OPTICAL EIGENMODES FOR ILLUMINATION & IMAGING

Sebastian Kosmeier

**A Thesis Submitted for the Degree of PhD
at the
University of St. Andrews**
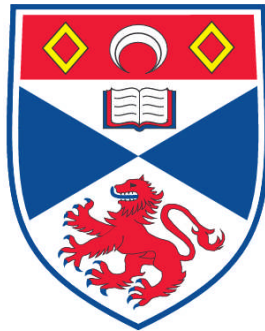
2012

**Full metadata for this item is available in
Research@StAndrews:FullText
at:
http://research-repository.st-andrews.ac.uk/**

**Please use this identifier to cite or link to this item:
http://hdl.handle.net/10023/3369**
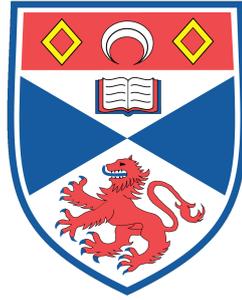
University
of
St Andrews

School of Physics & Astronomy

Optical Eigenmodes
for
Illumination & Imaging

Thesis submitted for the degree of

Doctor of Philosophy

Author: Sebastian Kosmeier

1st Supervisor: Prof Kishan Dholakia
2nd Supervisor: Dr Michael Mazilu

September 2012

Declaration

I, Sebastian Kosmeier, hereby certify that this thesis has been written by me, that it is the record of work carried out by me and that it has not been submitted in any previous application for a higher degree. This study was carried out at the University of St Andrews between 2009 and 2012.

Signature of Candidate: .... Date: ....

I hereby certify that the candidate has fulfilled the conditions of the Resolution and Regulations appropriate for the degree of Doctor of Philosophy at the University of St Andrews and that the candidate is qualified to submit this thesis in application for that degree.

Signature of Supervisor: .... Date: ....

In submitting this thesis to the University of St Andrews we understand that we are giving permission for it to be made available for use in accordance with the regulations of the University Library for the time being in force, subject to any copyright vested in the work not being affected thereby. We also understand that the title and abstract will be published, and that a copy of the work may be made and supplied to any bona fide library or research worker, that my thesis will be electronically accessible for personal or research use unless exempt by award of an embargo as requested below, and that the library has the right to migrate my thesis into new electronic forms as required to ensure continued access to the thesis. We have obtained any third-party copyright permissions that may be required in order to allow such access and migration, or have requested the appropriate embargo below. The following is an agreed request by candidate and supervisor regarding the electronic publication of this thesis: Access to Printed copy and electronic publication of thesis through the University of St Andrews.

Signature of Candidate: .... Signature of Supervisor: ....

Date: ....

Acknowledgement

First of all I want to thank Prof Kishan Dholakia for supervising this PhD and giving me the opportunity to work in his group. In times of discouragement, Kishan was a great motivator and ensured things will be alright. The same applies for Prof Thomas Krauss, whom I would like to thank as my mentor. In difficult times it was a great relief to know about and make use of the option of having an open conversation with him and getting honest feedback from him.

Then I would like to thank Drs Michael Mazilu, Jörg Baumgartl, Anna Chiara De Luca, Tom Vettenburg, and Andrea Di Falco for their support. Michael developed the theoretical framework of Optical Eigenmodes and especially helped me in theoretical questions, but also with practical issues. He let me take part in his deep physical understanding and did not get tired to explain the concept to me over and over again. Jörg helped me a lot in the lab, he taught me about light shaping, and there was no LabVIEW problem, that Jörg could not solve. Furthermore I want to thank him for being my guide at the beginning of my time in St Andrews. He made my life a lot easier by taking me to many social activities and introducing me to new people. Anna Chiara also taught me many things in the lab and I am especially grateful for benefitting from her strong expertise in Raman spectroscopy. She also never lost the patience to motivate me and always had time for a private talk. Tom I would like to thank for many inspiring discussions and as well as help in the lab. It is difficult to convince him of something and impossible to persuade him, but in exchange he also will not try to persuade you of something he is not sure about. His unbiased and open attitude make discussions with him challenging but at the same time very motivating and helpful. Furthermore my thanks go to Andrea for helpful discussions, but especially for fabricating countless nanostructures.

I also want to thank Martin Plöschner for valuable scientific discussions, but also for very good chats about cycling and other aspects of life. Moreover I have to thank Maria Leilani Torres for an introduction into cell culture (the corresponding experiments unfortunately did not make it into the thesis) and for being a very good friend. Caroline Thomson and Svetlana Zolotovskaya are acknowledged for setting up a new laser after failure of the old one. Further than that I also want to thank Svetlana for motivation during the final part of the PhD. I would also like to thank Rob Marchington, Tomáš Čižmár, Praveen Ashok, Bavishna Balagopal, and Mario Giardini for their support.

I am indepted to Kapil Debnath, not only for fabrication and taking SEM images, but especially for being one of the best flatmates and friends one can imagine. He had to listen to a lot of complaints, but hardly ever complained himself. I am also grateful to Raphal Adler for his friendship, good pub and gym

List of Publications

- M. Mazilu, J. Baumgartl, S. Kosmeier, K. Dholakia, *Optical Eigenmodes; exploiting the quadratic nature of the energy flux and of scattering interactions*, Optics Express **19**, 933-945 (2011)

- J. Baumgartl, S. Kosmeier, M. Mazilu, E.T.F. Rogers, N. I. Zheludev, K. Dholakia, *Far field subwavelength focusing using optical eigenmodes*, Applied Physics Letters **98**, 181109 (2011)

- A.C. De Luca, S. Kosmeier, K. Dholakia, M. Mazilu, *Optical eigenmode imaging*, Physical Review A **84**, 021803 (2011)

- S. Kosmeier, M. Mazilu, J. Baumgartl, K. Dholakia, *Enhanced two-point resolution using optical eigenmode optimized pupil functions*, Journal of Optics **13**, 105707 (2011)

- S. Kosmeier, M. Mazilu, A.C. De Luca, J. Baumgartl, K. Dholakia, *Optical eigenmodes for imaging applications*, Proceedings of SPIE **8274**, 82740I (2012)

Attended Conferences & Courses

- 3$^{\text{rd}}$ Summer School on Optoinformatics, Maynooth, Ireland (June 2010, Poster: *Optimization of amplitude and phase filters to locally beat the far field diffraction limit*)

- Nanoscope EPSRC Basic Technology Project Open Day, Southampton, England (March 2011, Talk: *Optimized pupil filters for confocal imaging*)

- SPIE Photonics West Conference, San Francisco, USA (January 2012, Talk: *Optical Eigenmodes for Imaging Applications*)

- IOP Nanolight Day, London, England (June 2012, Poster: *Enhanced two-point resolution using a spatial light modulator as complex pupil filter*)

- Summer School on Advanced Scientific Programming in Python, Kiel, Germany (September 2012)

- EOS Annual Meeting, Aberdeen, Scotland (September 2012, Talk: Coherent Control using Optical Eigenmodes)

Abstract

This thesis exploits so called "Optical Eigenmodes" (OEi) in the focal plane of an optical system. The concept of OEi is introduced and the OEi operator approach is outlined, for which quadratic measures of the light field are expressed as real eigenvalues of an Hermitian operator. As an example, the latter is employed to locally minimise the width of a focal spot. The limitations of implementing these spots with state of the art spatial beam shaping technique are explored and a selected spot with a by 40 % decreased core width is used to confocally scan an in focus pair of holes, delivering a two-point resolution enhanced by a factor of 1.3.

As a second application, OEi are utilised for fullfield imaging. Therefore they are projected onto an object and for each mode a complex coupling coefficient describing the light-sample interaction is determined. The superposition of the OEi weighted with these coefficients delivers an image of the object. Compared to a point-by-point scan of the sample with the same number of probes, i.e. scanning points, the OEi image features higher spatial resolution and localisation of object features, rendering OEi imaging a compressive imaging modality. With respect to a raster scan a compression by a factor four is achieved. Compared to ghost imaging as another fullfield imaging method, 2-3 orders of magnitude less probes are required to obtain similar images. The application of OEi for imaging in transmission as well as for fluorescence and (surface enhanced) Raman spectroscopy is demonstrated.

Finally, the applicability of the OEi concept for the coherent control of nanostructures is shown. For this, OEi are generated with respect to elements on a nanostructure, such as nanoantennas or nanopads. The OEi can be superimposed in order to generate an illumination of choice, for example to address one or multiple nanoelements with a defined intensity. It is shown that, compared to addressing such elements just with a focussed beam, the OEi concept reduces illumination crosstalk in addressing individual nanoelements by up to 70 %. Furthermore, a fullfield aberration correction is inherent to experimentally determined OEi, hence enabling addressing of nanoelements through turbid media.

An animal with an olfactory sense or with hearing, however well developed, could never have created science. A smell is either good or bad, and even hearing is never entirely neutral; music can convey emotions with an immediateness of which the sober visual arts are incapable. No wonder that the very word "objective" has been appropriated by optics.

Dennis Gabor,
about a remark of
Aldous Huxley

Contents

Chapter 1

Introduction

Oscillations refer to events that are repeating themselves and are inherent in almost all natural processes. Be it the recurring change between the seasons or between day and night, the periodic ebbing of the tide, or just waves on the ocean, moving water up and down over and over again. All these processes are oscillations. As already implied by the latter example, in a physical manner the periodicity of these events can be dealt with as *wave* behaviour. An illustrative example for wave motion, besides water waves, is the swinging of a pendulum. However, also less intuitive phenomena, like the movement of an electron in the Coulomb potential of a hydrogen nucleus or the nature of *light*, may be described as a wave.

Another well known instance of waves and oscillations is the field of acoustics. A string, which is under tension fixed between two points, will start to vibrate if it is excited, e.g. by moving it away from its equilibrium position and releasing it. This vibration is transfered to the surrounding air and detected as a sound, when striking our eardrum. Depending on the excitation, the string can either move in a "chaotic" manner or in a stable standing wave pattern. In the second case the string was hit at *resonance*. This means that the excitation was supporting a "natural" state of motion of the string. These forms of oscillation are called *eigenmodes*, *normal modes*, or simply *modes* of the string. They are characterised by their "natural" wavelength and frequency.

In general, every oscillating system has characteristic modes that describe states of oscillation and energy of the system. This can be an object of everyday life, such as a car body, whose dynamic properties are tweaked using modal analysis [1]. But also a rather big object like our earth has distinctive modes of core and mantle that can be excited by seismic activity, as happened by the Great Bolivia and Kuril Islands earthquakes in 1994 [2]. With respect to sound and vibration, modal analysis is for example used to determine and tailor the acoustical properties of a violin [3, 4]. Figure 1.1 shows so called "Chladni figures" of the top and bottom plate of a violin. They are generated by fixing the plates above a powerful speaker and exciting it with sound of different frequencies [5].
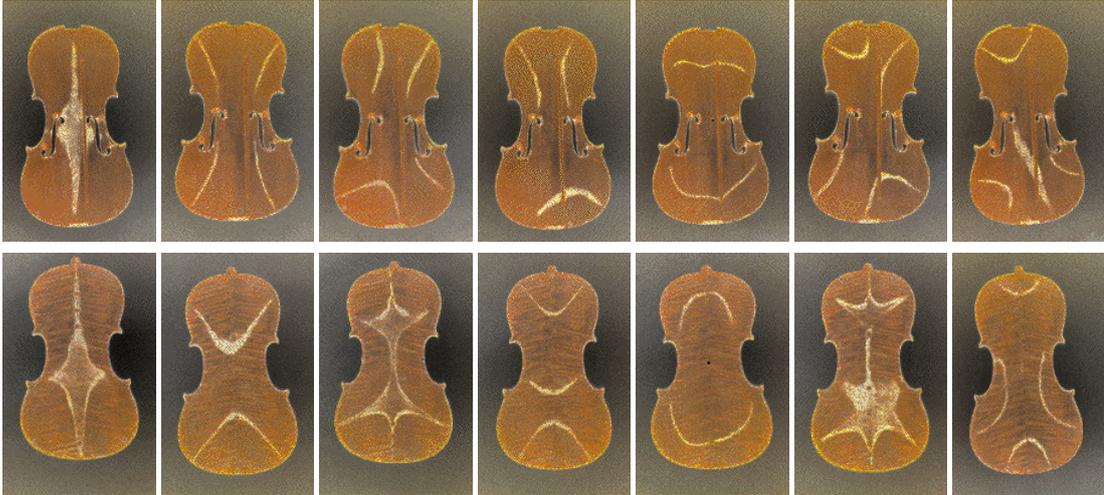
Figure 1.1: Chladni figures of the top and bottom plate of a violin, excited with frequencies between 91 Hz and 392 Hz (pictures with permission of Joe Wolfe from `http://www.phys.unsw.edu.au/jw/patterns1.html`, accessed 14th March 2012). For better visibility the colours of the pictures are inverted, such that the powder which accumulates in the nodal areas is white.

If the sound hits a resonant frequency of the plate, a powder put on top of the plate accumulates in the nodal areas of the excited mode. Tonal adjustment of the violin can then be done by changing the stiffness and mass distribution of the plate. Another example for the application of modal analysis is in characterising the dynamic properties of buildings [6]. Bridges are subject to vibrations, which may be vehicle induced [7], occur under passage of a train [8], or originate from natural phenomena such as wind [9] or earthquakes [10]. Furthermore, also the stability of tall as well as small houses is affected by seismic activated [11] and traffic-induced vibrations [12]. Here, modal analysis helps adjusting the construction, e.g. by damping, in order to minimise resonances with these factors and avoid incidences such as the collapse of the Tacoma Bridge in 1940 [13].

However, there is more in the concept of modes than "just" analysing resonances. An important property of modes is that their oscillations are orthogonal with respect to each other, each of the modes representing a degree of freedom of a linear system. Hence, every possible state of the system can be expanded into a linear superposition of modes. What makes this approach very powerful is that most states of the system can be well described using the system's most prominent modes. This *compressive* feature finds applications for speeding up detection and modeling processes. Face recognition for example is used in security systems and criminal identification. One approach for improving this procedure is to first determine a set of *eigenfaces*, which represent the most significant features from a sample of test faces [14, 15]. The eigenfaces can be thought of as "modes" of the

Figure 1.2: Intensity distribution of the first 20 Hermite-Gaussian modes in a laser cavity with rectangular symmetry calculated according to [22].

human face, which oscillate around the average face of the sample. A picture of a face which one wants to identify is then projected onto this subset of eigenfaces, delivering projection coefficients to approximate the given face. This enables comparison of the obtained coefficients with the sets of coefficients in the database to identify a face, which is much faster than comparing the face to every single face in the database picture by picture. A further application of modal analysis is in modelling the motion of objects. Therefore an object's motion is decomposed into deformation modes. Then the movement of the object is modelled as a linear superposition of only the principle modes, thus greatly reducing computational load [16]. This approach is used in engineering to model dynamic properties of objects such as airfoils [17]and in computer anmiations used for surgical training [18, 19]. Moreover modal analysis is employed to animate characters [20] and their clothes [21] in e.g. video games or animated movies.

In the field of optics and photonics the concept of modes is traditionally important for lasers and their cavities, respectively, as well as for waveguides such as optical fibers. Here one distinguishes between longitudinal modes, which correspond to the spectral content of the light, and transverse modes, that are characterised by their spatial intensity and phase distribution in a transverse cross section through the waveguide or cavity. As an example, Figure 1.2 depicts intensity profiles of the first 20 transverse modes in a laser cavity with rectangular symmetry. An analysis of these modes can be performed e.g. with complex optical filters [23–27] or by a numerical "fit" of a chosen basis set to a measured intensity pattern [28]. On the one hand this gives insight into effects like mode competition [29] and mode coupling or loss mechanisms. Furthermore it supplies
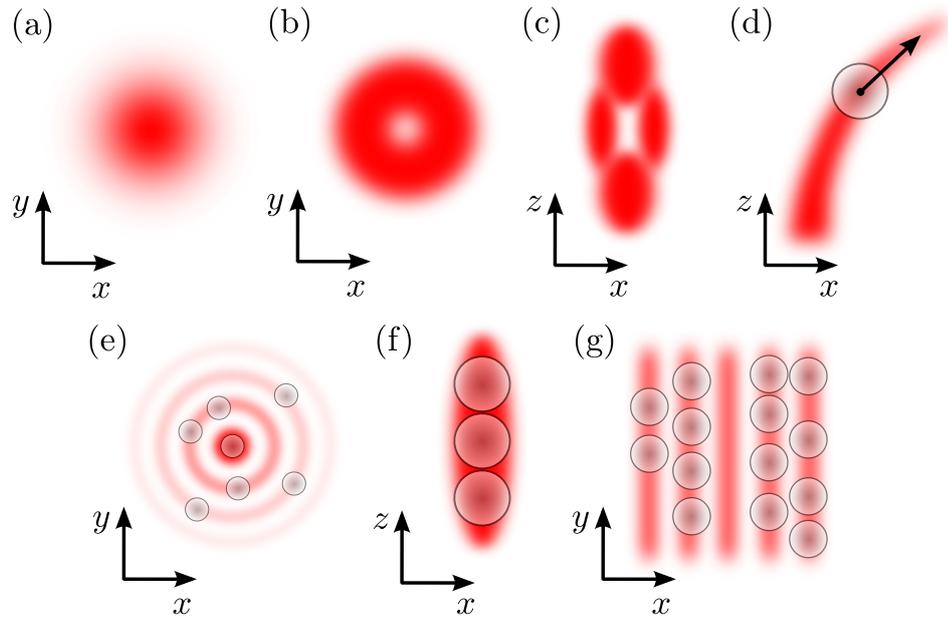
Figure 1.3: Schematics of some examples beams: (a) Gaussian beam, (b) Laguerre-Gaussian beam, (c) bottle beam, (d) Airy beam, (e) Bessel beam, (f) Axially elongated focus, (g) periodic interference pattern.

knowledge about the propagation properties, hence enabling prediction of the beam size and quality at certain distances from the fiber or laser output [30–32]. On the other hand the mode concept is useful to tailor the output of lasers and fibers. For example the bending loss of a large area multimode fiber, allowing higher power throughput then smaller area single mode fibers, can be tweaked in order to impair higher order modes [33–35]. This enables near single mode operation for high power applications. To increase the output power of lasers they can be forced into single higher order transverse mode operation e.g. by positioning phase optical elements inside the cavity [36]. The higher order mode exploits a bigger volume of the gain medium than the fundamental gaussian mode, hence delivering more output power, while still featuring stable operation and low divergence [37].

Recently, more and more photonic applications evolve that also use light fields deviating from the fundamental Gaussian beam profile, which is shown in Figure 1.3a. Applications include, but are not limited to, optical micromanipulation, imaging, and coherent control. The latter refers to the structured illumination of plasmonic nanostructures to selectively activate elements of that structure. This is useful for for sensing or micromanipulation as well. In the following some of these applications are explained in more detail.

With respect to imaging, modified focal fields or point spread functions (PSF) are mostly used to improve spatial and temporal resolution. Certain modifications

to the pupil of the illuminating or detecting objective of a scanning confocal microscope can improve axial [38] or lateral resolution [39]. In a widefield fluorescence microscope, enhanced axial localisation capabilities can for example be obtained by inducing a controlled two dimensional astigmatism on the detection side [40]. A very popular instance from imaging using for example a "doughnut" shaped light beam to obtain enhanced resolution is REversible Saturable/Switchable Optical Linear Fluorescence Transition (RESOLFT) microscopy. The concept of RESOLFT is to spatially restrict fluorescence by a bleaching spot with zero intensity in its center, thus delivering an effective PSF reduced in size. Implementations include STimulated Emission Depletion (STED) and Ground State Depletion (GSD) microscopy [41, 42]. In STED microscopy, fluorescence is excited by a normal Gaussian beam. Then a Laguarre-Gaussian (LG) beam, depicted in Figure 1.3b, depletes the fluorescence again, except for the small central dark region of the beam. This procedure limits the area from which fluorescence is emitted and detected, hence enabling imaging below the diffraction limit. The order of excitation and depletion is inverted in GSD, for which first the ground state of the fluorophor is depleted with the LG beam, such that the Gaussian beam only excites fluorescence in a small region. To improve also the axial resolution with the RESOLFT method, light patterns are used that feature a dark central core in three 3D [43], such as a so called "bottle beam", shown in Figure 1.3c. Another imaging example that uses spatially structured light fields is Structured Illumination Microscopy (SIM). In SIM a resolution gain is achieved by projecting a periodic fringe pattern onto the sample and numerically evaluating the moiré fringes resulting for different orientations and positions of the fringes [44]. Also using full field illumination of the sample opposed to scanning a focussed beam, the number of probes to obtain an image can be reduced for sparse samples by compressive imaging [45]. Here the sample is illuminated with various patterned light fields, and for each of the fields the total intensity resulting from the light-sample interaction is recorded. Furthermore, modifying the light incident on or collected from the sample, it is even possible to image through turbid media [46].

In the field of micromanipulation, microscopic objects can be trapped in high and low intensity areas of focussed beams [47, 48]. For example the optical force acting on a particle can be used to trap a particle in the center of a Gaussian beam. A simple translation of the beam in 3D evokes a translation of the particle. This method allows to manipulate one particle with one focus. Using more complex beams, micromanipulation can be performed with a higher throughput. Beams such as hollow core Laguerre Gaussian beams, Bessel beams, and Airy beams allow efficient transport of particles in two and three dimensions [49–51]. A so called "Airy beam" for example is generated by a cubic phase gradient in the pupil plane. Its beam path exhibits a curve, on which particles move along. This effect is visualised in Figure 1.3d and it can be used to move particles from one sample chamber to another [51]. In the "washboard" type potential of a Bessel beam,

particles first gradually move in lateral direction towards the center of the beam and finally in axial direction along the elongated focus [50]. Figure 1.3e shows a sketch of this process. Furthermore, elongated foci enable optical binding [52], alignment of elongated objects like for example glass rods and chromosomes [53], and stacking of particles [54, 55]. The latter situation is depicted in Figure 1.3f. To parallelise manipulation of matter, complex light shaping is used to generate periodic potentials for the light-matter interaction. For example microscopic particles can be periodically confined in arrays of traps [56] and close to surfaces in evanscent interference patterns [57, 58], as illustrated in Figure 1.3g. Further than just trapping and transporting them, particles can also be sorted in standing wave patterns or "optical lattices" [59, 60]. Moreover, complex fields enable not only the translation of particles, but also other movements such as rotation. For example small objects can be rotated in spiral interference patterns [61] and by light beams carrying orbital angular momentum [62–65], such as the LG beam in Figure 1.3b, which features a rotational phase gradient around its center.

A third utilisation of structured light fields is so called "coherent control" [66–69]. Here metallic nano structures such as nanopads [70] or antennas [71] are coherently illuminated in order to form "photonic landscapes" in their vicinity [71]. The intensity maxima and minima of these can for example be used for optical trapping [72–74] and sensing with fluorescence and SERS [75–77]. Furthermore, the local heat generation due to the field enhancement enables convections on the microscopic scale [78], which can again be utilised for trapping [79]. As the structures are fabricated by etching or ion beam milling in materials like gold or silver, they are static. But the light fields they form can still be modified to some extend by shaping the illumination [66, 67, 69], for example using higher order Hermite-Gaussian modes [68] as depicted in Figure 1.2. This promises the flexible use of static nanostructures for novel schemes in optical micromanipulation, sensing, and maybe also imaging.

In conclusion there are many applications for light fields, which are different from a conventional Gaussian beam. However, in most of the cases the light fields for each application are based on an intuitive choice. This means that either ideas for new applications evolve based on already known fields or for a new application idea a field with sufficient properties is selected from a repertoire of already known fields. For example the intuitive choice for spinning a particle would be a beam with some angular momentum or for optical guiding one would chose an elongated beam profile. But would it not be more efficient to freely tailor the field to fulfill specified properties depending on the application one has in mind? — Exploring that option is part of this work. The basic concept used here is to first decompose the optical field in the focal plane of an optical system into orthogonal modes, here called *Optical Eigenmodes* (OEi). Then the superposition of these modes is tailored to exhibit certain properties. One method is to construct, based on the OEi, operators, whose eigenvalues correspond to the magnitude of a quadratic

measure of the field, such as optical intensity or momentum. The corresponding eigenfunctions are the fields featuring that magnitude. This concept is related to quantum mechanics, where the observables of a system are eigenvalues and the states of the system are eigenfunctions of an operator [80]. Importantly, the field corresponding to the minimum eigenvalue minimises the chosen quadratic measure, while the field related to the maximum eigenvalue maximises it. Hence, based on the eigenvalue spectrum, one can select the optical field that extremises the chosen measure. In Chapter 3 this method is used to minimise the width of a focal spot.

Another important feature of the OEi is their orthogonality and the fact that, based on their eigenvalue spectrum, they can be ordered by their information content. Hence, they form the optimum base to express a quadratic measure, such as intensity. For an intensity image this means that they are the set of functions to express the information in that image with the minimum possible number of functions. In Chapter 4 this property is used for highly compressive imaging. Therefore the OEi are projected onto the object one wants to image and for each mode a complex coupling coefficient with respect to the sample is determined. The superposition of the modes with these coefficients then delivers an image of the object.

In a similar fashion, optical eigenmodes can be projected onto a target function, i.e. a light fields one wants to generate. The resulting superposition of the modes then delivers the desired field. This concept is employed in Chapter 5 to perform coherent control of gold nanostructures. Here the advantage of using OEi to approximate a target function opposed to for example a superposition of Gaussian beams is, that due to their orthogonality and phase information, the superposition of OEi can correctly deal with interference.

Additionally to the structure that has already been outlined by now, Chapter 6 summarises the content of this thesis and provides conclusions and an outlook onto future directions. The next Chapter 2 covers the theory of propagation and focussing of light and introduces the concept of optical eigenmodes.

Chapter 2

Optical Eigenmodes

This chapter deals with the decomposition of coherent light into Optical Eigenmodes (OEi). Section 2.1 gives a brief introduction into light as a wave. The outlined solutions of the wave equation are used in Section 2.2 for the numerical description of propagation and in particular of focussing of light. This is needed to simulate probe fields in the focal plane of an optical system, which are then used to calculate OEi. The diffraction limit is a fundamental restriction for many photonic applications. It prohibits perfect focussing of light and also plays a central role throughout this thesis, for example for the coherent control of metallic nanostructures, which is dealt with later on. Attention is paid to the diffraction limit in Section 2.3. In Section 2.4 optical degrees of freedom in a linear optical system are discussed and related to the OEi. Section 2.5 deals with the heart of this thesis: Optical Eigenmodes. It is described how the focal plane of a linear optical system is decomposed into its degrees of freedom, i.e. into optical eigenmodes. Furthermore, the concept of extremising quadratic measures of the light field using operators is outlined. Finally, examples for OEi in a square and a circular region are determined and illustrated. The content of this chapter is summarised in Section 2.6.

2.1 Light

According to the concept of wave-particle duality, light exhibits properties of both waves and particles [81]. Particle like behaviour can be observed during interaction with matter in terms of emission and absorption processes, such as the photo electrical effect [82]. For optical systems involving propagation through free space, lenses, and other optical elements, it is more convenient to describe light in a wavelike manner as an electromagnetic or wave field. In general light is a three dimensional vector field $\mathbf{U}(\mathbf{r}, t)$ depending on both the spatial coordinate $\mathbf{r}$ and the time t. However, methods presented in this work rely on experimental measurements of the field. With conventional interference techniques this

only delivers scalar amplitude and phase information. Thus the procedure is here simplified to the scalar field $U(\mathbf{r}, t)$ only. Monochromatic fields in a linear, homogeneous, and isotropic medium are solutions of the scalar wave equation [83]

$$\left\{\nabla^2 - \frac{1}{c^2}\frac{\partial^2}{\partial t^2}\right\} U(\mathbf{r}, t) = 0 \tag{2.1}$$

with c representing the phase velocity of light in a given medium. Substituting the separation of variables $U(\mathbf{r}, t) = E(\mathbf{r})\, V(t)$ into Equation 2.1 delivers two individual equations, one for the space dependent part $E(\mathbf{r})$ and one that governs the time dependence $V(t)$. In the following the latter is neglected, as this work deals with spatial light modes. The space dependent part of Equation 2.1 is known as the *Helmholtz Equation* [84]

$$\left\{\nabla^2 + k^2\right\} E(\mathbf{r}) = 0. \tag{2.2}$$

In Equation 2.2, $k = 2\pi\nu/c$ denotes the magnitude of the wave vector

$$\mathbf{k} = \begin{pmatrix} k_x \\ k_y \\ k_z \end{pmatrix} \tag{2.3}$$

and ν is the frequency of the light. Prominent solutions of Equation 2.2 are plane waves

$$E(\mathbf{r}) = E_0\, \mathrm{e}^{\mathrm{i}\mathbf{k}\mathbf{r}}, \tag{2.4}$$

propagating in the direction of $\mathbf{k}$, and spherical waves

$$E(r) = \frac{E_0}{r}\, \mathrm{e}^{\mathrm{i}kr} \tag{2.5}$$

with their source located at the coordinate origin and r being the magnitude of $\mathbf{r}$.

2.2 Propagation and focussing of light

The theory of light's propagation and focussing deals with the question of calculating the field in one plane of an optical system if it is known in another plane. The basis for scalar propagation theory is *Huygens' integral*, which is described in Section 2.2.1. The *Fresnel approximation* in Section 2.2.2 simplifies Huygens' integral in paraxial optical systems. Ray optics, depicted in Section 2.2.3, are a convenient tool for modeling the propagation through paraxial optical elements
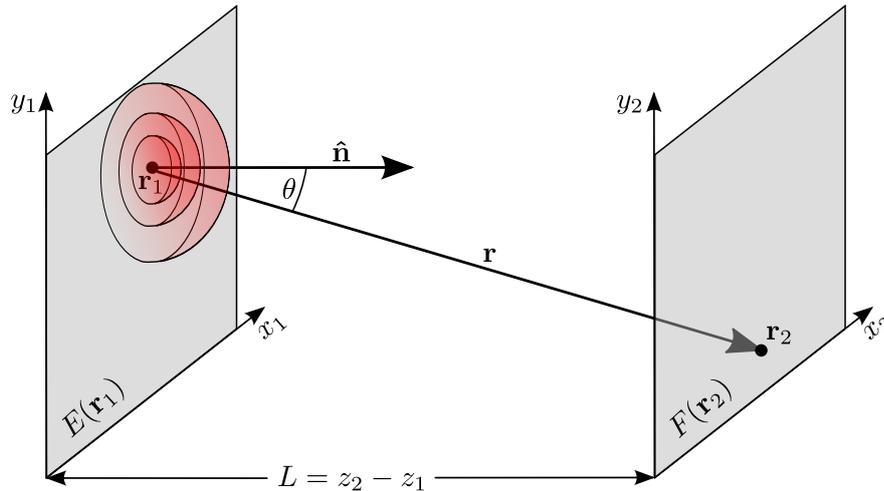
Figure 2.1: Propagation of light from one plane to a parallel plane according to Huygens' principle.

such as lenses. In Section 2.2.4 it is described, how ray optics and Huygens' integral are combined to simulate the focussing of light in radial symmetry. Modeling the focus of high numerical aperture (NA) optics requires vectorial propagation methods, of which one is specified in Section 2.2.5. However, the vectorial nature of light is in this case only used for the propagation itself, the calculation of OEi is then carried out with the scalar magnitude of the field.

2.2.1 Scalar theory of propagation: Huygens' integral

The underlying idea for the propagation theory of light is *Huygens' principle* [85]. Huygens suggested that each point of a *primary* wave front can be considered as the source of a *secondary* spherical wave. The primary wave at another point in space then results from the superposition of all the secondary waves at that point. In mathematical terms this can be expressed as Huygens' integral [22]:

$$F(\mathbf{r}_2) = \frac{\mathrm{i}}{\lambda} \iint\limits_{S} E(\mathbf{r}_1) \frac{1}{r} \, \mathrm{e}^{\mathrm{i}kr} \, \cos\theta \, d\sigma_1. \tag{2.6}$$

In Equation 2.6 the field E at the point $\mathbf{r}_1$ on the primary wave front is a source of a spherical wave $\exp(\mathrm{i}kr)/r$, which is weighted with the factor $\cos\theta$. The angle θ is the inclination between the vector $\mathbf{r}_2 - \mathbf{r}_1$ and the normal $\hat{\mathbf{n}}$ of the surface element $d\sigma_1$. Integration over the whole surface S delivers the field F at the point $\mathbf{r}_2$ on another primary wave front. The quotient i/λ in front of the integral is a normalisation factor. Figure 2.1 depicts the described situation for the simple case of a wave field propagating in z-direction from one plane to another parallel plane.

2.2.2 Fresnel approximation

In a paraxial situation, implying that the angle θ in Equation 2.6 is small, Huygens' integral can be simplified. This is useful to evaluate it via a Fast Fourier Transform (FFT) approach, hence enabling a rapid numerical implementation [86]. A further advantage, which will be used in this work, is that Huygens' integral can be written using ray matrices. These have the potential to model propagation through multicomponent paraxial optical systems in a convenient way.

For the *Fresnel* approximation it is, without loss of generality, assumed, that the major direction of propagation is along the z-axis. This corresponds to the situation depicted in Figure 2.1. Furthermore, the points $\mathbf{r}_1$ and $\mathbf{r}_2$ are located close to the z-axis, such that the angle θ is small. Then the factor $\cos\theta$ in Equation 2.6 can be approximated as unity. Moreover, the distance r between $\mathbf{r}_1$ and $\mathbf{r}_2$, which in cartesian coordinates is

$$r = \sqrt{(x_2 - x_1)^2 + (y_2 - y_1)^2 + (z_2 - z_1)^2}, \qquad (2.7)$$

can be approximated by the first terms of the power series

$$r = z_2 - z_1 + \frac{(x_2 - x_1)^2 + (y_2 - y_1)^2}{2(z_2 - z_1)} + \cdots . \qquad (2.8)$$

The distance r in the exponent of Equation 2.6 is approximated by the first two terms of Equation 2.8 and for r in the denominator all but the first term are dropped. If now, as in Figure 2.1, one is only interested in the propagation in z-direction between two parallel planes, then $z_2 - z_1$ equals the distance L between these planes and Equation 2.6 finally becomes

$$F(\mathbf{r}_2) \approx \frac{\mathrm{i}}{\lambda L} \, \mathrm{e}^{\mathrm{i}kL} \iint\limits_S E(\mathbf{r}_1) \, \exp\left[\mathrm{i}k\frac{(x_2 - x_1)^2 + (y_2 - y_1)^2}{2L}\right] \, dx_1 dy_1. \qquad (2.9)$$

Equation 2.9 is the Fresnel approximation of Huygens' integral, valid in paraxial optical systems.

2.2.3 Ray optics & ray matrices

A very convenient way to deal with the propagation of light through paraxial optical systems is by means of ray optics using ray matrices. In a system that is radial symmetric around the z-axis, each point of a ray can be described by its distance ρ to the z-axis and the slope $\rho' = d\rho/dz$ of the ray in that point as illustrated in Figure 2.2a. These two properties are bundled in a ray vector

$$\mathbf{r}^{\mathrm{ray}} = \begin{pmatrix} \rho \\ \rho' \end{pmatrix}. \qquad (2.10)$$
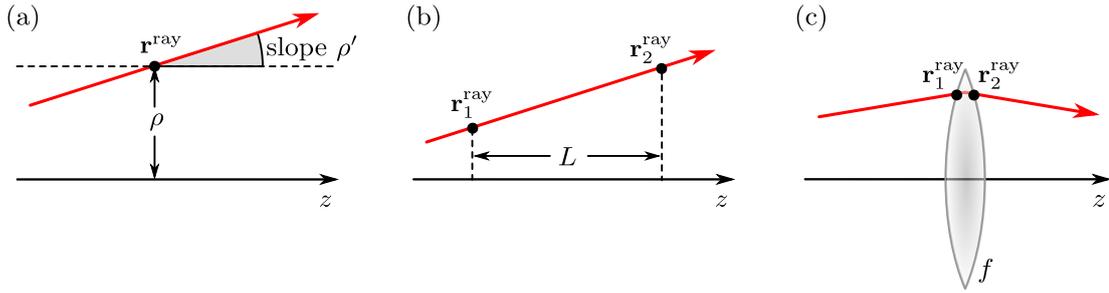
Figure 2.2: According ray optics: (a) Distance ρ to the z-axis and slope ρ' at a point $\mathbf{r}^{\text{ray}}$ of a ray. (b) Propagation of a ray in free space. (c) A ray transmitted through a thin lens of focal length f.

The effect of a paraxial optical element on a ray can then be represented by a ray or $ABCD$ matrix acting on the ray vector. If the ray before the optical element was described by $\mathbf{r}_1^{\text{ray}}$, the ray vector $\mathbf{r}_2^{\text{ray}}$ after passing the optics is the transformation of $\mathbf{r}_1^{\text{ray}}$ by a ray matrix:

$$\mathbf{r}_2^{\text{ray}} \equiv \begin{pmatrix} \rho_2 \\ \rho_2' \end{pmatrix} = \begin{pmatrix} A & B \\ C & D \end{pmatrix} \begin{pmatrix} \rho_1 \\ \rho_1' \end{pmatrix} \equiv \mathbf{M}^{\text{ray}} \, \mathbf{r}_1^{\text{ray}}. \tag{2.11}$$

The elements A, B, C, and D of the ray matrix specify the interaction of the ray with the optical element. Figures 2.2b and 2.2c depict free space propagation over a distance L and passage through a thin lens of focal length f. The corresponding $ABCD$ matrices are

$$\mathbf{M}_{\text{free}}^{\text{ray}} = \begin{pmatrix} 1 & L \\ 0 & 1 \end{pmatrix} \qquad \text{and} \qquad \mathbf{M}_{\text{lens}}^{\text{ray}} = \begin{pmatrix} 1 & 0 \\ -1/f & 1 \end{pmatrix}. \tag{2.12}$$

For an optical system consisting of a concatenation of elements, the propagation through the whole system can be expressed as the multiplication of the incident ray vector with the matrix, which results from a concatenation of the single element matrices. In this work the considered situation for focussing is: Light propagating from the backfocal plane of a lens through the lens and to the focal plane. The matrix describing the total propagation is the concatenation of three matrices, first free space propagation over distance f to the lens, then passage of the lens, and finally again free space propagation over distance f to the focal plane:

$$\mathbf{M}_{\text{focus}}^{\text{ray}} = \mathbf{M}_{\text{free}}^{\text{ray}} \, \mathbf{M}_{\text{lens}}^{\text{ray}} \, \mathbf{M}_{\text{free}}^{\text{ray}}. \tag{2.13}$$

With the matrices given in Equation 2.12, this focussing matrix can be calculated to be

$$\mathbf{M}_{\text{focus}}^{\text{ray}} = \begin{pmatrix} 0 & f \\ -1/f & 0 \end{pmatrix}. \tag{2.14}$$

2.2.4 Huygens' integral with ray matrices

Huygens' integral in Equation 2.9 describes the propagation of light through free space between two parallel planes. However, focussing light requires to include a lens into the optical path. The transformation introduced by the lens can, for one ray of light, be dealt with using matrix optics as shown in Section 2.2.3. In order to model the propagation from one plane to a parallel plane with a lens in between both planes, it is useful to combine Huygens' integral with ray matrices. In one transverse dimension, the Fresnel approximation of Huygens' integral with the elements of an $ABCD$ matrix can be written as [22]

$$
F(x_2, z_2) = \sqrt{\frac{\mathrm{i}}{B\lambda}}\, \mathrm{e}^{-\mathrm{i}kL} \cdot
$$
$$
\cdot \int_{-\infty}^{\infty} E(x_1, z_1) \exp\left[-\mathrm{i}\frac{k}{2B}\left(Ax_1^2 - 2x_1 x_2 + Dx_2^2\right)\right] dx_1. \qquad (2.15)
$$

Extending Equation 2.15 into two transverse dimensions is straightforward and shown in Appendix A.

In this work the paraxial case is only used for foci that are radial symmetric around the z-axis. Hence computational load can be reduced by using not two transverse dimensions but only the radial coordinate ρ in the x, y-plane. In Appendix A it is shown how Huygens' integral with $ABCD$ matrix elements can be derived in radial symmetry. Here only the final result

$$
F(\rho_2, z_2) = \mathrm{i}\frac{k}{B}\, \mathrm{e}^{-\mathrm{i}kL} \cdot
$$
$$
\cdot \int_{0}^{\infty} E(\rho_1, z_1) \exp\left[-\mathrm{i}\frac{k}{2B}\left(A\rho_1^2 + D\rho_2^2\right)\right] J_0\left(\frac{k}{B}\rho_1\rho_2\right)\rho_1\, d\rho_1 \qquad (2.16)
$$

shall be given with J_0 denoting the Bessel function of first kind and zero order. With the elements of the ray matrix in Equation 2.14 for focussing and the length of total propagation $L = 2f$, Equation 2.16 takes the simple form

$$
F(\rho_2, z_2) = \mathrm{i}\frac{k}{f}\, \mathrm{e}^{-2\mathrm{i}kf} \int_{0}^{\infty} E(\rho_1, z_1)\, J_0\left(\frac{k}{f}\rho_1\rho_2\right)\rho_1\, d\rho_1. \qquad (2.17)
$$

Equation 2.17 finally describes the paraxial propagation of a radial symmetric field from the backfocal plane of a lens with focal length f to the focal plane.

2.2.5 Debye approximation for non paraxial systems

The focussing of light described in Section 2.2.4 can be applied for paraxial optical systems. However, this work also deals with non-paraxial systems, such as high
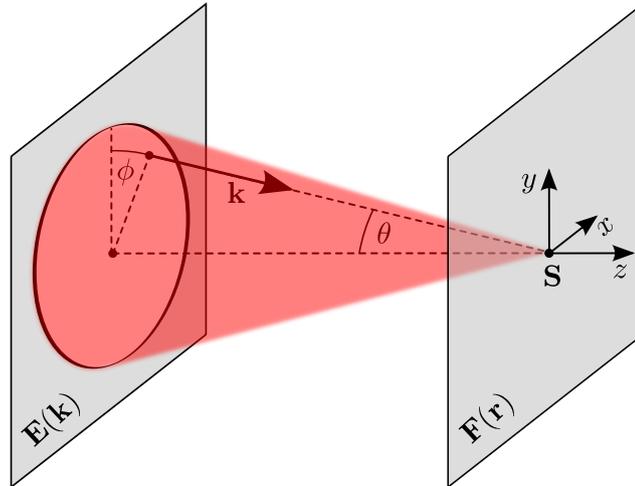
Figure 2.3: Focussing of light in Debye approximation. The cone from the focal point **S** to the edge of the aperture is indicated in red.

NA microscope objectives. In that case the Fresnel approximation is not valid any more. A common way to deal with the focussing of high NA optics is in the framework of the *Debye approximation*. According to that, the field in the focal region can be calculated as a superposition of the plane waves, whose wave vectors **k** fall inside the cone defined by the focal point and the aperture of the lens or objective [83]. This situation is illustrated in Figure 2.3. In mathematical terms the superposition is expressed as an integral over all the plane waves [87]:

$$\mathbf{F}(\mathbf{r}) = -\frac{\mathrm{i}k}{2\pi} \iint_{\Omega} \mathbf{E}(\mathbf{k}) \, \mathrm{e}^{\mathbf{i}\mathbf{k}\mathbf{r}} \, d\Omega \qquad (2.18)$$

with Ω denoting the solid angle defined by the cone from the focal point to the aperture edge. For a fast numerical implementation, the integral in Equation 2.18 can be evaluated using a Fast Fourier Transform (FFT) [88]:

$$\mathbf{F}(\mathbf{r}) \propto -\frac{\mathrm{i}k}{2\pi} \, \mathrm{FFT} \left(\mathrm{e}^{\mathrm{i}kz} \, \mathbf{E}_t(\theta, \phi) \, \frac{1}{\cos\theta} \right), \qquad (2.19)$$

where the coordinate transformed field $\mathbf{E}_t(\theta, \phi)$ has to be calculated from $\mathbf{E}(\mathbf{k})$. This and further details regarding the method can be found in Reference 88.

2.3 The diffraction limit

The "diffraction limit" imposes a lower limit for the minimum size to which light can be focussed and for the maximum resolution that can be obtained in bright-field light microscopy. A rule of thumb for the diffraction limit is $\lambda/2$, half the
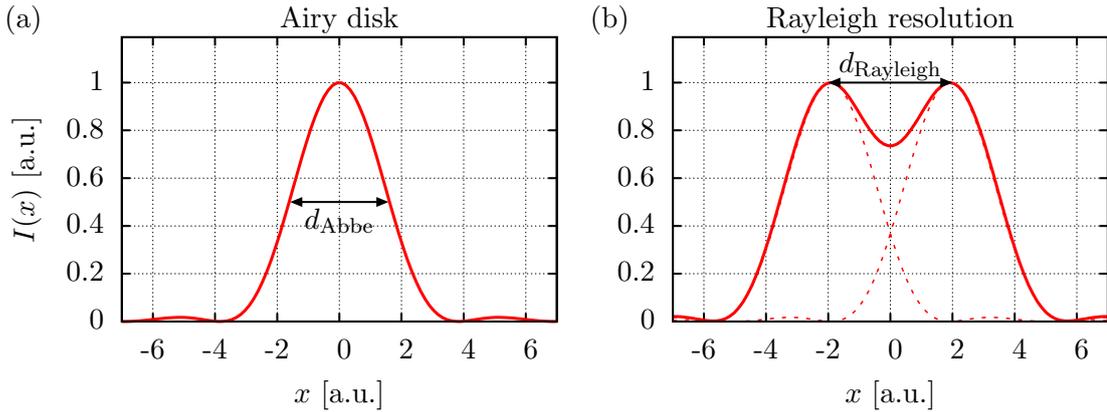
Figure 2.4: (a) FWHM of the Airy disk corresponding to Equation 2.20 with $I_{\max} = 1$. (b) Sum of the PSFs of two points, that are just resolved by the Rayleigh criterion.

wavelength λ of the light [89–91]. Two more precise definitions that are often used are the *Abbe* and the *Rayleigh* resolution limit.

The Abbe limit defines the minimum possible width of the Airy disk, which results from (i) focussing a plane wave or (ii) imaging a point with a conventional lens/microscope objective. Figure 2.4a shows a plot of the Airy disk's intensity I, which is calculated by [84]

$$I(\rho_{xy}) = I_{\max} \left(\frac{2 J_1(\rho_{xy})}{\rho_{xy}} \right)^2, \tag{2.20}$$

where $J_1(\rho_{xy})$ denotes the Bessel function of the first kind of order one, and ρ_{xy} is the radial coordinate in the x, y-plane. For a lens with numerical aperture NA, the minimum possible Full Width Half-Maximum[1] (FWHM) d_{Abbe} of the Airy disk according to Abbe is

$$d_{\mathrm{Abbe}} = 0.5 \, \frac{\lambda}{\mathrm{NA}}. \tag{2.21}$$

In Equation 2.21, λ denotes the wavelength of the light and the numerical aperture NA is the product of the refractive index n and the sine of half the opening angle α of the lens:

$$\mathrm{NA} = n \sin \alpha. \tag{2.22}$$

However, the Abbe limit just takes into account the image of one point.

The Rayleigh criterion considers the image of two point objects. It states that for incoherent illumination two points in the sample can be resolved, when the

---

[1]Further measures for the beam width will be discussed in Section 3.2.1

maximum of the first point's PSF coincides with the first minimum of the second point's PSF. This situation is depicted in Figure 2.4b. The distance d_{Rayleigh} of the two points in the sample is then [91, 92]:

$$d_{\text{Rayleigh}} = 0.61 \, \frac{\lambda}{\text{NA}}. \tag{2.23}$$

In that case the contrast C between a maximum and the central minimum in the diffraction of both points equals $26.5\,\%$.

Based on the $26.5\,\%$ contrast rule, the lateral two point resolution can be generalised for imaging modes other than incoherent widefield imaging as

$$d_{\text{points}} = K \, \frac{\lambda}{\text{NA}}. \tag{2.24}$$

The constant K for common imaging modes is [93, 94]:

$$
\begin{aligned}
K &= 0.61 && \text{for widefield incoherent,} \\
K &= 0.82 && \text{for widefield coherent,} \\
K &= 0.46 && \text{for confocal incoherent,} \\
K &= 0.56 && \text{for confocal coherent.}
\end{aligned}
\tag{2.25}
$$

The confocal resolutions in Equation 2.25 are better than the widefield ones, as the confocal pinhole reduces out-of-focus contributions. And the incoherent resolutions are better compared to the coherent ones, as the intensity PSF is narrower than the amplitude PSF.

2.4 Optical degrees of freedom

The amount of information that can be transmitted through an optical system is an important question for both imaging and light shaping. An object imaged by for example a microscope has an infinite number of degrees of freedom (DOF), while the number of DOF that is present in the image of the object is finite [95]. The question is [96]: How many independent variables are required to express the information about the object that is contained in its image? With respect to beam shaping one can consider an optical system with an input and an output plane as illustrated in Figure 2.5. In this context a relevant question is how many input functions $E(\mathbf{r_1})$ in the input plane one needs to generate a desired light field $F(\mathbf{r_2})$ in a region of interest (ROI) in the system's output plane. In both cases this number of DOF depends on the diffraction limit arising from the finite NA of the optical system.
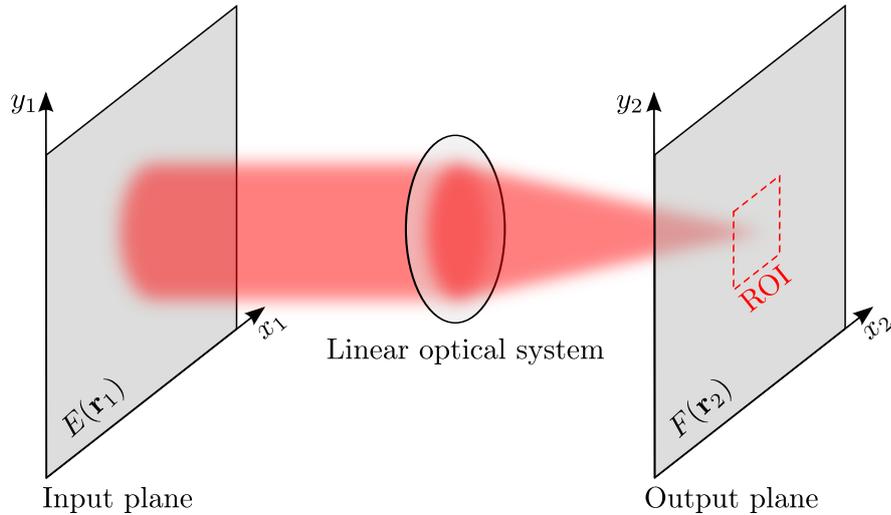
Figure 2.5: Propagation of the input field $E(\mathbf{r}_1)$ through a linear optical system forming the output field $F(\mathbf{r}_2)$.

Hence, in early work the number of independent optical variables was estimated based on the sampling theorem and related to the quotient of the object area and the area of a diffraction limited beam [95, 97]. This diffraction limited beam area can for a circular pupil be estimated by a Gaussian spot [96]. However, two Gaussian beams always overlap regardless of their seperation, hence they do not represent independent variables [98]. In a mathematically more rigorous approach the spatially finite input and output planes of an optical system are decomposed into spherical waves [98–100]. These are used to generate a Hermitian operator, whose eigenvectors are orthogonal and whose eigenvalues are real and hence can be ordered by magnitude. The superposition of the spherical waves with the elements of the eigenvectors results in orthogonal eigenfunctions. The magnitude of the associated eigenvalues is a measure for the coupling efficiency between the functions in the input and output plane. A large eigenvalue indicates a high intensity of the corresponding output eigenfunction and vice versa. The number of eigenvalues that is above the noise level of the optical system is equivalent to the number of usable DOF [100].

In Reference 101 the above concept is generalised to generate orthogonal eigenfunctions not only from spherical waves, but from *any* decomposition of the input and output plane. This has great advantage for experimental applications, as will be shown in the course of this work. These eigenfunctions are termed "Optical Eigenmodes" and it is demonstrated in Reference 101, how their superposition can be tailored to extremise certain measures of the electromagnetic field such as energy, intensity, spot size, or momentum. The fact that, according to their eigenvalues, these modes can be ordered by their relevance enables to only take into account the most important ones, which greatly simplifies optimisation tasks and

delivers the most efficient solution. Furthermore, with respect to imaging, the OEi can be projected onto an object in order to get an image with the maximum possible information content using the minimum necessary number of probes. In the next Section 2.5.1 it is outlined how the fields in an optical system can be decomposed into these OEi.

2.5 Optical Eigenmodes

In the next Section 2.5.1 it is described how the field in an optical system can be decomposed into optical eigenmodes. Furthermore it is outlined, how operators can be defined to extremise quadratic measures of the light field. Some examples for optical eigenmodes are then shown in Section 2.5.2.

2.5.1 Decomposition into Optical Eigenmodes

Here the decomposition of the light field in an optical system into optical eigenmodes is outlined. The full vectorial treatment for the electromagnetic field can be found in Reference 101. However, as mentioned in Section 2.1, in this work the procedure is simplified to the scalar electric field only. A sketch of the considered situation is depicted in Figure 2.5. The field $E(\mathbf{r}_1)$ in an input plane propagates through a linear optical system, forming the field $F(\mathbf{r}_2)$ in an output plane. In an experimental realisation the input plane would feature a device for complex light shaping, such as a spatial light modulator, and the linear optical system could e.g. be a lens or a microscope objective. Now the question is in which way the input field has to be modulated in order to generate orthogonal modes in the output plane. In a first step, the problem is restricted by defining a region of interest (ROI) in the output plane, indicated by the red dashed box in Figure 2.5. The next step is to probe the system to determine which modes are supported within this ROI. Therefore the input field E is decomposed into a set of "test" fields E_i,

$$E = \sum_{i=1}^{N} a_i \, E_i, \tag{2.26}$$

resulting in a set of fields F_i in the output plane,

$$F = \sum_{i=1}^{N} a_i \, F_i, \tag{2.27}$$

with complex coefficients a_i. It should be emphasized that the resulting modes not only depend on the symmetry of the ROI, but also critically on the choice

of test fields. For optimum results the probing should cover the largest possible amount of the system's degrees of freedom with respect to the ROI.

Similar to the calculation of the prolate spheroidal wave functions [102], the modes in the ROI are determined as solutions of an intensity maximization problem [103].[2] With an operator $\mathbf{M}^{(0)}$ whose elements $m_{ij}^{(0)}$ are the cross interferences of the test fields F_i in the ROI,

$$\mathbf{M}^{(0)} = \begin{pmatrix} M_{11}^{(0)} & \cdots & M_{1N}^{(0)} \\ \vdots & \ddots & \vdots \\ M_{N1}^{(0)} & \cdots & M_{NN}^{(0)} \end{pmatrix} \quad \text{with} \quad M_{ij}^{(0)} = \int\limits_{\text{ROI}} F_i \, F_j^* \, d\sigma_2, \qquad (2.28)$$

the total intensity I in the ROI can be written as

$$I = \mathbf{a}^\dagger \mathbf{M}^{(0)} \mathbf{a}. \qquad (2.29)$$

In Equation 2.28 the * indicates the complex conjugate, $d\sigma \equiv dx_2 dy_2$ represents the integration over the area of the ROI, and the † in Equation 2.29 denotes the conjugate transpose of the column vector $\mathbf{a}$, which contains the complex coefficients a_i:

$$\mathbf{a} = \begin{pmatrix} a_1 \\ \vdots \\ a_N \end{pmatrix} \quad \text{and} \quad \mathbf{a}^\dagger = \begin{pmatrix} a_1 \cdots a_N \end{pmatrix}. \qquad (2.30)$$

The operator $\mathbf{M}^{(0)}$ is Hermitian, thus featuring two important properties. Firstly, its eigenvectors $\mathbf{v}_k^{(0)}$ are orthogonal. This means that fields composed according to Equation 2.27 from the output fields F_i using the elements $v_{ki}^{(0)}$ of the eigenvectors as coefficients are orthogonal within the ROI. Due to the linearity of the optical system, the coefficients for the input fields E_i to generate orthogonal output fields are the same. Secondly, the eigenvalues $\lambda_k^{(0)}$ of $\mathbf{M}^{(0)}$ are real, hence sortable by magnitude. In fact the magnitude of $\lambda_k^{(0)}$ corresponds to the intensity in the ROI of the field F composed from the elements of $\mathbf{v}_k^{(0)}$. Hence, $\mathbf{M}^{(0)}$ is termed *Intensity Operator*. With respect to the ROI orthonormal fields $\mathbb{F}_k$ can be obtained by input fields $\mathbb{E}_k$ normalized with the square root of the eigenvalue $\lambda_k^{(0)}$:

$$\mathbb{E}_k = \frac{1}{\sqrt{\lambda_k^{(0)}}} \sum_{i=1}^{N} v_{ki}^{(0)} \, E_i, \qquad (2.31)$$

$$\mathbb{F}_k = \frac{1}{\sqrt{\lambda_k^{(0)}}} \sum_{i=1}^{N} v_{ki}^{(0)} \, F_i. \qquad (2.32)$$

---

[2]Actually it is shown in Reference 98 that for a rectangular system geometry and a decomposition of input and output plane into spherical waves, the orthogonal eigenfunctions correspond to the prolate spheroidal wave functions.

These fields $\mathbb{F}_k$ are called the *Optical Eigenmodes* of the system in the chosen ROI.

As mentioned in Section 2.4, the most efficient OEi feature the largest eigenvalues such that the OEi can be ordered according to their relevance. In some sense this renders the OEi method similar to a principle component analysis (PCA) [104] on the initial fields F_i: The initial fields F_i are reexpressed in a new basis set, the OEi $\mathbb{F}_k$, which is orthogonal and in which the dimensions are sorted by their information content about the system in the ROI. Prior to their usage for focal field optimisation or imaging, it makes sense to select the most important OEi. This can be done by setting a relative threshold $T \in [0,1]$ to select the M OEi whose eigenvalues $\lambda_k^{(0)}$ are larger then $T \lambda_1^{(0)}$. The correct choice of the value for T depends on the noise level of the optical system. If T is to small, the intensity of some OEi will be below the noise level. The number of OEi, whose eigenvalues are above the noise level, can be associated with the number of degrees of freedom of the system, given that they were covered by the initial choice of test fields F_i.

After selection of the appropriate modes, their superposition can be tailored to extremise quadratic measures of the field. Therefore other operators corresponding to quadratic measures of the light field can be constructed in a way similar to Equation 2.28, using the eigenmodes $\mathbb{F}_k$ instead of the fields F_i. As one example, a *Spot Size Operator* is defined in Chapter 3 to locally minimise the width of a focal spot. Further options include for example an *Energy Operator* or a *Momentum Operator*, as outlined in Reference 101. A form of the latter operator has been applied in Reference 105 to simulate the field that acts with the maximum force on a plasmonic particle. This operator concept is general for all quadratic measures in linear optical systems. Before applying it in Chapter 3, some examples of optical eigenmodes are shown in the next Section 2.5.2.

2.5.2 Examples of Optical Eigenmodes

This section shows some examples for optical eigenmodes in the focal plane of optical systems for two different system geometries. As a first example, OEi are simulated in the focal plane of a lens with 1 m focal length. This corresponds to the setup used in the next Chapter 3 with the input plane being the backfocal plane of the lens and the output plane being the focal plane. More quantitative detail on the exact arrangement can be found in Chapter 3, in the following the description is limited to the information necessary for this example. The laser beam is simulated with a wavelength of 633 nm and a uniform intensity distribution over its cross section. Furthermore, in both the backfocal and the focal plane circular masks of 8.64 mm and 360 μm diameter respectively are applied. Hence

$\lambda_1^{(0)} = 1$ $\quad$ $\lambda_2^{(0)} = 0.48$ $\quad$ $\lambda_3^{(0)} = 0.25$ $\quad$ $\lambda_4^{(0)} = 4.8 \cdot 10^{-3}$ $\quad$ $\lambda_5^{(0)} = 1.5 \cdot 10^{-5}$

0 — Intensity [a.u.] — 1 $\qquad$ 0 — Phase [rad] — 2π
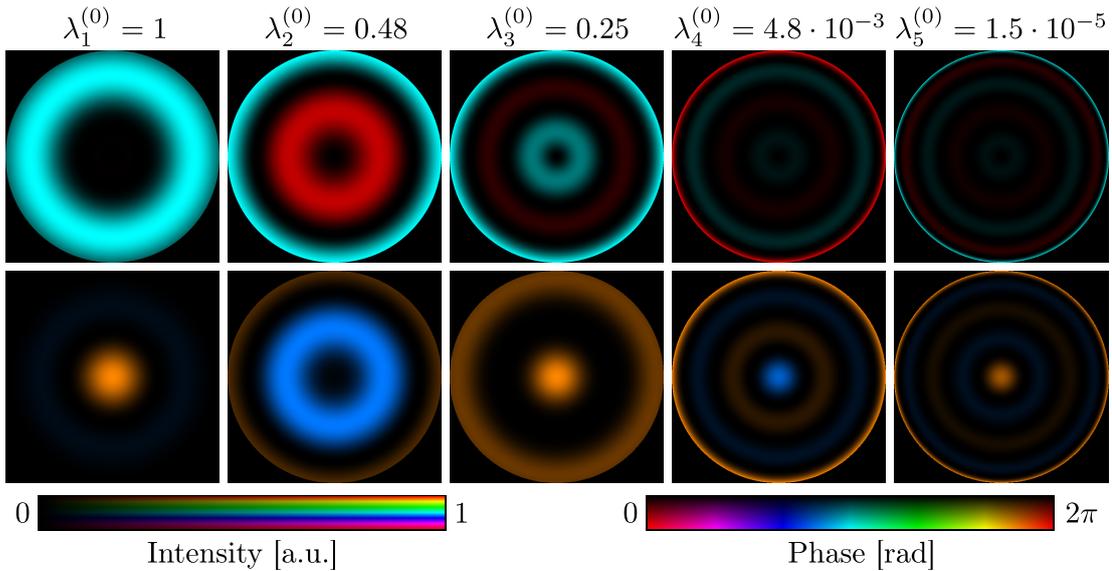
Figure 2.6: First 5 optical eigenmodes in a circular region of interest. Their efficiency is denoted by the associated eigenvalues $\lambda_k^{(0)}$. Top row: Fields $\mathbb{E}_k$ in the reciprocal, i.e. the SLM plane. Bottom row: Focal fields $\mathbb{F}_k$ resulting from the reciprocal fields in the top row. The coordinate origin is located at the center of each picture.

both input and output plane feature radial symmetry. The input plane is then decomposed into nonoverlapping annular rings of different diameter. These represent the input fields E_i. The resulting focal fields F_i, in this case Bessel beams, are calculated using the radial symmetric representation of Huygens' integral in Equation 2.17. These are then used to determine optical eigenmodes as outlined in Section 2.5.1. The first five OEi are depicted in Figure 2.6 with the backfocal fields $\mathbb{E}_k$ in the top row and the focal fields $\mathbb{F}_k$ in the bottom row. With increasing mode number k higher spatial frequencies are more pronounced in the fields $\mathbb{E}_k$. This results in a smaller central spot for higher order modes $\mathbb{F}_k$ for the price of reduced efficiency. The intensity in each picture is actually normalised, but the eigenvalues $\lambda_k^{(0)}$ indicate the rapid decay in efficiency with increasing k.

As a second example OEi are simulated again for circular system symmetry of the input plane, but this time in a square ROI in the output plane. More precisely, the 3.5 mm diameter backfocal plane of a 1.3 NA oil emersion objective is decomposed into fields E_i with different spatial phase gradients $\phi = k_x x_1 + k_y y_1$ and unity intensity over the pupil. The values for k_x and k_y are chosen such that the foci F_i, calculated according to Equation 2.19, are deflected within a square ROI of 10 µm × 10 µm size. The step width in the focal plane between two deflections was chosen to be 100 nm, corresponding to a slight oversampling compared to the diffraction limited FWHM of about 300 nm at the simulated 785 nm wavelength. This choice of parameters results in 10201 test fields F_i,

Eigenvalue spectrum of OEi in square ROI
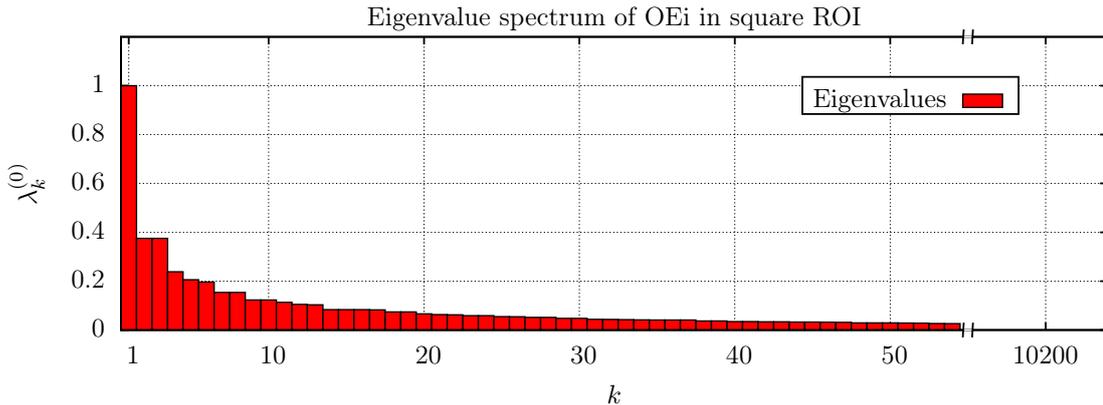
Figure 2.7: Eigenvalues $\lambda_k^{(0)}$ of the intensity operator $\mathbf{M}^{(0)}$ according to Equation 2.28 when probing a square with 10201 foci F_i.

which are used to generate the intensity operator $\mathbf{M}^{(0)}$, from which OEi are then determined according to Section 2.5.1. The resulting eigenvalues $\lambda_k^{(0)}$ are plotted in Figure 2.7, showing their rapid decay with increasing k. The input fields $\mathbb{E}_k$ and the resulting output fields $\mathbb{F}_k$ are depicted in Figures 2.8 and 2.9 respectively. Also here it can be observed that with increasing mode number k, i.e. decreasing eigenvalue $\lambda_k^{(0)}$, the input OEi feature higher spatial frequencies so that the output OEi consequently exhibit finer spatial details. A further aspect worth noticing is that due to the square symmetry degenerate modes exist. This means that two different modes have the same eigenvalue, as it is the case e.g. for $k = 2$ and $k = 3$. The spatial field distribution of both modes is the same except for a rotation by 90° with respect to the coordinate origin. In Chapter 4 these OEi in a square ROI are utilised to perform imaging. Furthermore, in the context of coherent control presented in Chapter 5, they provide the set of test fields to guarantee an efficient probing for the experimental determination of OEi on metallic nanostructures.

2.6 Summary

This chapter introduced the concept of Optical Eigenmodes. After a brief introduction to the wave nature of light, the numerical description of its propagation and focussing was outlined. Then the diffraction limit and its effect for focussing and different imaging modalities was described. The question for the degrees of freedom in an optical system, related to the diffraction limit, was discussed. After that, the optical eigenmode concept was outlined. With respect to that the following aspects have been addressed and pointed out:
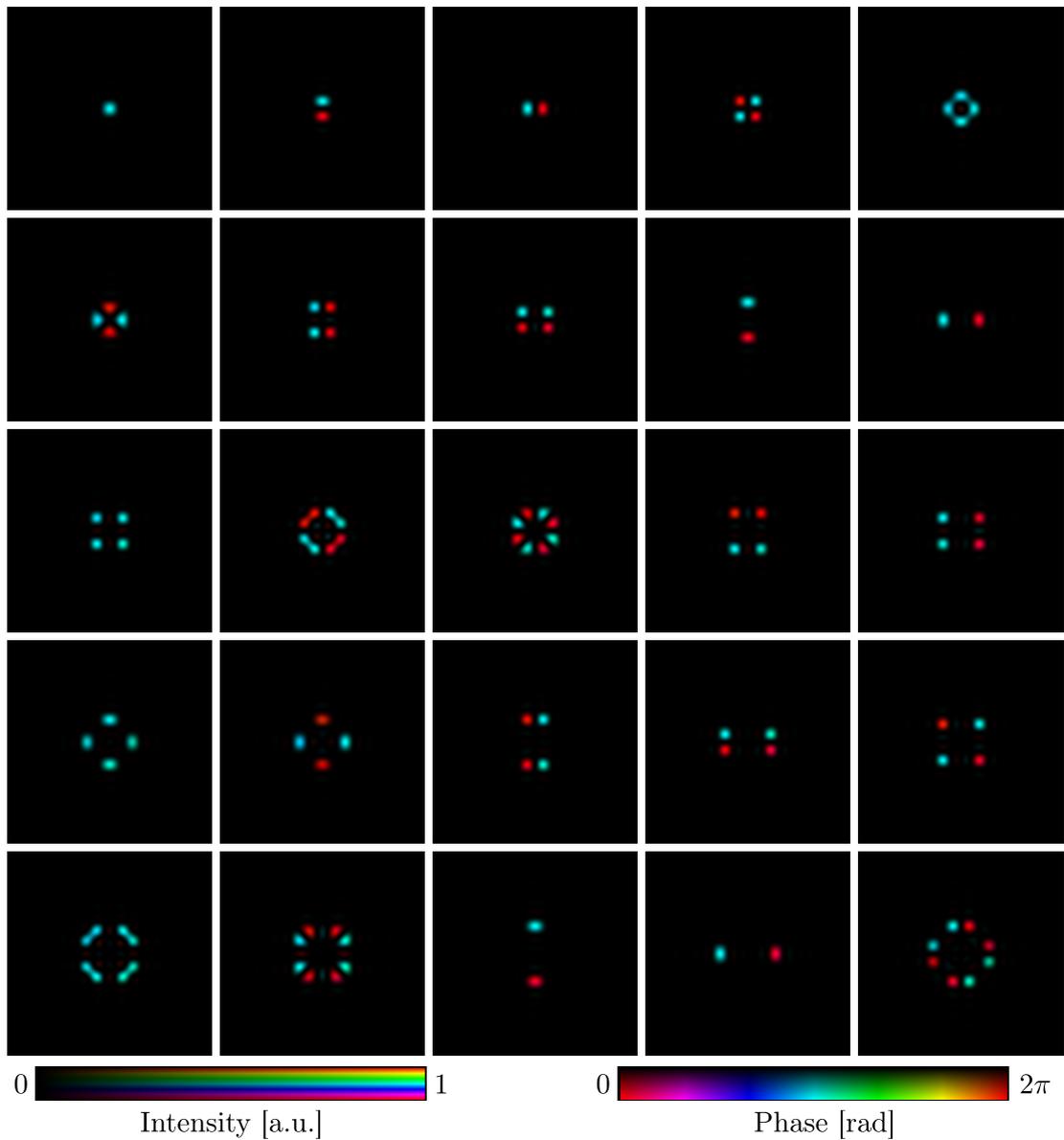
Figure 2.8: Reciprocal fields $\mathbb{E}_k$ of the first 25 optical eigenmodes with respect to a square region of interest in the focal plane. The mode number increases from left to right and from top to bottom. First row: Modes 1 to 5, second row: Modes 6 to 10 etc. The coordinate origin is located at the center of each image.
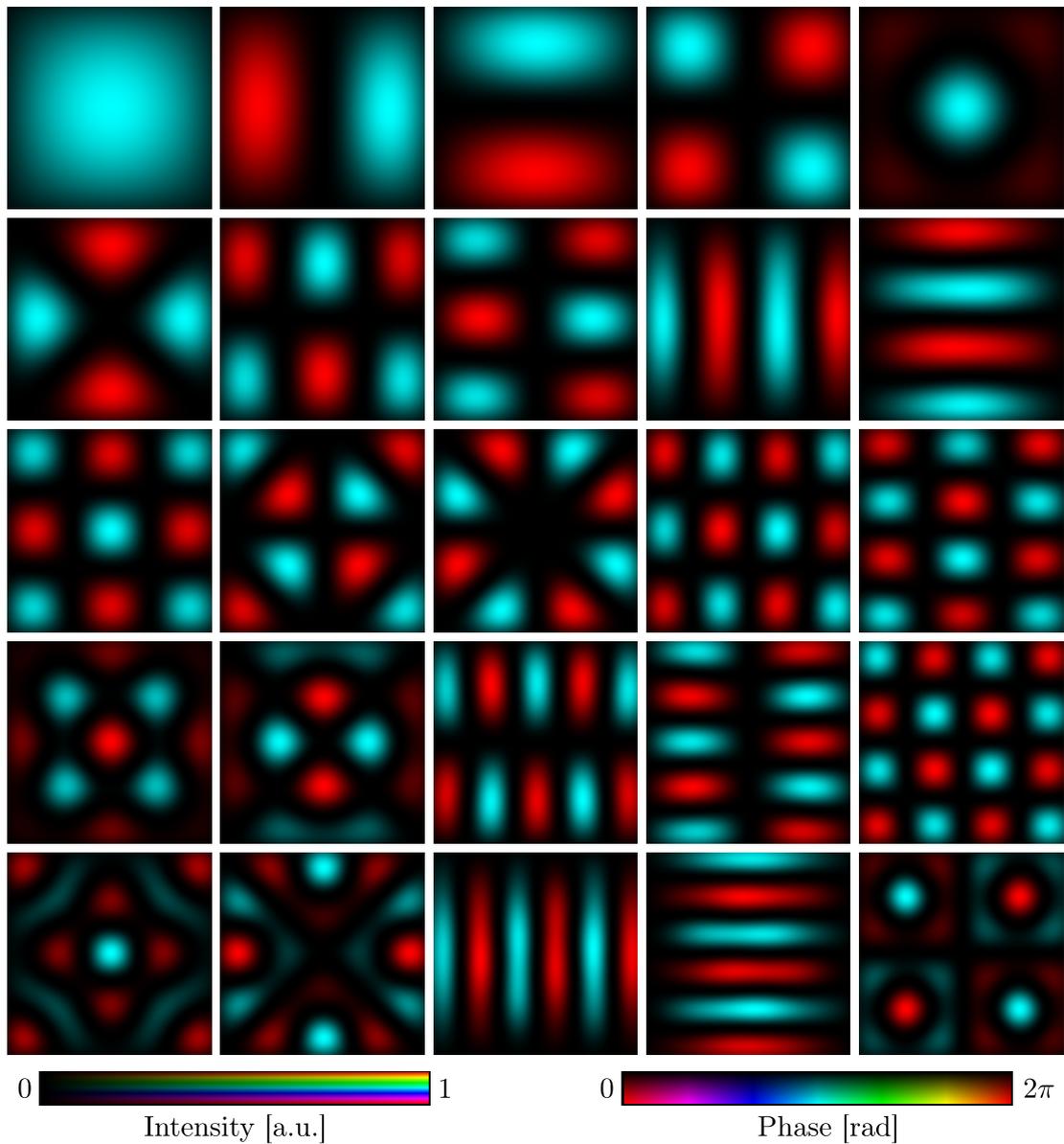
Figure 2.9: Focal fields of the first 25 optical eigenmodes in a square region of interest, resulting from the reciprocal fields in Figure 2.8. The coordinate system has its origin in the center of each picture. The mode number increases from left to right and from top to bottom. First row: Modes 1 to 5, second row: Modes 6 to 10 etc.

- The procedure of determining optical eigenmodes in the focal plane of a linear optical system as solutions to an intensity maximisation problem was outlined.

- Given that the initial test fields were sufficiently covering the system's degrees of freedom, the number of OEi with an intensity above the noise level corresponds to the number of available degrees of freedom.

- Using the OEi, operators can be constructed to determine the fields, that extremise quadratic measures, such as intensity, spot size, energy, or momentum, of the light field.

- The concept of OEi and operators to extremise certain properties of the light field is general for linear optical systems and can be applied to all quadratic measures of the field.

In order to give some examples, optical eigenmodes were furthermore calculated within a circular ROI in the focal plane of a lens and in a square ROI in the focal plane of a microscope objective. The former will be used in the next Chapter 3 to locally minimise the width of a focal spot and the latter will be employed in Chapters 4 and 5 to perform compressive hyperspectral imaging and coherent control of gold nanostructures.

Chapter 3

Minimising the width of a focal spot

In this chapter it is shown, how the optical eigenmode concept can be used extremise a measure of the light field. In particular, the width of a focal spot is locally minimised. The introduction in Section 3.1 reviews prior work on that topic and outlines possible applications of such spots. In Section 3.2 the principle of minimising the beam width using optical eigenmodes is explained. The experimental configuration to implement the spots is detailed in Section 3.3. In Section 3.4 minimsed focal spots are simulated and compared to their experimental realisations. As a simple application example, a selected spot is used to confocally scan pairs of holes in Section 3.5. Results and conclusions of this chapter are summarised in Section 3.6.

3.1 Minimised focal spots via pupil filters

Many photonic applications, such as optical lithography, optical data storage, optical trapping, or laser scanning imaging, are affected by the far field diffraction limit, imposing a restriction on the minimum possible size light can be focussed to (for more information one might also refer to Section 2.3). With respect to imaging, this limitation can be overcome in some cases by working in the near field [106, 107], using properties of fluorescent dyes [41, 90, 108], or applying numerical reconstruction methods [44]. Furthermore, negative refractive index materials, so called "superlenses", enable focussing of light below the diffraction limit for lithography and imaging [109–111]. But they have to be positioned directly on the sample, hence also operating in the near field.

However, if none of the above methods can be employed, by applying amplitude and phase modulations to the system's pupil it is still possible to obtain a focal spot that locally exhibits a size below what is commonly called the diffraction limit. Since the lectures of Luneburg [112], a considerable amount of theoretical work has been carried out to calculate pupil filter designs delivering a spot or

PSF of reduced size compared to the Airy-disk [113–119]. The most well known amongst these are probably the zone filters of Toraldo di Francia [116] and the continuous pupil functions of Frieden [117]. The basic finding in References 113–119 is that, using phase and intensity filters in the pupil of an optical system, its 2D focal spot, or point spread function (PSF) respectively, can be arbitrarily squeezed for the tradeoff of reduced intensity of the central peak and increased intensity of the sidelobes. Recently, this effect has also been termed "superoscillations" [120–125]. Investigations in 3D furthermore revealed that the spot can also be squeezed axially, but that there is a certain limit in three dimensions [126]. Usually a squeezing of the focal spot in the lateral direction results in an axial elongation and vice versa [126, 127]. Nevertheless, depending on the application a compromise can be made between size and intensity of the spot as well as the intensity and distance of the sidelobes. Like that pupil filters enable enhanced resolution or contrast in optical data storage [128, 129] and confocal imaging [38, 39, 130–140].

As mentioned above, using pupil filters it is in principle possible to abritrarily squeeze the focal spot or PSF at the expense of an increased sidelobe intensity and a decreased spot intensity. The high intensity sidelobes can also be moved away from the central peak, again reducing the intensity of the latter. With an arbitrarily powerful light source and a device for arbitrarily accurate beam shaping, it would still be possible to locally generate useful focal spots with subdiffractive extent. Unfortunately both are not available in reality. However, only few pupil modifications have been tested experimentally so far [38, 130, 131, 136, 141] and a systematic study about what type of spots can be experimentally realised is still lacking. This is partly due to the implementation of pupil filters as fabricated diffractive elements [38, 130, 131] and the cumbersome ways of calculating them. Based on the fact, that the goal is a narrowing of the focal width compared to the unobstructed pupil, it is possible to make clever approximations on suitable pupil functions [127, 135, 142]. However, this does not result in optimized designs. Available optimization methods use an initial decomposition of the pupil into a set of functions and determine their superposition such that the resulting focal spot fulfills given constraints. These constraints can be a number of chosen zeros in the focal plane [116, 119], a target function to approximate [117, 118], a desired focal width reduction [136], or a combination of multiple constraints such as focal width, Strehl ratio, and sidelobe distance and intensity [141, 143]. Given that the pupil is initially decomposed in a suitable manner, the pupil design required for the focal distribution to match a set of chosen zeros or a special target function can usually be calculated directly. But in that case the initial constraints already strongly influence the solution, as the focal function is forced into a very particular shape. Solving the problem with constraints on the focal width and/or other parameters requires iterative algorithms [136, 141, 143].

A drawback is that such approaches are time consuming and do not necessarily deliver the best possible solution.

Here, the recently developed *Optical Eigenmode* (OEi) method is used for the calculation part. This enables the high-performance determination of pupil functions delivering the smallest possible focal spot, which at the same time has the maximum possible intensity for that spot size [101]. The method only requires a single iteration, works for any pupil decomposition and system geometry, and the only constraint is a region of interest (ROI), within which the spot is minimized, thus placing very weak conditions on the particular shape of the focal spot. Experimentally, the OEi optimised pupil modifications are encoded on a spatial light modulator (SLM) as in References 136, 141. This renders the optical system highly flexible with the opportunity of carrying out an extensive study on the limitations of state-of-the-art beam shaping technique to implement pupil filters that generate minimised focal spots.

3.2 Minimizing the beam width using optical eigenmodes

To minimise the beam width it has to be measured in a defined way, of which the most common ones are discussed in Section 3.2.1. In Section 3.2.2 it is then shown how the beam width can be minimised using a superposition of optical eigenmodes resulting from a spot size operator.

3.2.1 Measuring the beam width

In order to minimise the beam width, one first needs to define a way to quantify it. A common method to measure the transversal width of an in z-direction propagating light beam is to chose an intensity gap and define the beam width as the diameter of the area, in which the beam intensity exceeds this gap. For the Full Width Half-Maximum (FWHM) measure this gap is chosen to be half of the maximum intensity $I_{\max}$. This is illustrated at the example of the Airy-disk in Figure 2.4a. For Gaussian beams a frequently used method is to define the beam radius as the distance from the beam axis, where the intensity drops to $1/e^2$ of $I_{\max}$. This measure corresponds to the standard deviation σ of the Gaussian beam's amplitude and doubling this value delivers the beam width.

A disadvantage of intensity gap based measures is that they can only be applied to beam shapes which feature a well defined single maximum. Thus another method that shall be mentioned here is the one of ISO Standard 11146, which is

based on the second order moment of the intensity distribution $I(x, y)$. Here the beam width w is defined as [144]

$$w = 4 \sqrt{\frac{\int_{\text{ROI}} I(x, y) \, \rho^2 \, d\sigma}{\int_{\text{ROI}} I(x, y) \, d\sigma}} \tag{3.1}$$

with $\int_{\text{ROI}}$ indicating the integration in a *region of interest* (ROI) and $d\sigma \equiv dxdy$. This method is also often referred to as the $D4\sigma$ method, because in the case of a Gaussian beam w equals 4 times the standard deviation σ of the intensity distribution $I(x, y)$ of the beam. The advantages of this measure compared to the FWHM or the $1/\text{e}^2$ method are that it can also be applied to more complicated beam shapes and that it takes into account, how quickly the intensity decays in the outer areas of the beam, which are below the chosen gap (e.g. the side maxima of the Airy disk in Figure 2.4).

3.2.2 The spot size operator

Apart of the already mentioned benefits, the definition of the beam width in Equation 3.1 has the advantage that it explicitly contains the electric field F in terms of the intensity $I = F F^*$. Using a decomposition

$$F = \sum_{k=1}^{M} b_k \, \mathbb{F}_k \tag{3.2}$$

of the field in the output plane of the system considered in Section 2.5.1 into the optical eigenmodes $\mathbb{F}_k$ from Equation 2.32, the beam width can be written as

$$w = 4 \sqrt{\frac{\mathbf{b}^\dagger \mathbf{M}^{(2)} \mathbf{b}}{\mathbf{b}^\dagger \mathbf{M}^{(0)} \mathbf{b}}}. \tag{3.3}$$

In Equation 3.3 the $M \times M$ elements of $\mathbf{M}^{(0)}$ are calculated with the optical eigenmodes $\mathbb{F}_k$ in analogy to Equation 2.28. The elements of the $M \times M$ operator $\mathbf{M}^{(2)}$ are defined as

$$M_{kl}^{(2)} = \int\limits_{\text{ROI}} \mathbb{F}_k \, \mathbb{F}_l^* \, \rho_2^2 \, d\sigma_2, \tag{3.4}$$

and $\mathbf{b}$ contains the coefficients b_k from Equation 3.2. The integration in Equation 3.4 is over a ROI in the output plane with $d\sigma_2 \equiv dx_2 dy_2$ and ρ_2 is the radial coordinate in that plane.

According to its definition also $\mathbf{M}^{(2)}$ is Hermitian, thus featuring orthogonal eigenvectors and real eigenvalues. If $\mathbf{b}$ in Equation 3.3 is one of the normalized

eigenvectors $\mathbf{v}_m^{(2)}$ of $\mathbf{M}^{(2)}$, then the denominator in Equation 3.3 is unity as the optical eigenmodes $\mathbb{F}_k$ are normalized. In that case the beam width w in Equation 3.3 equals four times the squareroot of the corresponding eigenvalue $\lambda_m^{(2)}$ of $\mathbf{M}^{(2)}$, which means that w is a monotone increasing function of $\lambda_m^{(2)}$. Hence the output field $F_{\min}$ with the smallest second order moment in the ROI is the one composed according to Equation 3.2 with the elements of the eigenvector $\mathbf{v}_{\min}^{(2)}$ of the smallest eigenvalue $\lambda_{\min}^{(2)}$. It can be obtained by using the same coefficients for the optical eigenmodes $\mathbb{E}_k$ in the input plane:

$$E_{\min} = \sum_{k=1}^{M} v_{\min,k}^{(2)} \, \mathbb{E}_k, \qquad (3.5)$$

$$F_{\min} = \sum_{k=1}^{M} v_{\min,k}^{(2)} \, \mathbb{F}_k. \qquad (3.6)$$

3.3 Setup & calibration

The setup used for the experiments contains an SLM system to implement intensity and phase modulation for the generation of beams with minimised focal width. An SLM is a liquid crystal display. To each of the display's pixels a voltage can be applied to change the orientation of the liquid crystals. This allows for the refractive index of the pixels to be controlled, hence enabling spatial phase modulation of the incident light. As there are little gaps between the pixels, not all the light undergoes modulation. This is why an SLM is usually operated in so called first order configuration. Therefore a blazed grating is encoded on the SLM, deflecting the modulated light into the first diffraction order, while the unmodulated light remains in the zeroth order. In the focal plane of a telescope the first order can be filtered out by an iris, which is blocking the other diffraction orders (higher orders exist as well due to the pixelation of the display). However, there is always at least a little interaction of the zeroth diffraction order with the first order [145]. This is tolerable for applications in which the first order is strong compared to the zeroth order. But it becomes problematic, when strong spatial intensity modulation is required, which is usually performed by deflecting unwanted light from the first into the zeroth order. As the experiments in this chapter depend on extensive intensity modulation, a configuration is chosen that employs two SLM displays, one for intensity and another for phase modulation.

For phase modulation an SLM display with a thick layer of parallel aligned liquid crystals is used. This enables phase modulation with almost no rotation of polarisation [146] and the thickness of the liquid crystal layer is sufficient to achieve phase modulation over a full wave cycle at visible wavelengths. The
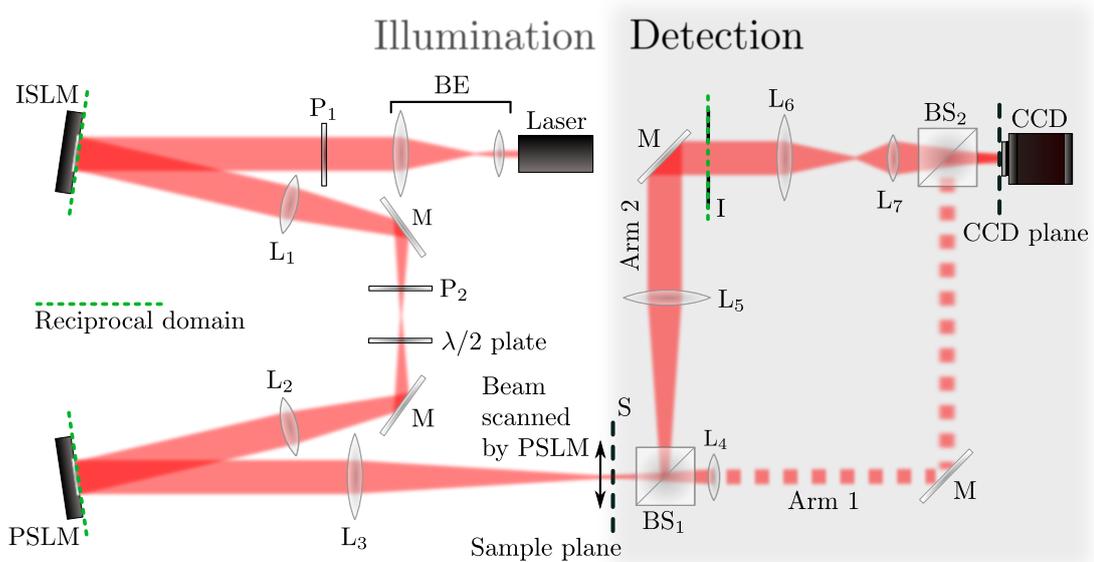
Figure 3.1: Experimental setup to create and analyse optimised focal spots and to perform confocal scanning imaging using these spots. BE: beam expander; P_n: polarisers; ISLM: intensity SLM; PSLM: phase SLM; M: mirror; BS_n: 50/50 beam splitters; I: iris; CCD: CCD camera. The lenses L_n have the following focal lengths f_n: $f_1 = f_2 = 400\,\text{mm}$, $f_3 = f_5 = 1\,\text{m}$, $f_6 = 500\,\text{mm}$, $f_7 = 100\,\text{mm}$.

display used for intensity modulation features vertically aligned liquid crystals, which mainly cause a rotation of polarisation. Hence, it can be used in combination with two crossed polarisers to achieve a spatial modulation of intensity. The layer of liquid crystals of this display is significantly thinner, such that only little phase modulation occurs parallel to the polarisation change. This is accounted for during calibration of the system. Decoupling the modulation of intensity and phase avoids an intensity increase in the zeroth order, which would interfer with the first order. This configuration is described in detail in Section 3.3.1 and the calibration of the SLM system is outlined in Section 3.3.2.

3.3.1 Setup

The experimental setup to generate OEi optimized focal spots and to use them for confocal scanning imaging is depicted in Figure 3.1. It can be roughly subdivided into an illumination part and a detection part.

The illumination part features an 8-bit Holoeye HEO 1080 P dual display liquid crystal spatial light modulator system. The first SLM display ISLM in conjunction with two crossed polarisers P_1 and P_2 performs intensity modulation of the beam and the second display PSLM modulates the phase. For this, the

beam of a linearily polarized HeNe laser (emission wavelength $\lambda = 633\,\text{nm}$) is expanded such that it visually fills the active area of the ISLM with homogeneous intensity. The polariser P_1 makes sure the polarisation is correct. Depending on the encoded 8-bit value the ISLM turns the polarisation of the light such that the intensity can be spatially modulated via the polariser P_2. Using a $1:1$ telescope consisting of lenses L_1 and L_2, the ISLM is imaged onto the PSLM and the $\lambda/2$ wave plate turns the polarisation as it is required for phase modulation by the PSLM. The by both displays complex modulated light is then focussed by lens L_3 in the sample plane. The distances in the setup are chosen such that with respect to the sample plane, which is considered to be in space domain, the SLM displays are situated in the reciprocal domain, indicated by dotted lines in Figure 3.1. There should be made some further remarks about the SLM system:

- Of the display's $1920\,\text{pixel} \times 1080\,\text{pixel}$ array the central circular area of $1080\,\text{pixel}$ in diameter is used. The pixel pitch is $8\,\mu\text{m}$, hence the used diameter is $8.64\,\text{mm}$.

- The desired intensity and phase modulations are encoded in 32-bit RGB images, of which the blue channel is displayed on the ISLM and the green channel on the PSLM, hence featuring 8-bit per display.

- A calibration was carried out for both displays such that their 8-bit range corresponds to a linear real amplitude range from 0 to 1 and a linear phase range from 0 to 2π respectively (see Section 3.3.2 for calibration curves).

- Aberrations due to unevenness of the display surfaces were corrected by a wavefront correction method similiar to the one described in Reference 147.

- The ISLM not only rotates the polarization of the incident light but at the same time induces a phase shift. This phase shift dependency was measured with respect to the displayed 8-bit value and is subtracted from the phase displayed on the PSLM (see also Section 3.3.2).

- The PSLM was used in standard first order configuration [148] while the ISLM was used in zeroth order.

- Ideally the lenses L_1 and L_2 should image a pixel coordinate on the ISLM to the same pixel coordinate on the PSLM. By displaying an alignment cross on both displays we ensure a pixel matching of $\pm 2\,\text{pixel}$. This corresponds to a relative error of $< 0.2\,\%$ and can be neglected if the displayed mask does not exhibit such fine features.

The beam path of the detection part is divided by a beam splitter BS_1 into two arms, Arm 1 and Arm 2, of which only one is used at a time. In Arm 1, whose beam path is dotted in Figure 3.1, the sample plane is imaged via lens L_4 with $10\times$ magnification onto a CCD camera (Basler pilot piA640-210gm,

$648\,\text{pixel} \times 488\,\text{pixel}$ resolution, $7.4\,\mu\text{m}$ pixel pitch). This enables analysation of the focal spot with a resolution of $0.74\,\mu\text{m}$ per camera pixel. Arm 2 is utilized for the scanning imaging. The light transmitted through the sample is collected by lens L_5, which has identical NA as L_3. An iris I that is positioned in the back focal plane of L_5 truncates the beam to a diameter identical to the one incident on the PSLM. This ensures that L_3 and L_5 also have the same effective NA. The lenses L_6 and L_7 and their positions are selected such that the sample plane is imaged with $3\times$ magnification onto the camera. An image is then acquired in a confocal raster scanning fashion by deflecting the beam over the sample with the PSLM and averaging the transmitted intensity on the CCD in a small region that moves according to the beam deflection. This procedure is described in more detail in Section 3.5.1.2.

3.3.2 Calibration of the SLM system

The manufacturer of the SLM system provides software to modify γ-curves stored on the controller. These γ-curves translate 8-bit values sent to the controller into a voltage that is applied to the liquid crystal pixel, thus translating a gray scale value into a phase shift and a rotation of polarization. Here it is described how the γ-curves are changed such that for the linear gray scale range from 0 to 255 the devices deliver a linear amplitude modulation and phase shift respectively.

To calibrate the amplitude modulation the light after passing the second polariser P_2 is focussed onto a photo diode (PD). Then the 8-bit values encoded on the ISLM are varied in steps of 1 from 0 to 255 and the intensity transmitted through P_2 is collected with the PD. The red curve in Figure 3.2a shows the monitored behaviour of the normalised amplitude, which is the squareroot of the normalized intensity. From this data a new γ-curve was calculated and transferred to the SLM controller. Repeating the measurement now delivers a linear amplitude modulation as depicted by the blue curve in Figure 3.2a.

Unfortunately, the amplitude modulation also involves a phase shift that needs to be compensated for. This phase shift can be measured, with the polariser P_2 not in place, by putting a double slit in front of the SLM display and changing the gray scale value on one of the slits while keeping it constant on the other one. The induced phase shift is then derived from the shift of the interference fringes of the double slit diffraction pattern. Each column of the picture in Figure 3.2b corresponds to a profile in $x-$direction through the double slit interference pattern, which was captured with a CCD camera. Due to the orientation of the picture the shift of the fringes occurs from top to bottom. From a sine fit to each of the columns the phase shift is obtained and plotted as the red curve in Figure 3.2c. The coefficients from a 3rd order polynomial fit to this data are then used to
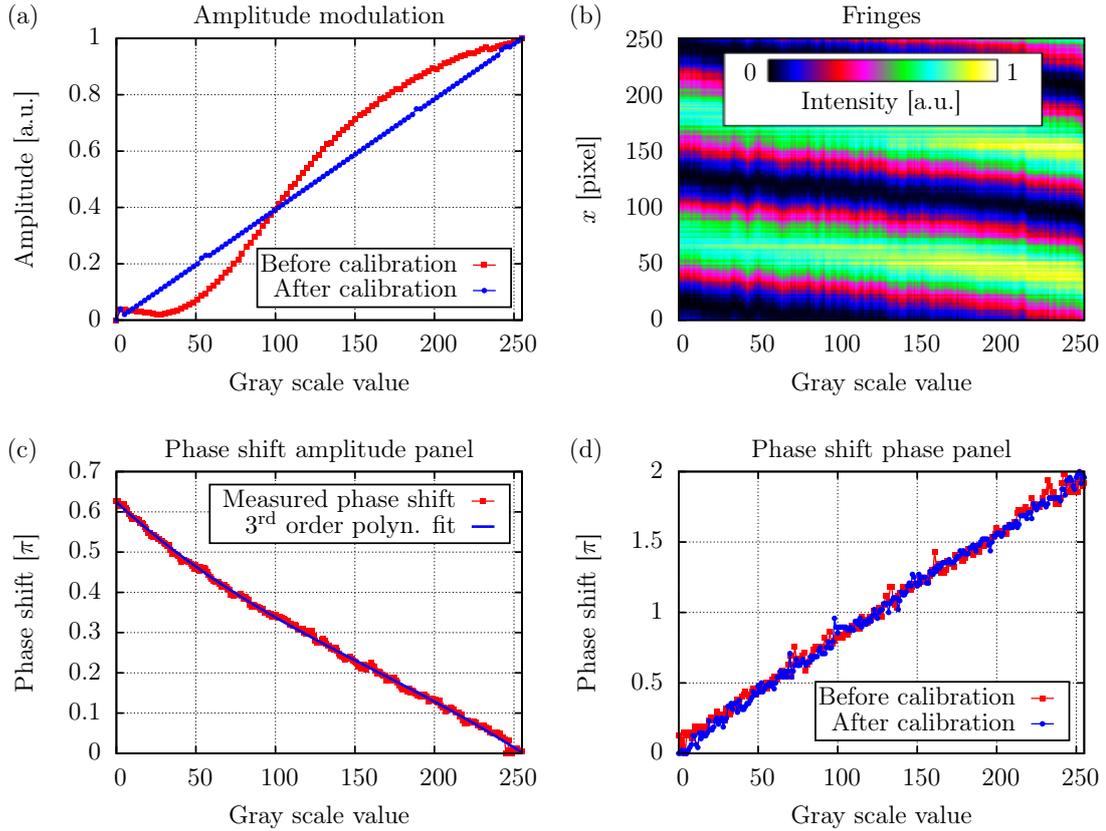
Figure 3.2: (a) Amplitude modulation depending on the gray scale value on the ISLM before and after calibration. (b) Profiles in $x-$direction through the double slit interference fringes depending on the gray scale value encoded on one of the slits (each column of the picture represents one profile). (c) Phase shift induced by the ISLM. (d) Phase shift of the PSLM before and after calibration.

calculate the phase shift depending on the gray scale value encoded on the ISLM and substract this shift from the phase which gets encoded on the PSLM.

The phase dependency of the PSLM is also calibrated with a double slit configuration. In fact, the double slit can be encoded on the ISLM and then the gray scale value encoded on the PSLM is varied for one of the slits. The procedure to obtain the phase shift from the fringe pattern is completely identical as described for the phase shift of the ISLM. Figure 3.2d shows the phase shift measured before and after calibration. Obviously the phase was behaving pretty linear beforehand. However, after calibration the 0 to 2π range is fully used which did not seem to be completely the case before.

3.4 Minimized focal spots

As mentioned earlier, shaping the reciprocal field with arbitrary precision in an unaberrated system would enable arbitrarily small focal spots with the sidelobes arbitrarily far away from the spot. The decreased intensity of the central spot could to a certain extend be compensated by a powerful light source. However, in reality every optical system and especially the light shaping SLMs themselves are aberrated and the light shaping is not perfect. The SLM systems can be calibrated with a finite precision as described in Section 3.3.2. Furthermore, using wave front correction methods, aberrations can be sensed with certain accuracy and they can be compensated taking them into account in the phase shaping part. It has been analysed in theory that smaller and dimmer central spots require more precise light shaping [149]. So it is expected that in a real system the focal spot size can be reduced until the size and intensity of the spot reaches a lower limit, at which the precision of the system is insufficient to produce that spot. To determine this limit for the setup decribed in Section 3.3.1 the following road is taken in this work:

1. Focal spots and the reciprocal fields to generate them are determined in theory for various spot sizes and intensities.

2. The reciprocal fields are encoded on the SLM system of the setup and the resulting focal spots are acquired.

3. The sizes, intensities, and some other parameters of interest of the simulated and experimentally acquired spots are measured and theory and experiment are compared.

In the following Section 3.4.1 it is described how the reciprocal and focal fields are obtained in simulations. The methods to quantify the relevant spot parameters are explained in Section 3.4.2 and the results are presented in Section 3.4.3.

3.4.1 Determining OEi optimized reciprocal and focal fields

In order to generate minimized focal spots, the OEi optimization method is applied in simulations and then the obtained reciprocal fields are encoded on the SLM system. Some simulated OEi for this system have already been presented in Section 2.5.2. Here these simulations are explained in more detail and including the spot minimisation procedure. In the first step, the input field $E(\mathbf{r}_1)$ in the reciprocal domain is decomposed into N fields E_i. As the optimised focal spots should have a radial symmetry, the utilised SLM area of 1080 pixel diameter is decomposed into $N = 540$ non overlapping rings $E_i(\rho_1)$ of 1 pixel width, where

ρ_1 denotes the radial coordinate. Like this all of the system's radial degrees of freedom are employed. Using 8-bit dynamic range for intensity and phase, as permitted by the SLM system, each of the fields $E_i(\rho_1)$ is numerically focussed using the scalar radial symmetric representation of Huygen's integral in Section 2.2.4. The focal plane was simulated with 244 pixel and a pixel pitch of 0.74 µm, which corresponds to the field one would obtain on the CCD camera through Arm 1 of the setup.

Then the resulting 540 focal fields $F_i(\rho_2)$ were used to calculate optical eigenmodes $\mathbb{F}_k$ and $\mathbb{E}_k$ in the focal plane and the reciprocal domain as described in Section 2.5.1. This was done for the ROI radius R_2 varied in steps of $0.03\,w_{\text{Airy}}$ between $0.09\,w_{\text{Airy}}$ and $2.30\,w_{\text{Airy}}$. The width w_{Airy} of the Airy disk can be calculated as FWHM from the Abbe limit. For the described setup with a beam diameter of 8.64 mm and a lens of 1 m focal length the effective NA is $4.32 \cdot 10^{-3}$ resulting in $w_{\text{Airy}} = 73.3$ µm.

To minimise the spot size while keeping the spot intensity maximum, the M most efficient OEi were selected with the in Section 2.5.1 discussed threshold chosen to be $T = 10^{-p}$ with $p = 1, 2, \ldots, 6$. Using the M selected OEi, the focal width was minimised as described in Section 3.2. This delivers optimised focal fields $F_{\min}$ and reciprocal fields $E_{\min}$. The fields $E_{\min}$ are then azimuthally interpolated to $1080\,\text{pixel} \times 1080\,\text{pixel}$ for encoding on the SLM system and the fields $F_{\min}$ are interpolated to $488\,\text{pixel} \times 488\,\text{pixel}$, corresponding to the CCD's central area. Figures 3.3a to 3.3j show some examples for reciprocal fields and some simulated example spots are depicted in Figures 3.3k to 3.3o.

By varying the radius R_2 of the ROI the constraints for minimising the second order moment of the beam are varied, thus delivering focal spots of various sizes. Furthermore, the variation of the intensity threshold T causes that OEi of different efficiency are taken into account for the optimisation, which results in spots of diverse intensities. The ways to characterise the varying features of the optimised focal spots is discussed in the next Section 3.4.2.

3.4.2 Spot parameters

As mentioned earlier, decreasing the width of a focal spot results in an increased sidelobe intensity and a decreased spot intensity. As an example for such a spot with more pronounced sidelobes one might have a look at e.g. Figures 3.3m and 3.3r. Furthermore, the spot intensity decreases whith increasing distance between sidelobes and central spot. Thus the interesting parameters of minimized focal spots are the spot size, the spot intensity, the distance to the sidelobes, and the sidelobe intensity. For the latter it is actually more relevant, how intense the sidelobes are compared to the central spot, i.e. how strong they disturb the

central spot when using it in photonic applications. These four properties of the spots are quantified in the following manner in the intensity distributions $|F_{\min}|^2$ of the optimised fields $F_{\min}$:

Spot size   The width w_{spot} of the central spot is measured as the FWHM obtained from a 2D Gaussian fit.

Spot intensity   The spot intensity is quantified as the Strehl ratio S, which is defined as the quotient of the peak intensities of the spot and the Airy disk [150].

Distance to the sidelobes   The distance d_{SL} to the sidelobes is measured between the central spot's peak and the peak of the nearest sidelobe of at least $10\,\%$ of the spot's peak intensity.

Spot intensity relative to the sidelobe intensity   The relative spot intensity I_{rel} is quantified as the ratio between the peak intensities of the central spot and the nearest sidelobe of at least $10\,\%$ of the spot's peak intensity.

The spot parameters obtained for the simulated and experimentally acquired spots are presented in the next Section 3.4.3.

3.4.3 Results

In Section 3.4.1 it was described how OEi optimized focal fields and their corresponding reciprocal fields are obtained in simulations. To determine the experimental pendants to the theory, the reciprocal fields are encoded on the SLM system in the setup described in Section 3.3.1. Then for each of the fields the resulting intensity distribution is captured on the CCD camera via Arm 1 of the setup. Some examples for experimentally captured spots are shown in Figures 3.3p to 3.3t. For each simulated and experimentally acquired focal spot the parameters w_{spot}, S, d_{SL}, and I_{rel} are determined as described in Section 3.4.2. The parameters of the example spots in Figure 3.3 are listed in Table 3.1 (the parameters R_{abs} and R_{rel} are introduced in Section 3.5).

The measured spot parameters for all spots are plotted in Figures 3.4a to 3.4f for the simulated (Figures 3.4a, 3.4c, and 3.4e) and experimentally captured spots (Figures 3.4b, 3.4d, and 3.4f). In each of the plots the horizontal axis depicts the spot size w_{spot} relative to the FWHM $w_{\text{Airy}} = 73.3\,\mu\text{m}$ of the Airy disk. On the vertical axis the distance d_{SL} to the sidelobes is also scaled to w_{Airy}. It should
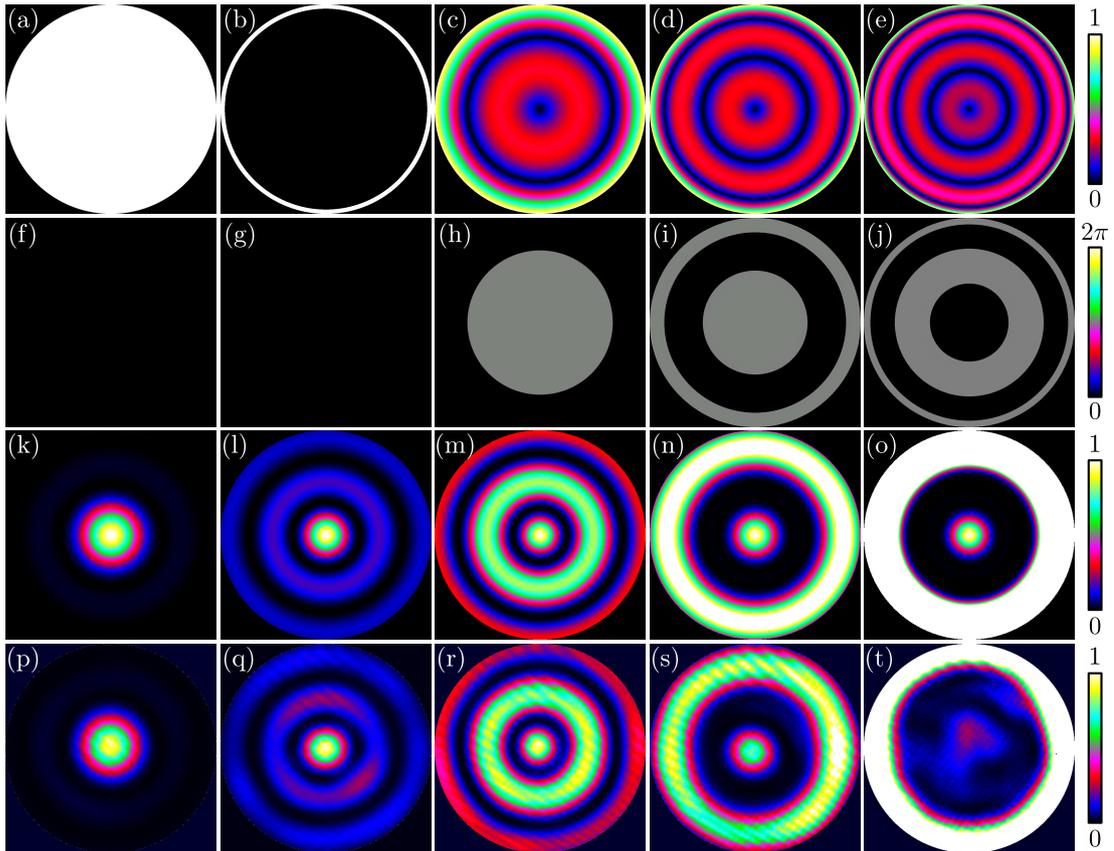
Figure 3.3: (a-e) Real amplitude and (f-j) phase of fields $E(\rho_1)$ in the SLM plane, that correspond to (a,f) the Airy disk, (b,g) a Bessel beam, and (c-e, h-j) three example spots: (c,h) Spot 1, (d,i) Spot 2, and (e,j) Spot 3. (k-o) Simulated and (p-t) experimentally resulting normalised itensity distributions $|F(\rho_2)|^2$ in the focal plane: (k,p) Airy disk, (l,q) Bessel beam, (m,r) Spot 1, (n,s) Spot 2, and (o,t) Spot 3.

be noted that, compared to the plots of the simulations, the experimental graphs have a smaller range of the horizontal axes, but the same scaling relationship. The colour codings in Figures 3.4a to 3.4f indicate the number M of OEi used in the optimization (Figures 3.4a and 3.4 b), the Strehl ratio S (Figures 3.4c and 3.4d), and the spot intensity I_{rel} relative to the sidelobe intensity (Figures 3.4e and 3.4f).

In Figures 3.4a and 3.4b it is observed that with an increasing number M of modes the sidelobes can be pushed further away from a central spot of identical size. At the same time the Strehl ratio S in Figures 3.4c and 3.4d decreases. The same applies for the relative spot intensity I_{rel} in Figures 3.4e and 3.4f. This is due to the lower efficiency of the higher order OEi (see Sections 2.4 and 2.5.1). Furthermore, S and I_{rel} decrease with decreasing spotsize w_{spot}. All these findings agree with the qualitative rules stated at the beginning of Section 3.4.2.
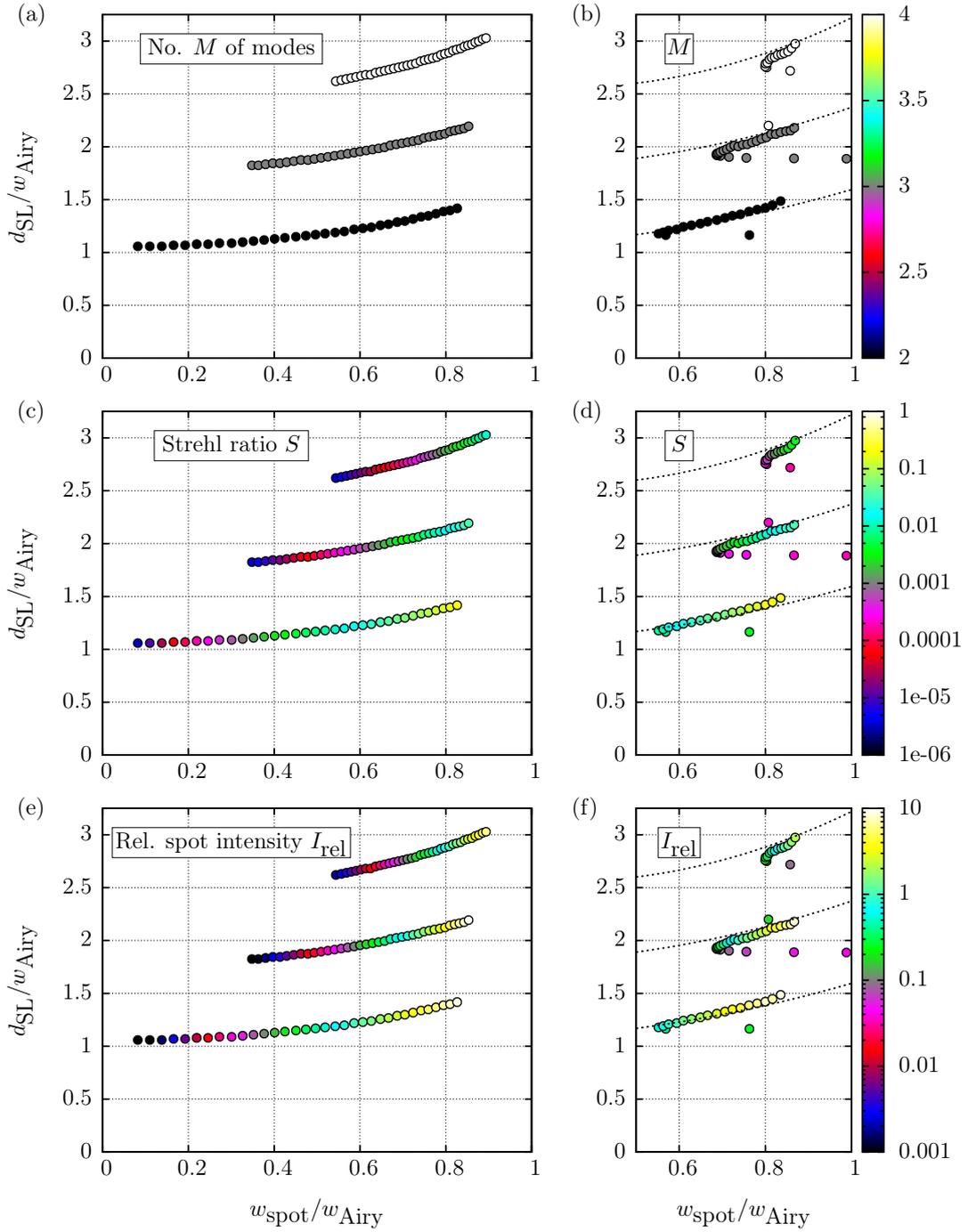
Figure 3.4: (a,c,e) Simulated and (b,d,f) experimentally obtained spot parameters quantified according to Section 3.4.2. In the individual plots the colour represents (a,b) the number M of modes, (c,d) the Strehl ratio S, and (e,f) the relative spot intensity I_{rel} in dependence on the spot size w_{spot} and the distance d_{SL} between spot and sidelobes. For better orientation, the dashed lines in the experimental plots indicate the trend of the simulations.

Parameter		Airy disk	Bessel beam	Spot 1	Spot 2	Spot 3
M		–	–	2	3	4
$w_{\text{spot}}/w_{\text{Airy}}$	Sim	1	0.71	0.61	0.71	0.60
	Exp	1	0.72	0.61	0.74	–
$d_{\text{SL}}/w_{\text{Airy}}$	Sim	–	1.28	1.21	1.84	1.62
	Exp	–	1.21	1.25	1.85	–
S	Sim	1	0.0096	0.022	0.0038	$1.7 \cdot 10^{-5}$
	Exp	1	0.0064	0.021	0.0037	–
I_{rel}	Sim	–	6.4	1.2	0.88	0.0083
	Exp	–	4.7	1.3	0.91	–
$R_{\text{abs}} \, [\mu m]$	Sim	83	70	65	68	61
R_{rel}	Sim	1	1.19	1.28	1.22	1.36

Table 3.1: Simulated (Sim) and experimentally (Exp) measured spot parameters for the Airy disk, a Bessel beam, and three example spots, which are illustrated in Figures 3.3m to 3.3o (simulation) and Figures 3.3r to 3.3t (experiment).

Comparing the simulated results in Figures 3.4a, 3.4c, and 3.4e and the experimental ones in Figures 3.4b, 3.4d, and 3.4f, good agreement is observed for Strehl ratios $S > 0.003$ and relative spot intensities $I_{\text{rel}} > 0.9$. The more the spot intensity drops below these values, the larger the mismatch between simulation and experiment. Consequently the spots in Figures 3.3r and 3.3s with $S = 0.021$ and $S = 0.0037$ also visually agree with their simulated counter parts in Figures 3.3m and 3.3n. On the contrary in Figure 3.3t, which should show a spot with simulated Strehl ratio $S = 1.7 \cdot 10^{-5}$, no well defined central peak exists.

As the simulations have been carried out with the actual SLM's bit depth and resolution, the lack of agreement between simulations and experiment for low spot intensities is not due to the pixelation and limited dynamic range of the SLM system. Hence it must be due to residual noise and aberrations in the system. The beam shaping process itself might not be accurate enough e.g. due to pixel noise or the calibrations not leading to the required precision. Furthermore, there might be residual aberrations which can not be entirely cancelled out by the wavefront correction. Thus in future results could be improved using more accurate beam shaping devices as well as more advanced calibration and aberration correction methods. For the system and methods that were applied here, Strehl ratios $S \approx 0.004$ and relative spot intensities $I_{\text{rel}} \approx 0.9$ seem to be the lower limit for reliably delivering minimised focal spots.

3.5 Confocal imaging with minimized focal spots

To show a possible application of the OEi minimised focal spots, one of them is utilised to improve the Rayleigh resolution in confocal raster scanning imaging. In Section 3.5.1 the basics of confocal imaging are discussed. Furthermore, it is described how confocal imaging can be performed in the used setup and how this process is simulated. In Section 3.5.2 confocal resolution limits with conventional focal spots are discussed and determined for the OEi optimised spots. The results from confocal scans with a selected minimised spot are presented in Section 3.5.3 and compared to scans with the Airy disk and a Bessel beam.

3.5.1 The imaging process and its simulation

In conventional confocal laser scanning microscopy either a focused beam is scanned over the sample using a scanning mirror or the sample is scanned through the beam on a translation stage [93]. The beam-sample interaction is imaged onto a pinhole in front of a detector to cancel out scattering light from outside the focal volume. An image is then composed from the intensities acquired at each scanning coordinate. If the beam is scanned over the sample, it needs to be descanned for detection by sending it back over the same scanning mirror. Otherwise the pinhole needs to be moved according to the displacement of the beam.

3.5.1.1 Confocal imaging with the utilised setup

To perform confocal imaging with the setup in Figure 3.1, the beam is raster scanned over the sample using the SLM system. The light transmitted through the sample is then detected with the CCD camera via Arm 2 of the setup for each point of the scan.

More precisely, adding a linear phase gradient $\phi = k_x x_1 + k_y y_1$ to the phase which is encoded on the PSLM causes a displacement of the beam in the sample plane. Like that the PSLM can effectively be used to substitute a scanning mirror. The displacement of the beam depending on the deflection k_x, k_y is calibrated beforehand without the sample in place. Therefore an image of the beam is captured on the CCD for each k_x, k_y and the beam position is determined as the center of a 2D Gaussian fit. For confocal scans the transmitted intensity is then averaged in a $3\,\text{pixel} \times 3\,\text{pixel}$ square on the CCD centered at the current beam position. This square is small compared to the diffraction limited focal spot featuring a FWHM of about $30\,\text{pixel}$. An image is then composed from the intensities acquired for each deflection.

3.5.1.2 Simulation of the imaging process

To simulate the scanning process described in Section 3.5.1.1, the transmissive sample is simulated as a binary distribution $B(x_2, y_2)$ that is 1 in the sample's transparent areas and 0 in the opaque ones. The spatial intensity distribution $I_c(x_c, y_c)$ on the CCD is then simulated as follows for each scanning position:

1. The complex field $A(x_2, y_2)$ in the sample plane is the illuminating field $F(x_2, y_2)$ modulated with the transmission $B(x_2, y_2)$ of the sample:

$$A(x_2, y_2) = F(x_2, y_2)\, B(x_2, y_2). \tag{3.7}$$

2. The detection part of the setup is coherent. Thus the intensity $I_c(x_c, y_c)$ on the CCD is given by the square of the complex convolution of Equation 3.7 with the amplitude point spread function APSF of the detection part [84]:

$$I_c(x_c, y_c) = \left| \left[F(x_2, y_2)\, S(x_2, y_2) \right] * \mathrm{APSF} \right|^2. \tag{3.8}$$

As APSF the complex field of the Airy disk is used.

3.5.2 Confocal resolution limits

To determine whether or not a focal spot is suitable for imaging and improves the resolution over a conventional focus is not trivial, also with knowledge of the spot parameters determined in Section 3.4.3. A small central spot is unusable if its intensity is too low compared to the surrounding sidelobes and/or these sidelobes are too close to the central spot. Thus it is necessary to investigate a spot's imaging performance by the imaging process itself. Usually resolution capabilities of an imaging system are quantified by considering the imaging of simple objects. For an incoherent imaging system it is sufficient to measure the width of the image of a single point, hence the width of the PSF of the system. However, in the experiments carried out in this work the detection process is coherent. Thus it is necessary to investigate at least two sample points next to each other in order to correctly deal with interference [93]. The resolution limit is then defined as the minimum distance between the two points, that can just be resolved. According to the Rayleigh criterion this is the case if the contrast between the two imaged points amounts at least 26.5 % [84].

To quantify the two-point resolution with the OEi minimised spots, the scan along a 220 µm long line through two transmissive holes was simulated as described in Section 3.5.1.2. The step width between the scanning positions was
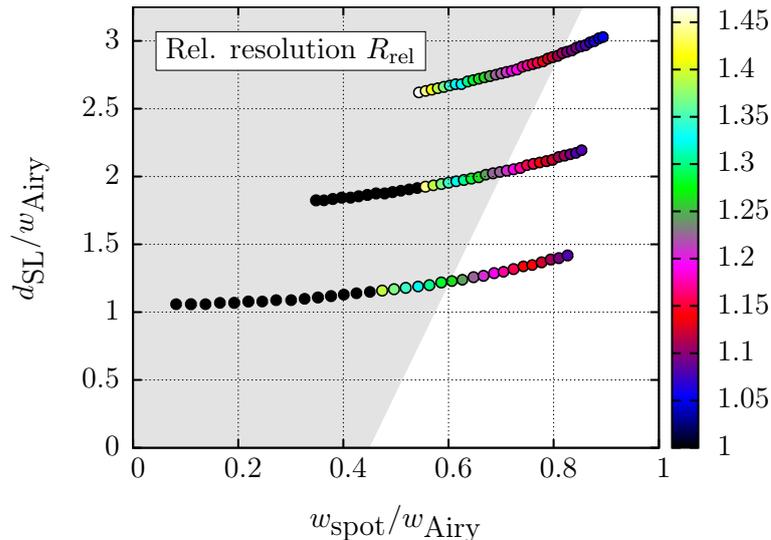
Figure 3.5: Simulated relative resolution in dependence on the spot size w_{spot} and the distance d_{SL} between spot and sidelobes. The white background roughly indicates the area of the spots, which can reliably be produced experimentally (compare experimental data in Figure 3.4).

chosen to be $1\,\mu\mathrm{m}$ and the separation between the holes was varied in steps of $1\,\mu\mathrm{m}$ as well. The absolute two point resolution limit R_{abs} was then quantified as the minimum, according to the Rayleigh criterion resolvable, distance between the hole centres. This was then scaled as a "resolution gain" in the way $R_{\mathrm{rel}} = R_{\mathrm{abs,Airy}}/R_{\mathrm{abs,spot}}$ to the absolute resolution limit $R_{\mathrm{abs,Airy}}$ when scanning with the Airy disk. Thus a value of $R_{\mathrm{rel}} = 2$ would correspond to twofold increased resolution over the conventional confocal resolution $R_{\mathrm{abs,Airy}}$. The two point Rayleigh resolution limit of the system for coherent confocal imaging with the Airy disk is defined by $R_{\mathrm{abs,Airy}} = 0.56\,\lambda/\mathrm{NA}$ [94], which results in a resolution of $82.1\,\mu\mathrm{m}$ with the already in Section 3.4.1 calculated effective NA of $4.32 \cdot 10^{-3}$.

The colour coding in Figure 3.5 depicts the obtained two point resolutions R_{rel} in dependence on the spot size w_{spot} and the distance d_{SL} to the sidelobes. Furthermore, the absolute and relative resolutions R_{abs} and R_{rel} for the spots illustrated in Figure 3.3 are listed in Table 3.1. The simulated relative resolution R_{rel} in Figure 3.5 generally decreases with decreasing spot size and increasing distance to the sidelobes. But at some point this effect stops due to a parameter combination in which the sidelobes are too close to the spot and/or the relative spot intensity I_{rel} is too low to resolve the two simulated holes with sufficient contrast (these are the black circles in the plot, which correspond to no resolution gain).

The interesting question is which resolution gain is obtainedable with the spots that can be generated experimentally. These spots are located in the white area

in Figure 3.5, while the spots in the grayed region did not match with their simulations. So the resolution gain that can be expected is somewhere between 1.25 and 1.3. In the next Section 3.5.3 an OEi minimised spot it used for confocal imaging of a test target to confirm these numbers.

3.5.3 Results

Here the suitability of OEi optimised focal spots for confocal imaging is analysed experimentally in raster scans of a thin in-focus object. The results are compared to simulations. More precisely, a photo mask (fabricated by Circuit Graphics, Essex, UK) featuring pairs of $10\,\mu m$ diameter transmissive holes on black film with hole separations d_{hol} varying in steps of $1\,\mu m$ was scanned as described in Section 3.5.1 (many thanks to Rob Marchington at this point for designing and ordering the mask). Scans were carried out with the Airy disk, a Bessel beam, and an optimised focal spot. For the latter, Spot 1 was used, whose intensity distribution is depicted in Figure 3.3r and whose parameters are listed in Table 3.1. This spot should give a significant resolution gain in the Rayleigh sense and its experimentally measured parameters did not show noticable disagreement with the simulations. The scanning was performed over a $220\,\mu m \times 110\,\mu m$ sized area at 64×32 uniformly spaced points for hole separations of $d_{\text{hol}} = 83\,\mu m$, $d_{\text{hol}} = 70\,\mu m$, and $d_{\text{hol}} = 65\,\mu m$. These separations correspond to the simulated two point resolution limits of the Airy disk, the Bessel beam, and Spot 1, as noted in Table 3.1.

The top row of pictures in Figure 3.6 shows the pairs of transmissive holes imaged with a widefield microscope (Nikon ECLIPSE Ti-S, Objective: Nikon Plan Fluor, $40\times/0.75$). Furthermore, Figure 3.6 illustrates for each of the hole pairs the simulated and experimentally obtained intensity distributions resulting from scans with the Airy disk, the Bessel beam, and Spot 1. Figures 3.7a to 3.7f depict profiles along a horizontal line through the simulated (Figures 3.7a, 3.7c, and 3.7e) and experimentally acquired intensity images (Figures 3.7b, 3.7d, and 3.7f). For each of the utlized scanning spots the key in Figures 3.7a to 3.7f features the contrast C measured between the smaller of the two main maxima and the central minimum.

The simulated and experimentally acquired intensity distributions and profiles look similar and the contrast values of simulation and experiment are in reasonable agreement. The results in Figures 3.7b, 3.7d, and 3.7f show that within a few percent of uncertainty the Rayleigh resolution criterion is experimentally fulfilled for $d_{\text{hol}} = 83\,\mu m$ by the Airy disk, $d_{\text{hol}} = 70\,\mu m$ for the Bessel beam, and $d_{\text{hol}} = 65\,\mu m$ when scanning with Spot 1. This is in agreement with the simulated values in Table 3.1. According to these values, for confocal imaging with coherent
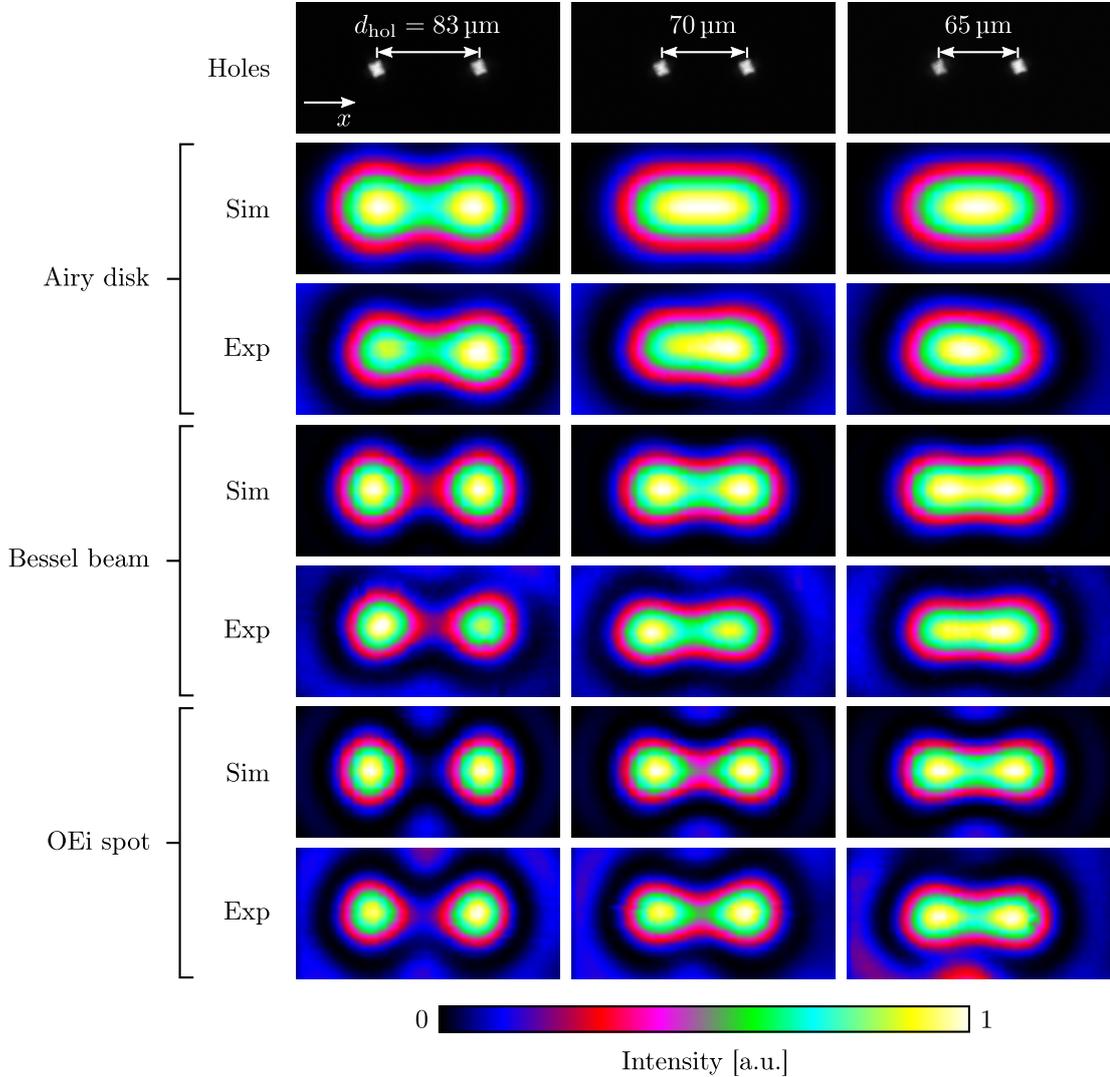
Figure 3.6: The first row of pictures shows images of the pairs of 10 μm sized holes with separations of $d_{\mathrm{hol}} = 83$ μm, $d_{\mathrm{hol}} = 70$ μm, and $d_{\mathrm{hol}} = 65$ μm. The remaining pictures depict simulated and experimentally acquired intensity distributions resulting from scanning the hole pairs with the Airy disk, a Bessel beam, and an OEi optimized spot (Spot 1). See also Figure 3.7 for profiles in $x-$direction through the diffraction patterns and resulting contrast values.
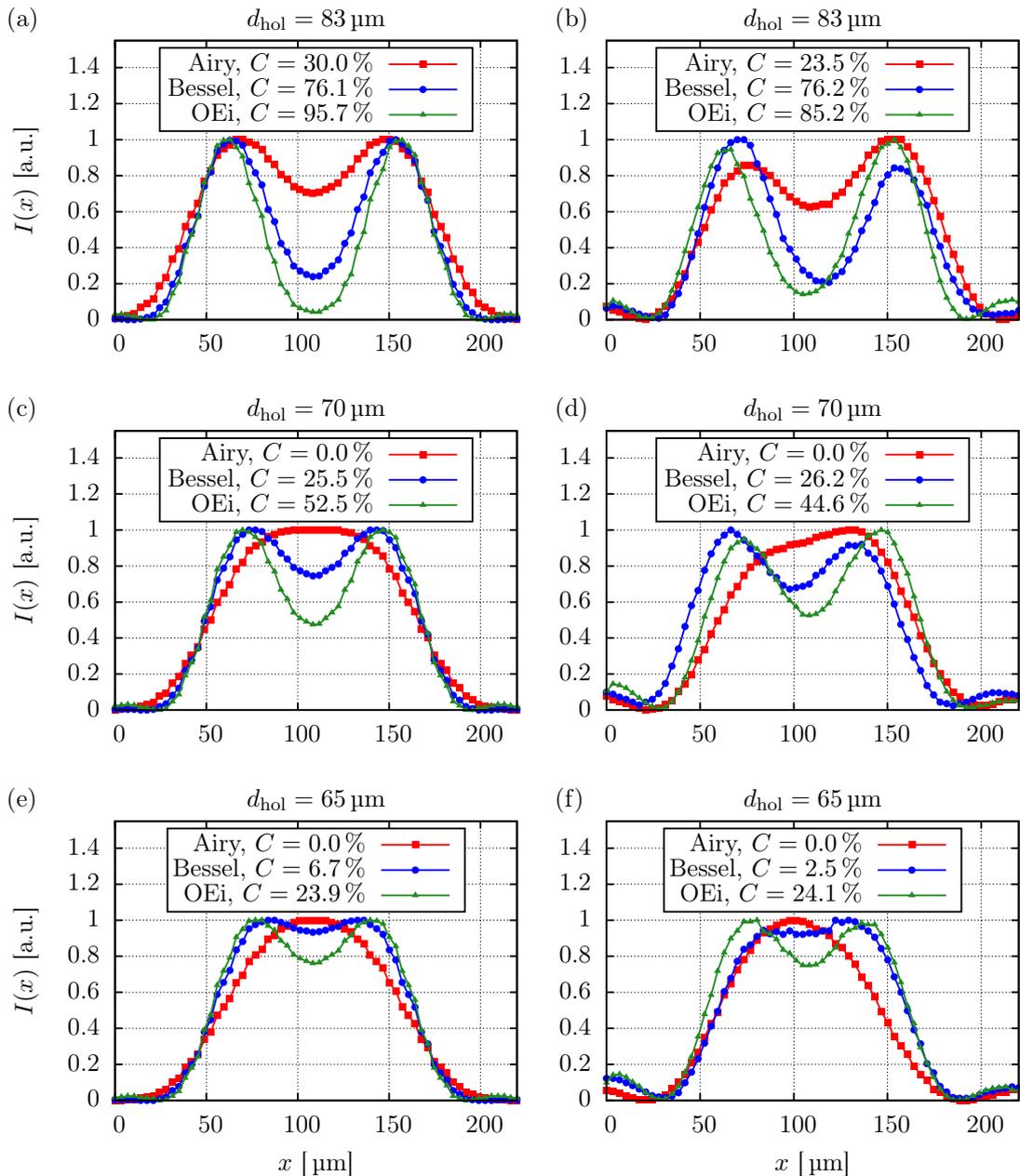
Figure 3.7: Profiles in x−direction through the centres of the (a,c,e) simulated and (b,d,f) experimentally obtained intensity distributions presented in Figure 3.6. Hole separations are (a,b) $d_{\mathrm{hol}} = 83\,\mu\mathrm{m}$, (c,d) $d_{\mathrm{hol}} = 70\,\mu\mathrm{m}$, and (e,f) $d_{\mathrm{hol}} = 65\,\mu\mathrm{m}$. The contrast C between the two peaks is indicated in each plot for scans with the Airy disk, a Bessel beam, and an OEi optimized spot.
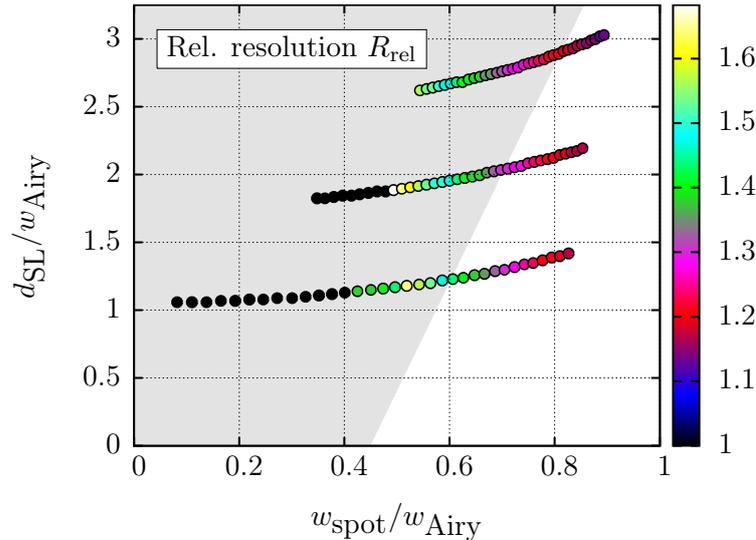
Figure 3.8: Simulated relative resolution for incoherent detection in dependence on the spot size w_{spot} and the distance d_{SL} between spot and sidelobes. The white background roughly indicates the area of the spots, which can reliably be produced experimentally (compare experimental data in Figure 3.4).

detection a Bessel beam delivers 1.19-fold enhanced resolution compared to the Airy disk, while using the OEi optimised spot improves resolution by a factor of 1.28. In comparison to the Bessel beam the OEi optimised spot still enables a 1.08-fold increased two point resolution capability. However, this is accompanied by increased artifacts around the holes, as can be seen in Figure 3.6. A little outlook for confocal scans with an incoherent detection process, such as fluorescence, is given in the summary in Section 3.6.

3.6 Summary

Summarising, the work presented in this chapter demonstrated the potential of the OEi method to tailor the focal field of an optical system. In analogy to prior work [116–119], the OEi approach was applied to the well known problem of determining pupil functions, which lead to a locally reduced focal width. The relationship of the spot size, the Strehl ratio, the sidelobe intensity and the distance between central peak and sidelobes was qualitatively following the behaviour described earlier [116–119]. The speedy calculation of optimised pupil designs by the OEi method in combination with the flexible implementation of the filters by means of an SLM system enabled an extensive experimental study to be carried out in order to determine the limitations of state-of-the-art beam shaping technique for the purpose of generating subdiffractive focal spots. With

the used setup and calibration methods, it was possible to experimentally reproduce spots with Strehl ratios down to 0.004 and a spot intensity of 0.7 relative to the intensity of the nearest sidelobe. The width of the spots could be squeezed to about 60 % of the Airy-disk's FWHM. Deviations from the simulations for Strehl ratios below 0.004 are due to residual aberrations in the system and inaccuracy in the pupil function implementation on the SLM, which could not be tackled by the calibration procedures. In a simple confocal imaging experiment with a coherent detection process, an OEi engineered focal spot helped to improve the resolution in the Rayleigh sense by a factor of 1.28 in comparison to scans with the Airy-disk. But as this resolution gain was accompanied by some artifacts, it will have to be investigated, how imaging of an extended object works. As a little outlook, Figure 3.8 depicts the simulated relative two point resolution R_{rel} for confocal imaging with an incoherent detection process, such as fluorescence. In that case using the same spot as for the experimental scans in Section 3.5 promises a resolution gain of about 1.45.

Based on these results, using pupil filters only offers a small resolution gain in comparison to microscopy techniques such as STED or PALM/STORM, which can increase the resolution up to an order of magnitude [89, 151]. Though pupil filters have the advantage of not relying on fluorescence techniques or special fluorophores, with structured illumination microscopy (SIM) there is already a technique available that offers a twofold resolution gain also for non-fluorescent samples [152]. It should be mentioned, that in Reference 153 at a wavelength of $\lambda = 640\,\mathrm{nm}$ a resolution of better than $\lambda/6$ has been reported using diffractive optical elements generating "superoscillations". But that is just due to a mismeasurement of the resolution. The resolution was determined by imaging a pair of 112 nm wide slits seperated by a gap of 137 nm. In particular it seems that the resolution was quantified as the FWHM of the central dip in the image of both slits. However, correctly measured it is the center to center distance of the two slits, i.e. the sum of slit width and slit gap. With the sample used in Reference 153, this corresponds to a Rayleigh resolution of about 250 nm, which can be achieved with conventional microscopes. Hence, the concept of pupil filters or "superoscillations" does not offer a great benefit in the field of imaging, as has also recently been pointed out in Reference 154. More practicable applications are areas which physically require a small focal spot, such as optical lithography and data storage [128, 129], optical transfection [155], and optical trapping. With respect to the latter it would be interesting to experimentally use the OEi method for maximising the force acting on a particle, as has been investigated theoretically in Reference 105. In the field of imaging, the OEi operator concept might be used not to minimise a focal spot, but to minimise the dark area of the depletion spot for RESOLFT microscopy.

Chapter 4

Optical Eigenmode imaging

At the example of minimising a focal spot, it was demonstrated in the previous Chapter 3, how the OEi approach an its operator concept can be used to extremise quadratic measures of the light field. In this chapter it is investigated, if the orthogonality of the eigenmodes themselves without any further operator based optimisation can contribute to minimise an important aspect in imaging: The number of probes required to obtain the image of an object. While in brightfield imaging the whole object is flooded with white light, spectroscopic imaging for example requires powerful coherent illumination of the sample, which is usually realised by a focussed laser beam scanning over the object. As the number of pixel in a raster scanned image equals the number of scanning positions, obtaining a high resolution image requires probing at many positions. This is particularly critical, if the acquisition time per pixel is long due to low efficiency of the light-sample interaction, as it is the case for Raman imaging. In the Raman regime, acquisition times of tens of seconds per image point may be required. Hence, obtaining an image with some thousands of pixels can take up to several days [156, 157].

A possible way to obtain high pixel resolution images with lower acquisition time are compressive indirect imaging methods, with "ghost imaging" probably representing the most popular variant. In brief, for these imaging modalities the whole sample is illuminated with different spatial light patterns and for each of the patterns a coefficient describing the interaction of the sample with the light is acquired. Superimposing the light patterns weighted with the measured coefficients gives rise to an image. The coefficients usually refer to a transmission or scattering by the sample. Detecting them wavelength dependent in principle also allows spectral imaging. Fluorescent ghost imaging has recently been proposed [158] and implemented with fluorophores of three colours in a compressive manner [45]. However, all these imaging methods still require a large number of probes and even the compressive modalities suffer from the fact, that their illumination patterns are not orthogonal on the sample, hence prohibiting the most efficient probing possible.

Here it is investigated, if the OEi as fundamental orthogonal basis set can be used to implement an indirect compressive imaging theme. In fact, using the OEi as illumination patterns should enable the most compressive imaging theme possible. In particular the goal is to apply "OEi imaging" in the field of spectroscopic imaging methods, which are powerful tools in biomedical research to characterise biological materials, such as cells and tissues [159]. Especially Raman spectroscopy has been proven to be very useful for the investigation of biologically relevant parameters. With particular emphasis on the discrimination between healthy and cancerous tissue, Raman spectroscopy promises reliable automated clinical tissue diagnosis, a task that to date is usually carried out by highly experienced pathologists [160–162]. The major drawback of Raman imaging, its long acquisition time, might be significantly diminished using optical eigenmode imaging. In this chapter, OEi as orthogonal illumination patterns are exploited for indirect imaging, first in transmission, then in fluorescence, and finally in the Raman regime. In the next Section 4.1 indirect imaging is introduced in more detail and the remainder of this chapter is outlined.

4.1 Compressive indirect imaging

"Ghost" [163], "interaction-free" [164], or "coincidence" [165] imaging are indirect imaging methods. The term "indirect" refers in this case to the fact, that an image is formed not directly by the light interacting with the object, but by a correlation between spatial light patterns and coefficients measured from the interaction of the object with these patterns. The first ghost imaging experiment by Pittman et al. in 1995 [166] utilised entangled photons generated by spontaneous parameteric down conversion [167]. The employed setup features two arms seperated by a beam splitter, a "test" arm and a reference arm. In the test arm one of the correlated photons impinges on the object under investigation and a single pixel detector positioned behind the object measures, whether or not the photon is transmitted. The reference arm features another single pixel detector, which can be spatially scanned to determine the position of the other part of the photon pair. An image can then be obtained from the coincidence measurements in conjunction with the position of the reference detector. Due to the fact that the image can not solely be formed from the individual detector signals, but only from their correlation, this modality was termed "ghost" imaging.

The demonstration of ghost imaging with a classical source by Bennink et al. in 2002 [165] triggered a lively debate on the necessity of entangled photons [168–170]. After numerous work on classical ghost imaging and its comparison to the original quantum mode [171–176] it seems to be commonly accepted, that all aspects of quantum ghost imaging can be achieved with classical light sources

as well, rendering it useable to a wider range of applications. Without the need for single photon counting, the whole object can at once be illuminated with spatially structured light patterns. These are usually generated by a rotating diffuser, covering the object with time dependent random speckle patterns. The spatial intensity distribution of the speckle is measured in the reference arm either by scanning a single pixel detector or, more conveniently, by a pixel array, such as a CCD sensor. For each of the speckle patterns the corresponding transmission or, also, reflection [177] coefficients are determined in the test arm. Correlating them with the measured speckle distributions gives then rise to an indirect image of the sample.

Recently, a form of ghost imaging was proposed [178] and implemented [179], that does not require a reference arm. In this so called "computational ghost imaging" the light is not shaped by a diffuser, but by an SLM. Encoding random phase masks on the SLM gives rise to random speckle patterns being projected onto the object. Knowing the encoded phase distributions enables numerical calculation of the resulting speckle patterns by means of diffraction theory. This makes an experimental measurement of the speckle distribution obsolete and allows to image the object just by correlating these numerical intensity maps with the corresponding measured transmission/reflection coefficients. Compared to the previous methods, this offers a very convenient and flexible implementation of indirect imaging.

An advantage of indirect imaging with full object illumination is that, as a "global random" acquisition scheme, it features a higher sampling efficiency compared to raster scanning methods [180]. This means that an image of the object can be obtained, whose pixel resolution exceeds the number of light patterns used for the acquisition. However, obtaining an indirect image with decent visibility of the sample is still a long process. This is why recently techniques for a more efficient object reconstruction have been explored [45, 181, 182]. In a combination of computational ghost imaging and compressive sensing, the aim is to represent the object in a sparse representation of the illuminating speckle patterns [181]. This is possible, if the object is compressible. In that case the coefficients of many of the speckle patterns are close to zero, as the speckle to not probe any features of the sample. Neglecting them improves the signal-to-noise (S/N) ratio, because then they do not contribute to the background of the image. Effectively this allows to reduce the number of acquisitions while still obtaining an image with good S/N level. A well known field utilising the approach of representing an image in a sparse basis set are image compression algorithms, as for example used with the JPEG file format [183]. Another method to improve the S/N ratio is differential ghost imaging, which only measures the fluctuations around the average transmission of the sample with respect to the set of speckle patterns. However, these methods do not work on the illumination itself, but just on the way the acquired data is treated. In contrast to that, another approach recently

realised is to project Hadamard patterns instead of speckle patterns onto the object [45]. Hadamard matrices are a set of orthogonal binary distributions. Hence they should enable a very efficient probing of the sample. However, the discontinuous transitions in the binary Hadamard patterns blur out due to diffraction, hence loosing their orthogonality. The work presented here goes a step further: The illumination of the object is shaped into its most sparse representation — Optical Eigenmodes. This is along the lines proposed in Reference 184 and similar to the realisation of compressive fluorescent imaging using Hadamard patterns in Reference 45. But in contrast to the experiments in Reference 45, the Optical Eigenmodes are truly orthogonal in the focal plane. It is this orthogonality combined with the fact, that the OEi are ordered according to their relevance, which potentially makes OEi imaging highly compressive.

To investigate this, the organisation of this chapter is as follows: In Section 4.2 the principle of OEi imaging is briefly outlined and its performance is compared to computational ghost imaging and raster scanning in simulations. With respect to the experimental realisation, the employed setups are described in Section 4.4. Furthermore, the practical reproducibility and orthogonality of simulated OEi is investigated and the experimental procedure to acquire an OEi image is detailed. Section 4.5 presents a macroscopic implementation of transmissive OEi imaging as well as the transition to spectral imaging in terms of flourescent OEi imaging. In Section 4.6 OEi imaging is implemented in the framework of Raman microscopy and used to image polystyrene and PMMA beads and to localise SERS hotspots. The chapter finishes with a summary and conlusions in Section 4.7.

4.2 Simulations: OEi imaging compared to ghost imaging and raster scanning

In this section the Optical Eigenmode Imaging, proposed and implemented in Reference 185, is compared in simulations to another indirect imaging method and to raster scanning imaging. The basic principle of OEi imaging is briefly introduced in Section 4.2.1. Section 4.2.2 compares the compressive nature of OEi imaging to an emerging indirect imaging modality, also using an SLM to generate illumination patterns: Computational Ghost Imaging. However, ghost imaging or variations of it have only recently been applied to spectral imaging [45, 186], for which to utilise OEi imaging is the goal of this work. Usually raster scanning is the preferred choice for fluorescence and Raman imaging. A relevant question in this context is the raster grid density required to achieve a certain spatial resolution and localisation accuracy of fluorophores or other relevant sample features, such as e. g. cell organelles. Hence, the resolution and localisation capabilities of OEi imaging are theoretically compared to raster scanning in Section 4.2.3.

4.2.1 Principle of OEi imaging

This section briefly outlines the basic principle of OEi imaging [185]. As a first step one has to determine M modes $\mathbb{F}_k$ in the sample plane. In theory[1], this is done as described in Section 2.5.1 and theoretical examples for a square sample area are depicted in Figure 2.9. In an indirect imaging fashion, these OEi are then projected onto the target $T(x_2, y_2)$. For each mode $\mathbb{F}_k$ a complex coupling coefficient c_k to the target is determined as

$$c_k = \iint\limits_{\text{ROI}} \mathbb{F}_k \, T \, d\sigma_2 \tag{4.1}$$

with $d\sigma_2 \equiv dx_2 \, dy_2$ and ROI being the area in which the OEi are defined. The superposition of the modes $\mathbb{F}_k$ with the corresponding coefficients c_k then delivers an image T^{img} of the target T:

$$T^{\text{img}} = \sum_{k=1}^{M} c_k \, \mathbb{F}_k. \tag{4.2}$$

4.2.2 OEi imaging and computational ghost imaging: Object reconstruction

The usual comparator for compressive indirect imaging methods is ghost imaging, probing the sample with random speckle patterns [173, 180, 181]. Hence the same is done in this section for the Optical Eigenmode Imaging. In particular, OEi imaging is compared in simulations to computational ghost imaging realised in Reference 179. Therefore a sample consisting of three transmissive holes, similar to the real sample used in Section 4.5, is represented as a binary distribution $T(x_2, y_2)$, depicted in Figure 4.1a. The sample size is $201 \, \text{pixel} \times 201 \, \text{pixel}$ and the holes have a diameter of $30 \, \text{pixel}$, which equals three times the diffraction limit of about $10 \, \text{pixel}$ for this simulation.

For the computational ghost imaging, M random phase distributions are generated in a plane reciprocal to the object plane. Upon numerical propagation according to Section 2.2.5, in the object plane these result in M random speckle patterns with two-dimensional intensity distributions $I_k(x_2, y_2)$, featuring speckles of diffraction limited FWHM. To obtain a ghost image, the transmission coefficient t_k is obtained for each speckle intensity distribution $I_k(x_2, y_2)$ by integration over the sample region ROI:

$$t_k = \iint\limits_{\text{ROI}} I_k \, T \, d\sigma_2 \tag{4.3}$$

[1] An experimental approach is illustrated in Sections 5.1.1 and 5.3.1
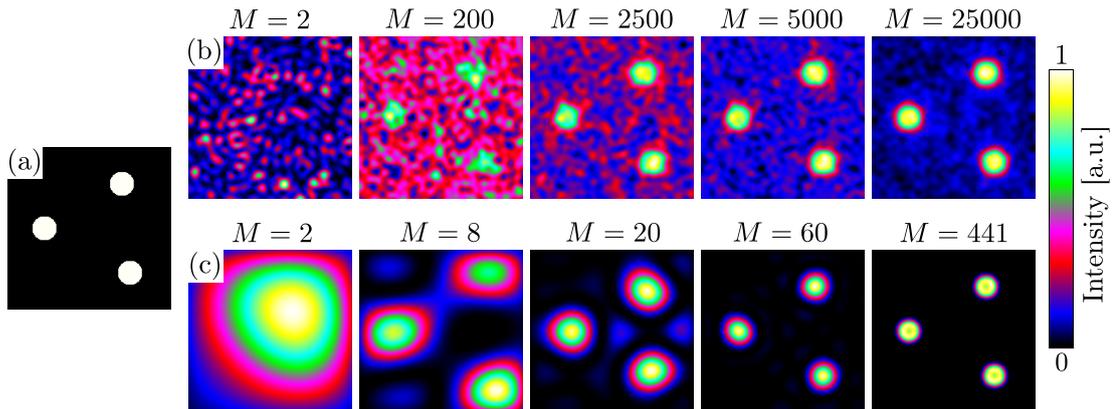
Figure 4.1: Comparison of computational ghost imaging and optical eigenmode imaging in simulations. (a) Simulated test target featuring three transmissive holes. (b) Simulated ghost images for increasing number M of projected speckle patterns. With increasing M the image of the three holes emerges from the noise. (c) Simulated optical eigenmode images for increasing number M of projected modes. With increasing M the sizes and positions of the imaged holes converge towards the actual positions and sizes.

with $d\sigma_2 \equiv dx_2\,dy_2$. The image T^{img} of the object is then composed by the superposition of the speckle patterns weighted with the transmission coefficients [181],

$$T^{\text{img}} = \frac{1}{M} \sum_{k=1}^{M} (t_k - \langle t \rangle)\, I_k, \tag{4.4}$$

where $\langle \cdot \rangle \equiv \frac{1}{M} \sum_{k=1}^{M} \cdot$ denotes the ensemble average. Figure 4.1b depicts ghost images for different numbers M of speckle pattern projections. For $M = 2$ one gets an idea of the speckle patterns themselves. At $M = 200$ the sample starts to emerge from the noise. For $M = 2500$ the object is clearly above the noise level, which is further decreased with increasing M. In Figure 4.2a the object reconstruction, quantified as deviation σ_{obj} according to

$$\sigma_{\text{obj}} = \frac{1}{N_{\text{pix}}} \sum_{p=1}^{N_{\text{pix}}} \left| T_p - T_p^{\text{img}} \right|, \tag{4.5}$$

is plotted depending on the number M of probes. For $M < 5000$ the deviation σ_{obj} decreases rapidly and is then decaying more slowly at $M > 5000$.

Figure 4.1c shows indirect images of the same object, simulated according to Section 4.2.1 by the projection of OEi instead of speckle patterns. For the superposition of $M = 2$ modes, intensity is spread over the whole area, but already for $M = 8$, three intensity spots give a rough idea of the object structure. With

(a)

(b)
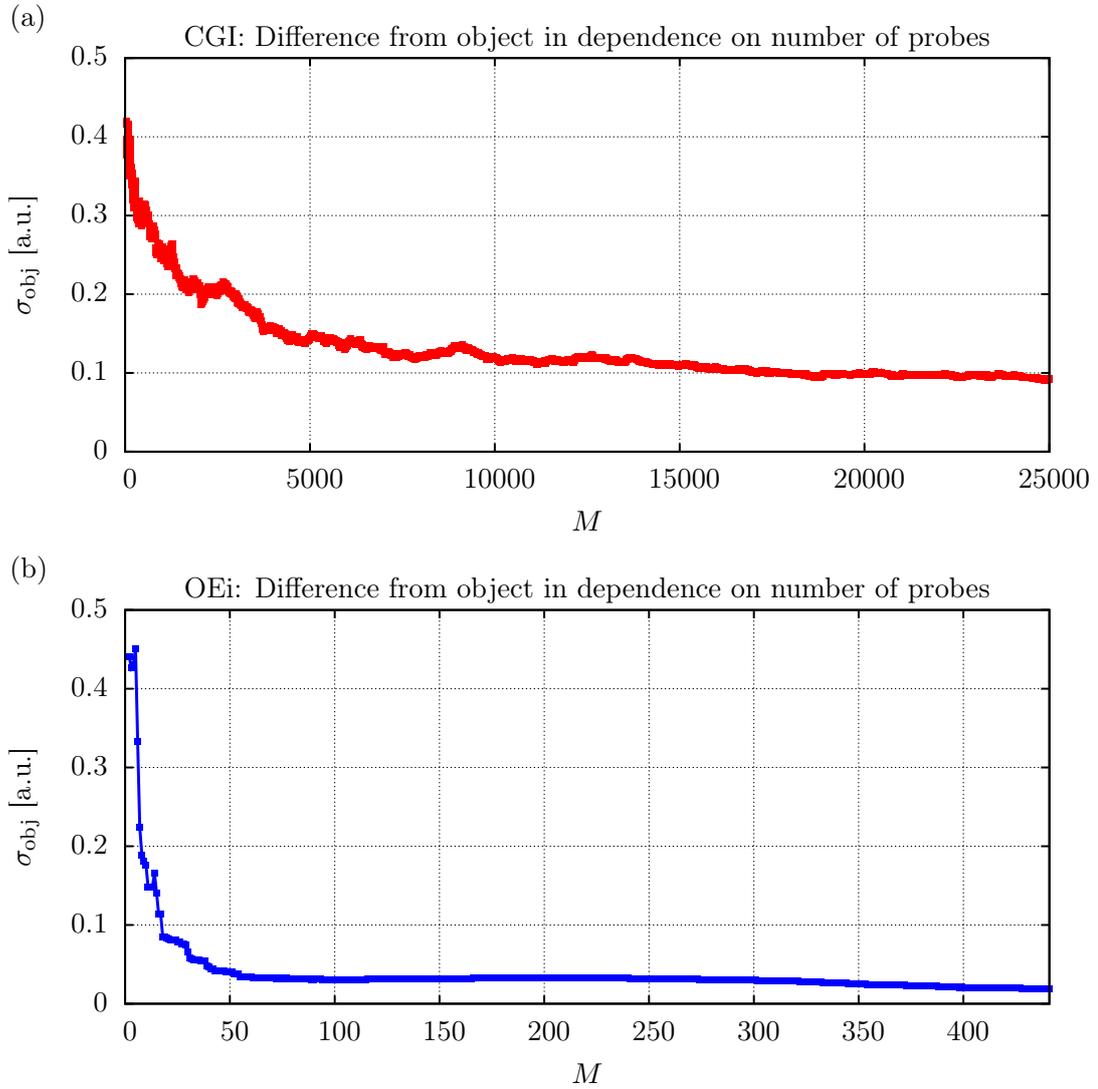
Figure 4.2: (a) Deviation σ_{obj} from object for computational ghost imaging depending on number M of projected speckle patterns. (b) Deviation σ_{obj} for optical eigenmode imaging depending on number M of projected modes (please note the different M scale on the horizontal axis). With eigenmode imaging the image converges quickly towards the actual object. The convergence in computational ghost imaging is much slower.

increasing M the sizes as well as the positions of these blobs get stronger confined to the actual arrangement of holes. The corresponding deviation σ_{obj} from the object, plotted in Figure 4.2b, decays much faster than for the traditional ghost imaging case. Actually, a constant level is already achieved for $M > 60$.

Comparing the reconstruction of the object with ghost imaging and OEi imaging on the basis of Figures 4.1 and 4.2 reveals some shuttle differences. For the OEi imaging the deviation σ_{obj} converges to a small remaining low level of discrepance between object and image. This can be attributed to diffraction, preventing replicating the discontinuities at the hole boundaries. The opaque areas of the sample also appear as such in the reconstruction. In contrast to that, for the ghost imaging the deviation is due to the same reason, but additionally also due to residual noise in the opaque areas of the sample, which is well visible in Figure 4.1b even for $M = 25000$ projections. A further difference is that in the ghost imaging case the holes "emerge" from the noise at their actual positions and with their actual size. Using OEi imaging, the reconstructed intensity distribution splits into three intensity blobs corresponding to the three holes. Then, using more higher order modes with finer features, these blobs converge towards the position and size of the holes.

Quantitatively, a deviation of $\sigma_{\mathrm{obj}} < 0.2$ is obtained for ghost imaging after about 2500 speckle pattern projections. OEi imaging requires just 10, i.e. 250 times less, projections. In order to push the reconstruction difference below 0.1 one needs roughly 17500 speckle patterns, while the same effect can be achieved with 20 OEi, corresponding to a factor of 875. Hence, using OEi imaging, one can lower the number of probes required to obtain the same object/image deviation by $2 - 3$ orders of magnitude. This is 1-2 orders of magnitude less than reported for other compressive indirect imaging modalities [181]. The most striking difference between OEi imaging and compressive computational ghost imaging is the low background of the OEi images. This is attributed to the phase information of the OEi: Destructive interference can cancel the background very efficiently.

4.2.3 OEi imaging and raster scanning: Localisation capabilities and PSF

In Section 4.2.2 it was observed, that in an OEi image the major change with increasing mode number is not the noise level, but the localisation accuracy and the size of object features, i.e. the resolution. Accurate reproduction of the object in terms of these quantities is an important ascpect of every imaging technique. A widely used imaging scheme for Raman imaging, which is the target application for OEi imaging in this work, is raster scanning. Here the localisation accuracy and resolution for a sampling above the Nyquist limit depends on the
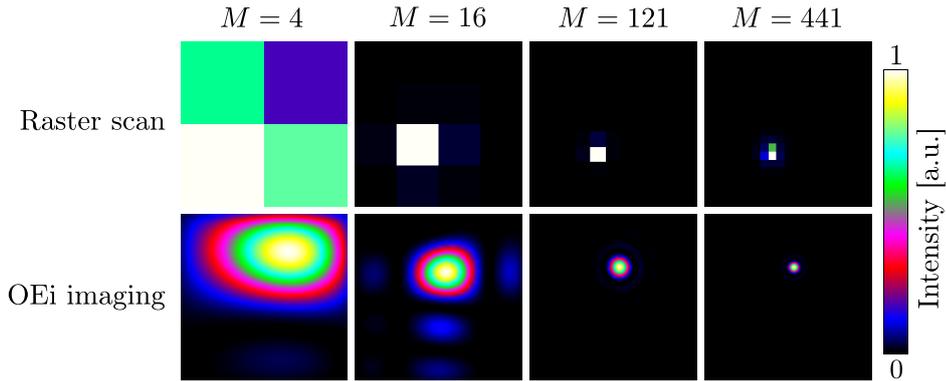
Figure 4.3: Raster scans and OEi images of a single point in the FOV for $M = 4$, 16, 121, and 441 probes.

raster density of the scan. For a sampling at the Nyquist rate, the resolution is ultimately bound by the diffraction limited width of the scanning spot. As the number of image points and hence also the acquisition time scales quadratically with the grid density, one wants to keep it as low as possible. The compressive nature of OEi imaging demonstrated in Section 4.2.2 promises that, using OEi compared to raster scanning, a lower number of probes might be required to obtain the same localisation accuracy and resolution. Investigating this proposal is the topic of this section.

Therefore binary objects of 201×201 pixels featuring one transmissive pixel are simulated. Then the imaging of these objects is simulated with raster scanning for varying number of raster points. In more detail, for each scanning point k the total transmission t_k of the target T is calculated upon illumination with the two-dimensional intensity distribution I_k of the diffraction limited Airy-disk:

$$t_k = \iint\limits_{\text{ROI}} I_k \, T \, d\sigma_2 \tag{4.6}$$

with $d\sigma_2 \equiv dx_2 \, dy_2$ and ROI indicating the rastered object area. An image is then composed from these transmissions. This imaging mode corresponds to raster scanning without confocal pinhole, hence the resolution limit is the conventional Abbe limit d_{Abbe} according to Equation 2.21 [94].

The top row in Figure 4.3 illustrates the PSF for raster scanning of a randomly chosen point for different numbers M of scanning coordinates. With increasing M the width of the PSF decreases, leading to a higher resolution and allowing a more accurate estimation of the position of the scanned point. For comparison, the bottom row of Figure 4.3 depicts OEi images of a randomly chosen point using the same numbers M of OEi (please note that the position of the points for both methods is not identical, but randomly chosen). At a first glance the OEi

(a)


(b)
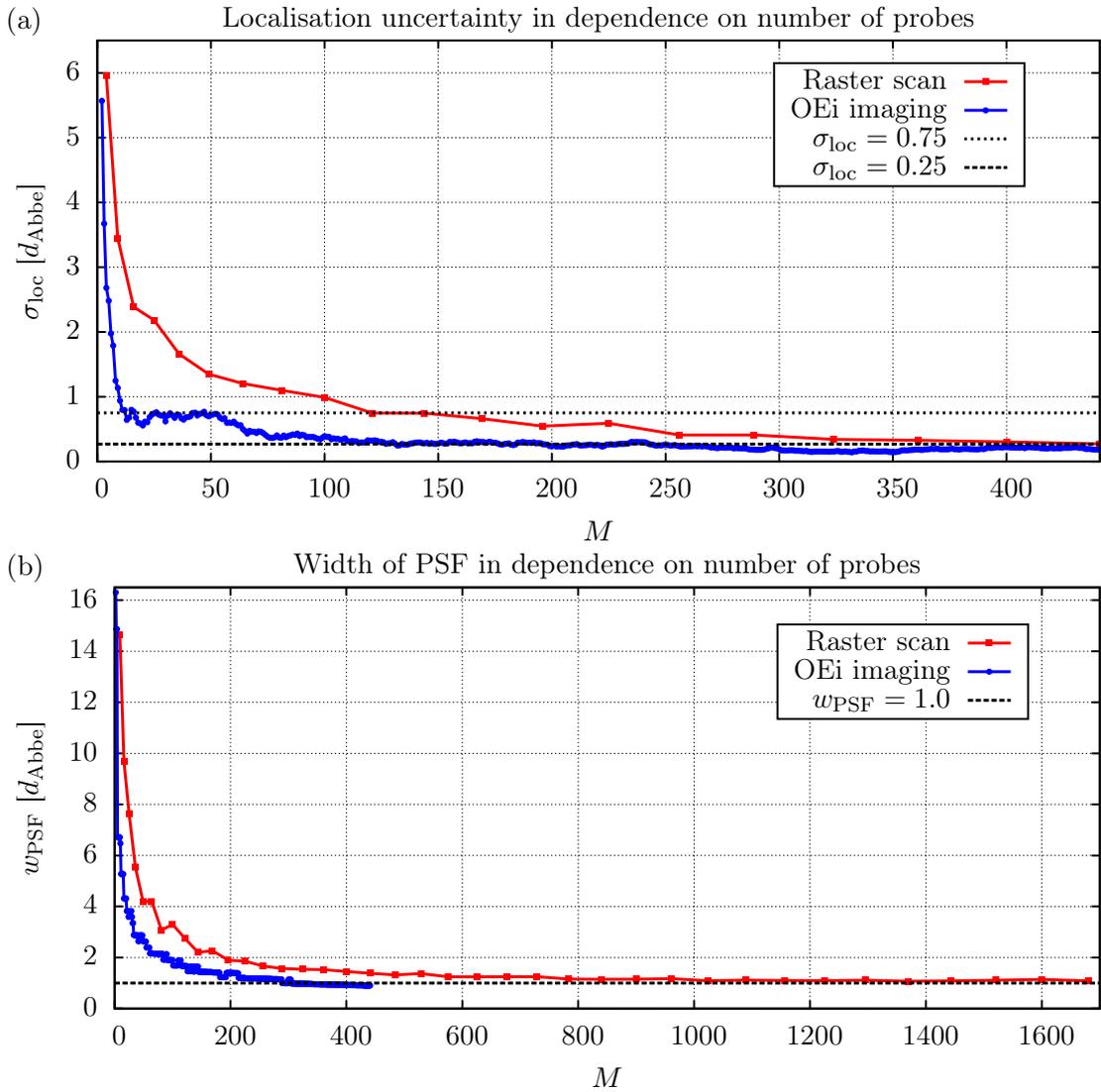
Figure 4.4: (a) Localisation accuracy σ_{loc} and (b) width w_{PSF} of the PSF, normalised to the Abbe limit d_{Abbe}, for raster scanning and OEi imaging depending on the number M of probes.

images appear more detailed, as each mode features the full pixel resolution of the simulated object. However, this does not yet say anything about the accuracy with which the point can be localised.

To quantify the localisation accuracy, the centroid of each image's intensity distribution is determined. The difference between the centroid and the actual coordinate of the transmissive pixel is a measure for the localisation precision and here referred to as σ_{loc}. In Figure 4.4a this difference σ_{loc} is plotted in dependence on the number M of probes, where probes are either scanning points or OEi. Each datapoint of the graph corresponds to the average over 10 randomly chosen pixel and σ_{loc} is normalised to the Abbe limit d_{Abbe}, which is about 10 pixel in these simulations. For the case of OEi imaging the localisation accuracy drops more rapidly then for raster scanning. With $\sigma_{\text{loc}} = 0.75$, a localisation error well below the diffraction limit is already obtained for 12 OEi, which requires raster scanning at 121 points. This is a factor 10 more illuminations. For larger numbers of illuminations, σ_{loc} changes more slowly. A level of $\sigma_{\text{loc}} = 0.25$ results from the projection of about 125 OEi and a point-by-point scan at 441 coordinates, corresponding to a factor of 3.5 in favour for OEi imaging.

Figure 4.4b depicts the width w_{PSF} of the PSF in dependence on the number M of probes. A raster scan at the Nyquist rate would require to scan with a grid spacing of half the diffraction limit. In the presented case this would mean 40 scanning points in each dimension, resulting in 1600 samples at all. Actually, in Figure 4.4b the width w_{PSF} for a raster scan already converges slowly within $M = 800$ samplings against the diffraction limit of $w_{\text{PSF}} = 1$. However, using OEi imaging, this a already the case for $M \approx 200$, corresponding to a factor four fewer probes.

In conclusion, OEi imaging is most beneficial in terms of localising object points for low numbers of acquisitions. Here the step width of the grid used for the raster scans is well above the diffraction limit and the OEi imaging benefits from its compressive properties in combination with the high pixel resolution of the modes. In that case an order of magnitude improvement is achieved compared to raster scanning the sample. With increasing number of scanning points the step width of the raster grid converges to the diffraction limit of about 10 pixel. Then the advantage of OEi imaging compared to raster scanning tails off and OEi imaging only save a factor 3.5 acquisitions compared to a point-by-point scan. A diffraction limited PSF is achieved with OEi imaging using a factor four less probes compared to raster scanning. However, for an objective comparison with a practical application in mind, it must be mentioned that OEi imaging also relies on phase information of the illumination, while a raster scan only uses intensity features. To experimentally reconstruct intensity and phase of the light field, at least three acquisitions are necessary [187], hence decreasing the advantage of OEi imaging for pure intensity objects. However, as has been discussed in
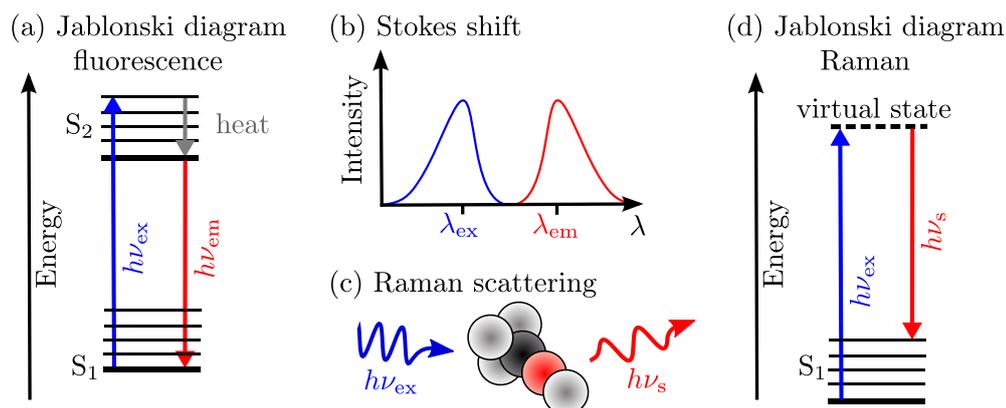
Figure 4.5: (a) Fluorescence excitation with energy $h\nu_{ex}$ and emission with energy $h\nu_{em}$ illustrated as Jablonski diagram. (b) Stokes shift between fluorescence excitation at wavelength λ_{ex} and emission at λ_{em}. (c) Schematic of Raman scattering with frequency ν_s after excitation with ν_{ex}. (d) Jablonski diagram for Raman scattering with virtual state.

Section 4.2.2, these phase information also enable a very low background and in principle also phase only objects could be imaged using OEi, as was shown in Reference 185.

4.3 Fluorescence, Raman scattering, and SERS

This section gives a brief introduction into the effects of fluorescence, Raman scattering, and surface enhanced Raman scattering (SERS). All three modalities are utilised for imaging in the remainder of this chapter.

Fluorescence belongs to the family of luminescence processes [188]. In these, light of an excitation frequency ν_{ex} is absorbed by the molecules of a substance, leaving them in an electronically excited state S_2. After the life time of that state, the molecule returns to its ground state S_1 under emission of light of frequency ν_{em}. This process is visualized in Figure 4.5a as a so called *Jablonski diagram*. Within luminescence, one distinguishes between fluorescence and phosphorescence. The difference between both processes is in their life time. Fluorescence usually features life times in the nanosecond range, while the life time of phosphorescence can be on the scale of milliseconds to minutes. Most of the time a part of the excitation energy $h\nu_{ex}$ is thermally lost, so that the reemitted light is shifted to longer wavelength by the *Stokes shift* [189], illustrated in Figure 4.5b. Usually the emission wavelength of fluorescence does not depend on the excitation wavelength. Fluorescent molecules often feature aromatic rings and are an important tool in biology. In combination with antibodies, they can be used to selectively

stain e.g. a cell's nucleus, membrane, or cytoskeleton for studies in fluorescence microscopy [190].

Another way light can interact with matter different from absorption/emission is scattering. For elastic scattering, the photon incident on a molecule just changes its direction, but not the momentum, i.e. wavelength/frequency. This is referred to as *Rayleigh scattering* [191]. In contrast, the Raman effect [192] is an inelastic scattering process, as illustrated schematically in Figure 4.5c and as Jablonski diagram in Figure 4.5d. A photon of energy $h\nu_{ex}$ excites vibrational states in a molecule [193]. The wavelength λ_s of the scattered photon with energy $h\nu_s$ is stokes shifted with respect to the excitation wavelength λ_{ex}. The Raman shift, calculated by

$$\text{Raman shift} = \frac{1}{\lambda_{ex}} - \frac{1}{\lambda_s}, \tag{4.7}$$

is related to the energy of the excited state. Measuring it enables material specific information without any need for labeling, which is a major advantage over fluorescent techniques. A disadvantage of Raman spectroscopy is its low scattering cross section, which is usually about 15 orders of magnitude lower then the cross section of fluorescence [193].

An option to increase that cross section is surface enhanced Raman scattering (SERS) [194]. The term "SERS" relates to the enhanced Raman signal observed for molecules close to or on the surface of metallic structures. This is attributed to two effects. On the one hand, upon illumination with laser light nanometric metallic structures give rise to a plasmonic enhancement of the electromagnetic field close to the structure. Popular structures are nanoantennas [77, 195] or simply nanoparticles [196]. On the other hand it has also been observed that binding of certain molecules to rough metallic surfaces leads to an increased Raman signal. This might be explained by an alterration of the electronic states of the molecules due to the binding [197]. In the best case, SERS offers cross sections similar to the ones of fluorescence [194], which enables detection of single molecules [198].

4.4 Experimental OEi imaging

Following the simulations in Section 4.2, this section deals with the experimental implementation of OEi imaging. The experimental setups for OEi imaging on the macroscopic and the microscopic scale are described in Section 4.4.1. In Section 4.4.2 the experimental reproducibility of theoretically calculated OEi, in particular their orthogonality, is investigated. Finally, the experimental OEi imaging process is outlined in Section 4.4.3.

4.4.1 Setups

This section describes the experimental systems for macroscopic OEi imaging in transmission and with fluorescence in Section 4.4.1.1 and for OEi Raman microscopy in Section 4.4.1.2.

4.4.1.1 Setup for bulk OEi imaging

The optical arrangement for macroscopic OEi imaging is depicted in Figure 4.6. The beam of a 1 W Ti:Sapphire laser (3900S, Spectra-Physics, wavelength $\lambda = 785$ nm) pumped with a frequency doubled 6 W Nd:YAG laser (Verdi V-6, Coherent Inc.) is collimated and reflected of the display of an SLM (LCOS-SLM X10468-02, Hamamatsu Photonics). The first order modulated light is filtered out by an iris (I) positioned in the focal plane of a telecope and then focused onto the sample. A small fraction of the focused light is reflected by a dichroic beam splitter (DBS) onto a CCD camera (Basler pilot piA640-210gm, 648 pixel × 488 pixel resolution, 7.4 μm pixel pitch). This enables the visualisation of the light pattern which illuminates the object. The laser light transmitted by the sample is focused by a telecope onto a single pixel photo detector (PD). Stokes shifted flourescent light emitted by the sample is reflected from a 45° notch filter (NF) and, after passing a second NF, focused onto the entrance slit of a spectrograph (Shamrock SR-303i-B, Andor). The spectra are acquired with a 400 lines/mm grating blazed for 850 nm on a cooled CCD detector (Newton CCD, Andor).

4.4.1.2 Setup for OEi Raman microscopy

The experimental setup for OEi Raman microscopy is depicted in Figure 4.7. Up to the iris (I) it is identical to the one described in Section 4.4.1.1, except for that the laser source, which in this case is a linearly polarized diode laser (TEC-420-0780-1000, Laser 2000) with 785 nm emission wavelength. The first order modulated light from the SLM passing the iris is coupled into a microscope objective MO (100×/1.30 Oil UPlanFL N, Olympus) and focused onto the sample (S). Raman scattered light from the sample is collected in epi-configuration, transmitted through a 45° notch filter (NF) as well as a plane NF, and focused onto the entrance slit of the spectrograph. The latter is identical to the one in Section 4.4.1.1 (Shamrock SR-303i-B, Andor) and acquires spectra with a 400 lines/mm grating blazed for 850 nm on a cooled CCD detector (Newton CCD, Andor). Laser light reflected from the sample is reflected by the 45° NF and another dichroic beam splitter DBS onto the same CCD camera as in Section 4.4.1.1. For a transmissive sample, whitelight illumination can be provided by a light emitting diode (LED).
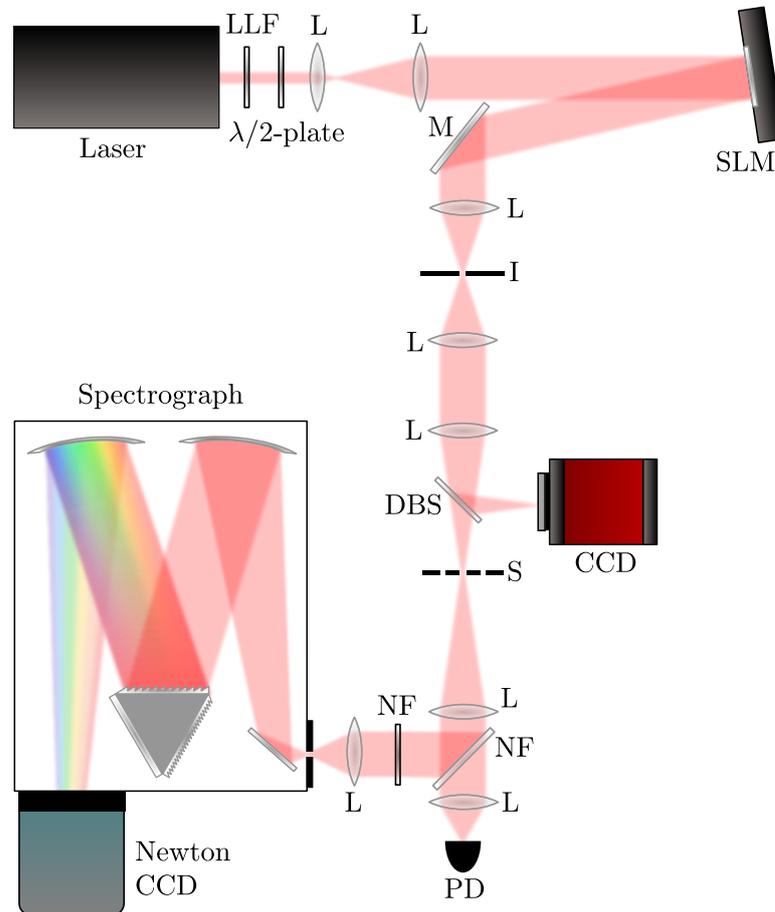
Figure 4.6: Experimental setup for optical eigenmode imaging. LLF: Laser line filter at 785 nm; L: Lens; SLM: Spatial light modulator; M: Mirror; I: Iris to filter out first diffraction order from SLM; DBS: Dichroic beam splitter reflecting visible light and transmitting infrared light; CCD: CCD camera; S: Sample; NF: Notch filters to transmit light with wavelengths longer then 785 nm into the spectrograph; PD: Photo diode.
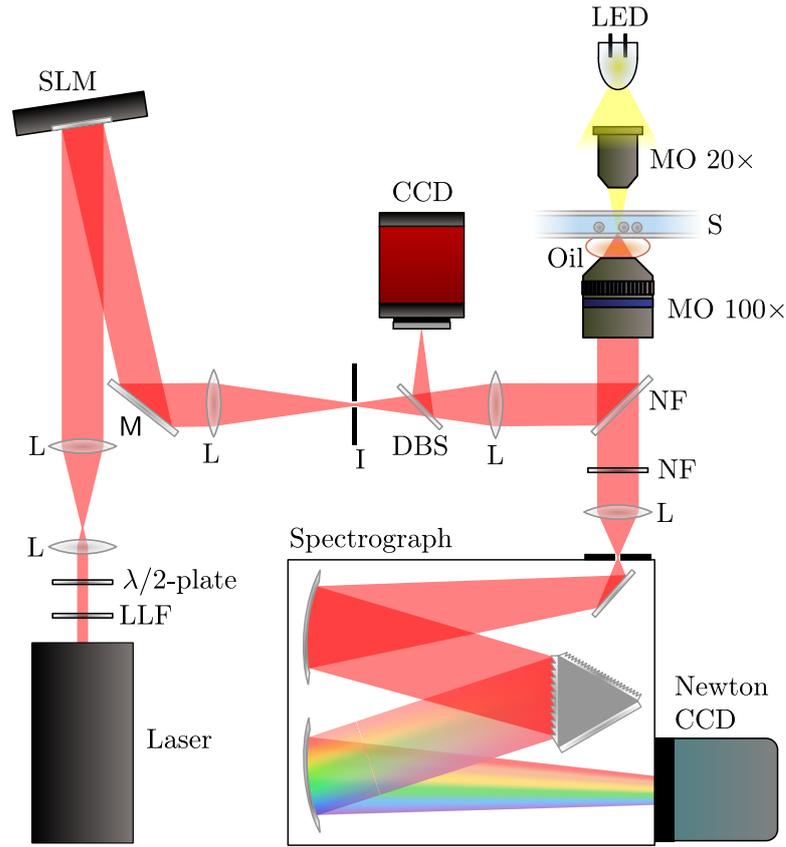
Figure 4.7: Experimental setup for optical eigenmode Raman microscopy. LLF: Laser line filter at 785 nm; L: Lens; SLM: Spatial light modulator; M: Mirror; I: Iris to filter out first diffraction order from SLM; DBS: Dichroic beam splitter reflecting visible light and transmitting infrared light; CCD: CCD camera; NF: Notch filters to transmit light with wavelengths longer then 785 nm into the spectrograph; MO: Microscope objective; S: Sample.

In order to get a comparator for the OEi Raman images, a Raman raster scan can be performed with this setup by deflecting the focus over the sample using the SLM as scanning mirror. More detail on this can be found in Section 3.5.1.1. An image is then composed from the spectra acquired at each beam position. For this to work, the input slit of the spectrograph has to be opened wide enough to let the light at each scanning coordinate pass. Like that the imaging process loses its confocality, which, compared to an infinitesimal slit, will degrade the lateral resolution by a factor of 1.4 [94], if the step width of the scans is similar to the width of the scanning beam. On the other hand, the same opening width has to be used for OEi imaging, as the whole illuminated ROI has to pass through the slit. For the experiments carried out, the slit width was 300 μm.

4.4.2 Experimental OEi

Figure 2.9 in Section 2.5.2 depicts simulated OEi in the focal plane of the microscope objective used in the setup of Section 4.4.1.2. In this section it is investigated if these modes can be replicated experimentally and if they are orthogonal in the focal plane. Therefore a microscope slide was coated with a $100\,\mathrm{nm}$ layer of silver, acting as mirror in the focal plane onto which the laser light is focused through that slide. This generates conditions similar to a real sample on a microscope slide and enables easy cleaning of the immersion oil after usage. To visually inspect the OEi in the focal plane, the reciprocal fields depicted in Figure 2.8, Section 2.5.2, are encoded on the SLM of the setup described in Section 4.4.1.2. Then the resulting focal fields are captured on the CCD camera with the coated microscope slide positioned in the focal plane of the objective. The resulting intensity distributions are depicted in Figure 4.8 and show good agreement with their simulated counterparts in Figure 2.9. However, this does not prove orthogonality of the modes, for which the accurate reproduction of phase properties is essential.

Orthogonality of two spatial fields $\mathbb{F}_k$ and $\mathbb{F}_l$ means, that the integral of the cross product $\mathbb{F}_k\,\mathbb{F}_l^*$ vanishs in the region ROI of orthogonality if $k \neq l$, and is unity for the field multiplied with itself:

$$\int\limits_{\mathrm{ROI}} \mathbb{F}_k\,\mathbb{F}_l^*\,d\sigma_2 = \delta_{kl} \tag{4.8}$$

with $d\sigma_2 \equiv dx_2\,dy_2$. The image denoted as "Theory" in Figure 4.9 depicts this relationship for the simulated OEi. The row and column numbers of the displayed matrix correspond to the indices k and l respectively. With the diagonal elements being unity and the offdiagonal elements equaling zero, in theory the OEi are perfectly orthogonal. Experimentally, the product $\mathbb{F}_k\,\mathbb{F}_l^*$ can be obtained via the "polarisation identity" [199]

$$\mathbb{F}_k\,\mathbb{F}_l^* = \frac{1}{4}\sum_{p=0}^{3} \mathrm{e}^{\mathrm{i}\frac{\pi}{2}p}\left|\mathbb{F}_k + \mathrm{e}^{-\mathrm{i}\frac{\pi}{2}p}\,\mathbb{F}_l\right|^2. \tag{4.9}$$

The absolute square in Equation 4.9 is captured on the CCD with the field $\mathbb{E}_k + \mathrm{e}^{-\mathrm{i}\frac{\pi}{2}p}\,\mathbb{E}_l$ encoded on the SLM. The image denoted "Experiment" in Figure 4.9 depicts the experimentally resulting orthogonality relationship (4.8) for the first 9 OEi. Visually, theory and experiment are in good agreement. Quantitatively the orthogonality can be characterised by the quotient σ_{orth} of the average offdiagonal entries and the average diagonal entries of the orthogonality matrix O:

$$\sigma_{\mathrm{orth}} = \frac{\overline{\mathrm{offdiag}(O)}}{\overline{\mathrm{diag}(O)}}. \tag{4.10}$$
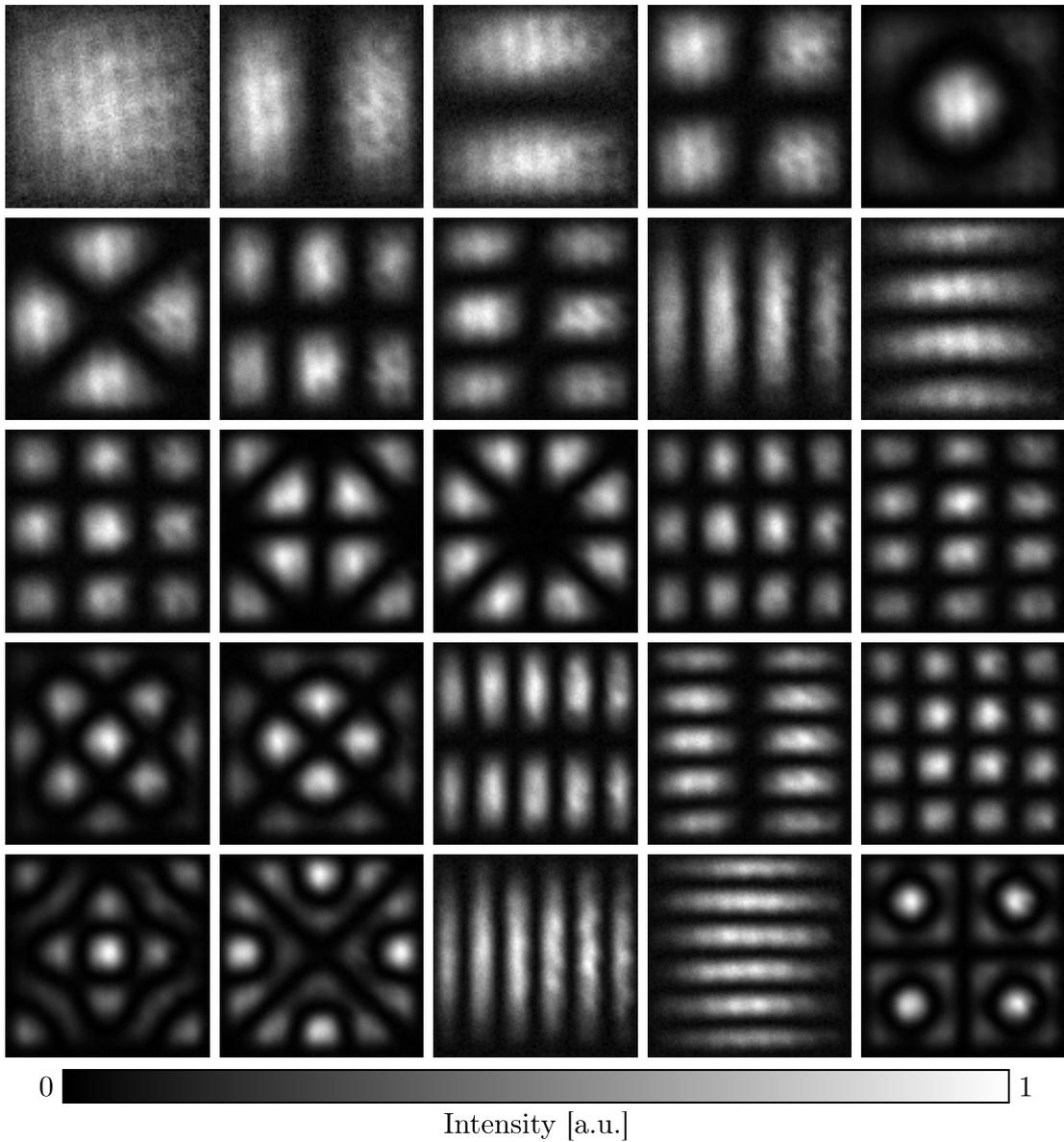
Figure 4.8: Experimentally captured spatial intensity distributions of the first 25 optical eigenmodes, corresponding to the simulations in Figure 2.9. The images were obtained with the CCD camera in the setup in Figure 4.7 with a mirror in the focal plane of the 100× microscope objective and the fields in Figure 2.8 encoded on the SLM.
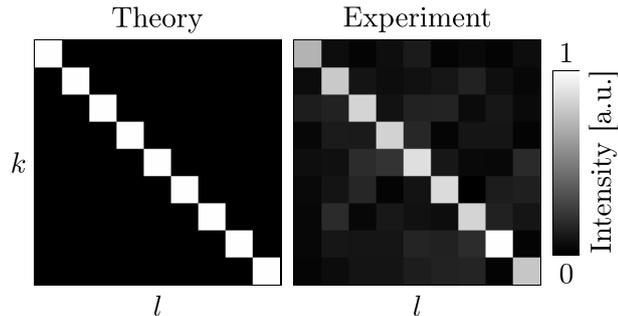
Figure 4.9: Theoretical and experimental orthogonality matrix for the first 9 optical eigenmodes. The latter was obtained with a mirror positioned in the focal plane of the 100× microscope objective in the setup in Figure 4.7.

The normalisation can be measured as the standard deviation σ_{diag} of the diagonal elements. For the experimental data shown in Figure 4.9 the corresponding values are $\sigma_{\text{orth}} = 0.09$ and $\sigma_{\text{diag}} = 0.08$. Hence, with less than $10\,\%$ error it can be concluded that orthogonality of the OEi in the focal plane is fulfilled to a good approximation. Deviations between the experimental and the theoretical orthogonality matrix will be due to a combination of measurement uncertainty and nonperfect encoding of the amplitude and phase of the fields $\mathbb{E}_k$ on the SLM.

4.4.3 Experimental procedure of OEi imaging

Following the description of the basic OEi imaging principle in Section 4.2.1, this part deals with its practical implementation. In the course of this, the major challenge is to determine the complex coefficients c_k in Equation 4.1, which characterise the coupling of each mode $\mathbb{F}_k$ to the sample. With a single acquisition, the detectors used in the setups described in Section 4.4.1 only provide intensity information. For access to the complex coupling coefficients, phase retrievial methods are required. In principle not more then three intensity acquisitions are necessary for phase reconstruction [187]. However, depending on the noise level, more measurements might improve the phase reconstruction accuracy. Hence the polarisation identity described in Section 4.4.2 is employed here. In particular, each mode $\mathbb{F}_k$ is interfered with a reference wave E_{ref} for P different phase shifts of the latter. This enables the reconstruction of the complex coefficient c_k for each OEi with respect to the complex coupling c_{ref} of the reference wave:

$$c_k\, c_{\text{ref}}^* = \frac{1}{P} \sum_{p=0}^{P-1} \mathrm{e}^{\mathrm{i}\frac{\pi}{2}p} \iint\limits_{\text{ROI}} \left| \mathbb{F}_k + \mathrm{e}^{-\mathrm{i}\frac{\pi}{2}p}\, F_{\text{ref}} \right|^2 d\sigma_2 \qquad (4.11)$$

with $d\sigma_2 \equiv dx_2\, dy_2$. The integration over the imaged area ROI is effectively carried out by the single pixel detector, onto which the illuminated object is imaged.
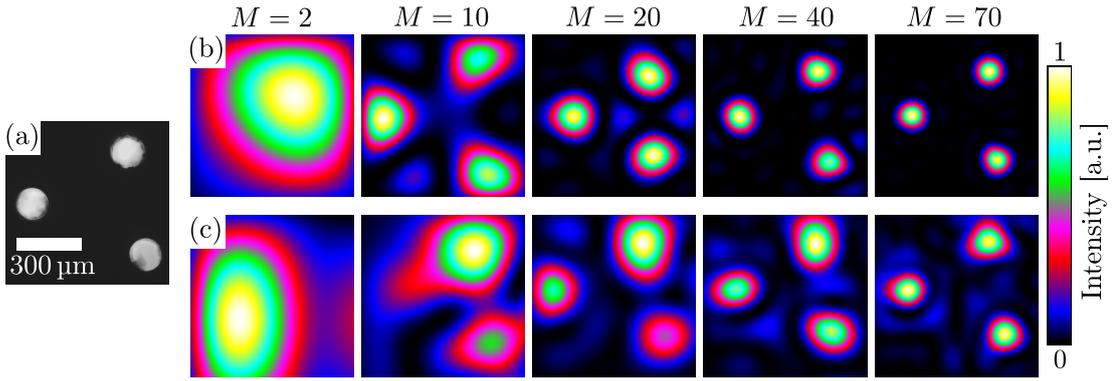
Figure 4.10: Optical eigenmode imaging in transmission. (a) Transmission image of the sample taken with a conventional microscope. (b) Simulated optical eigenmode images of the sample for different numbers M of projected modes. (c) Experimentally obtained optical eigenmode images corresponding to the simulations in (b).

The fact that the complex coupling is only determined with respect to the coupling coefficient of the reference wave is not problematic as long as each coefficient c_k is measured with the same reference. Equation 4.11 already enables the full complex reconstruction of the c_k. However, it was observed that the reconstructed amplitude $|c_k|$ can be retrieved with less noise as the squareroot of a single acquisition with only the mode $\mathbb{F}_k$ illuminating the sample. Hence, amplitude and phase of the the complex coefficient c_k are determined seperately, where the phase is obtained by taking the complex angle of Equation 4.11. With knowledge of the c_k, an image of the object is then obtained according to Equation 4.2 with the modes $\mathbb{F}_k$, which are known from simulations and have in Section 4.4.2 been demonstrated to be accurately reproduced experimentally.

4.5 Macroscopic OEi imaging

As a first step towards OEi Raman microscopy, this section provides proof of principle experiments of OEi imaging both in transmission and with fluorescence. In Section 4.5.1 a test target consisting of three holes in an aluminium plate, which was already simulated in Section 4.2.2, is imaged using the OEi concept. For a simple spectral imaging experiment, in Section 4.5.2 one of the holes is covered with a thin film of Blu-Tack, which is essentially a polymer and exhibits some fluorescence.

4.5.1 OEi imaging in transmission

For the first OEi imaging experiment an aluminium plate featuring three holes of $150\,\mu m$ diameter is positioned in the sample plane of the setup described in
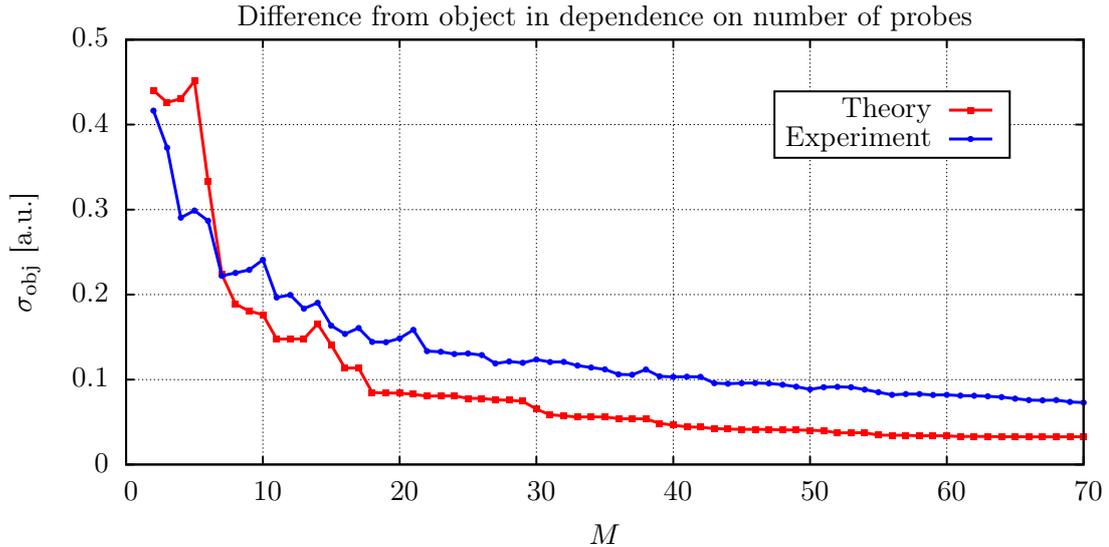
Figure 4.11: Difference σ_{obj} between object and eigenmode image according to Equation 4.5 depending on the number M of projected modes. Red curve: Simulation; Blue curve: Experiment.

Section 4.4.1.1. A transmission image of the sample captured with a conventional microscope (Nikon ECLIPSE Ti-S) is depicted in Figure 4.10a. An OEi image of the object is obtained as described in Section 4.4.3, using the photo detector of the setup in Section 4.4.1.1 to determine the coupling coefficients c_k. Figure 4.10c shows the reconstruction of the three holes for different numbers M of OEi. For $M = 2$, the features of the sample are not revealed. Using $M = 10$ modes, two of the three holes start to be reconstructed. With $M = 20$ probes, the third hole is becoming visible in the reconstruction. When imaging with $M = 40$ and $M = 70$ OEi, the positions and sizes of the holes are narrower confined to the actual arrangement. For comparison, Figure 4.10b depicts the corresponding simulated results from Section 4.2.2. In the experiment slightly more OEi are required to reconstruct the sample in good approximation and the final simulated result also shows better agreement with the object compared to the experiment. But overall simulation and experiment are in reasonable agreement.

Quantitatively, this observations are illustrated in Figure 4.11, which depicts a plot of the difference σ_{obj} between object and reconstruction in dependence on the number M of modes used for the imaging process. The deviation σ_{obj} was quantified according to Equation 4.5. The simulated curve in red and the blue experimental curve exhibit very similar behaviour in the decay of σ_{obj} with increasing number M of modes. For small $M < 20$, σ_{obj} drops quickly and is decreasing less rapid from about $M \geq 20$. In almost the full range of $2 \leq M \leq 70$, the theoretical deviation ranges below the experimental data. This is to be expected: The simulated image is in better agreement with the object as the experimental
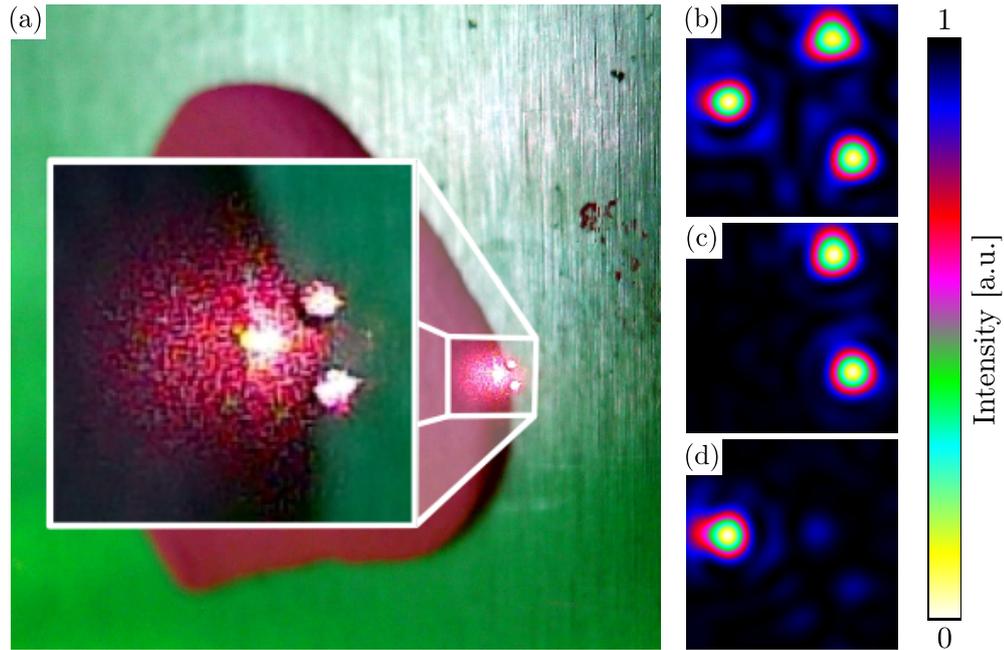
Figure 4.12: Experimental eigenmode imaging using fluorescence: (a) Macro photograph of the three hole test target with one hole being covered by pink Blu-Tack. The sample is illuminated from the other side by the reference wave. (b) Eigenmode image for $M = 70$ modes reconstructed based on the photodiode signal without Blu-Tack. (c) Eigenmode image on the basis of the photodiode signal, but one hole covered with Blu-Tack. Only the two free holes are reconstructed. (d) Eigenmode image reconstructed using the fluorescence signal captured with the spectrograph. Now the hole which is covered by Blu-Tack is reconstructed.

image. In conclusion, the results in this section show that the experimental performance of OEi imaging agrees to what has been proposed in the simulations, meaning that also experimentally a simple object can be reconstructed in good approximation from about 20 modes. After this first working example, OEi imaging is taken to the range of fluorescence in the next Section 4.5.2, for which the signal is weaker than for imaging in transmission.

4.5.2 OEi fluorescence imaging

On the route to OEi Raman microscopy, this section deals with the intermediate step of fluorescence imaging. Therefore one of the holes in the test sample from the previous Section 4.5.1 is covered with a thin layer of pink Blu-Tack. This scenario is visualised in Figure 4.12a by means of a photograph of the sample. The Blu-Tack blocks most of the laser light, but instead exhibits fluorescence at wavelengths larger then the 785 nm excitation wavelength. This fluorescence
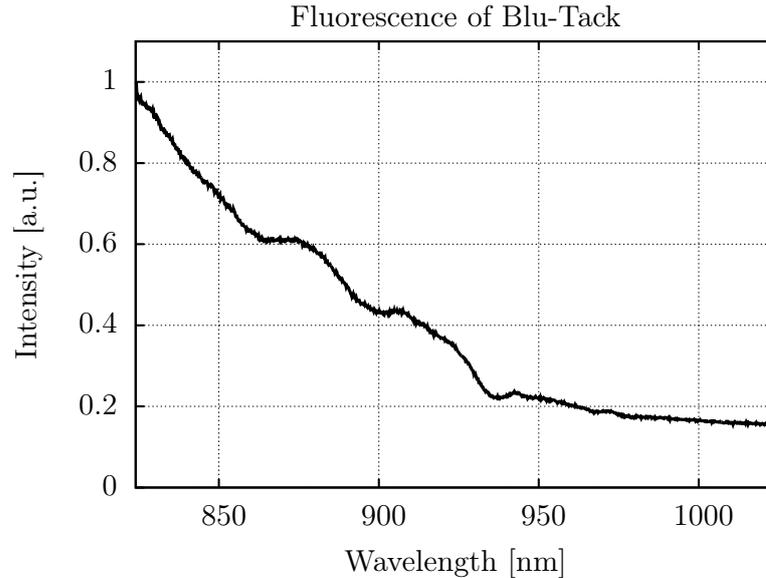
Figure 4.13: Fluorescence spectrum of Blu-Tack: Normalised counts in dependence on the wavelength.

can be detected via the spectrograph in the setup of Section 4.4.1.1. The two notch filters in front of the entrance slit should make sure that almost no laser light, but only frequency shifted fluorescence and Raman scattered light enters the spectrometer. However, to gain certainty that the signal detected with the spectrograph is not part of the tail of the laser light, it was compared with and without Blu-Tack in front of the holes. With Blu-Tack the signal detected with the spectrograph is much stronger and less noisy, hence confirming that it is indeed broad fluorescence of the Blu-Tack. Figure 4.13 depicts the broad fluorescence spectrum captured with the spectrograph.

The imaging experiment is then performed identically to Section 4.5.1. The only difference is that the coupling coefficients c_k are determined for both detectors, the photo diode and the spectrograph. Then an image is reconstructed based on the coefficients for each detector. For comparison to these, the image of all three holes from Section 4.5.1 is shown in Figure 4.12b. Figure 4.12c depicts the image resulting from the photo diode signal with one hole blocked by Blu-Tack. The two not covered holes are reconstructed based on the transmitted laser light, while the blocked hole remains dark. The opposite is the case when reconstructing based on the fluorescence detected with the spectrograph, as shown in Figure 4.12d. Here the covered hole is reconstructed while the two transmissive holes are at most visible as dark shadows. The latter will be due to some residual laser light which is not filtered out by the notch filters.

In conclusion, the results presented in this section show the capability of OEi imaging to reconstruct fluorescent samples. This is an important step towards

OEi Raman microscopy, in which the signal will be much weaker then fluorescence.

4.6 OEi Raman microscopy

In this section the concept of OEi imaging is extended to the regime of Raman spectroscopy. As the Raman scattering effect in general has a very low cross section, the first imaging experiment in Section 4.6.1 uses polystyrene and PMMA beads, which feature a relatively strong and distinct raman spectrum. In Section 4.6.2 advantage is taken of the SERS effect and OEi imaging is utilised to localise SERS hotspots.

4.6.1 Raman imaging of polystyrene and PMMA beads

The first OEi Raman imaging experiment uses polystyrene beads of 3 µm diameter (Microbead NIST Traceable, Polysciences Europe GmbH). For sample preperation, a sticker of about 100 µm thickness featuring a 1.25 cm aperture is glued onto a 25 mm × 25 mm quartz glass slide (CFQ-2557, UQG Optics) of 0.17 mm thickness. Then 30 µL of the solution containing the beads is distributed in the aperture and left to dry. That causes the beads to stick to the quartz slide, so that they do not drift around during the acquisition process. Then the sample volume is carefully refilled with 30 µL of water such that the beads do not detach from the surface. After closing the sample chamber by putting a coverglass on top, it is sealed with clear nail polish to prevent evaporation of the water.

For the imaging process the sample is placed in the focal plane of the setup described in Section 4.4.1.2. Then the acquisition process is performed according to Section 4.4.3, illuminating a sample area of about 6 µm × 6 µm with optical eigenmodes. For each mode $\mathbb{F}_k$ a complex coupling coefficient c_k has to be obtained. In the case of Raman imaging presented here, this coefficient is determined with respect to a certain range within the Raman spectrum, featuring the characteristics of the spectrum for the sample's material. The Raman signal of polystyrene exhibits a strong peak at a Raman shift of about $1001 \, \text{cm}^{-1}$ [200]. In Figure 4.14a it is indicated in red in the Spectrum resulting from illumination of a polystyrene bead with a focused beam. In more detail the determination of each coupling coefficient c_k works as follows: To determine the amplitude of c_k, the sample is illuminated with the mode $\mathbb{F}_k$. Figure 4.15a illustrates this in terms of a picture captured with the CCD camera of the setup. It shows the laser light, backreflected from two polystyrene beads attached with each other. The intensity is concentrated at the center of the beads, as they act as little lenses. The intensity
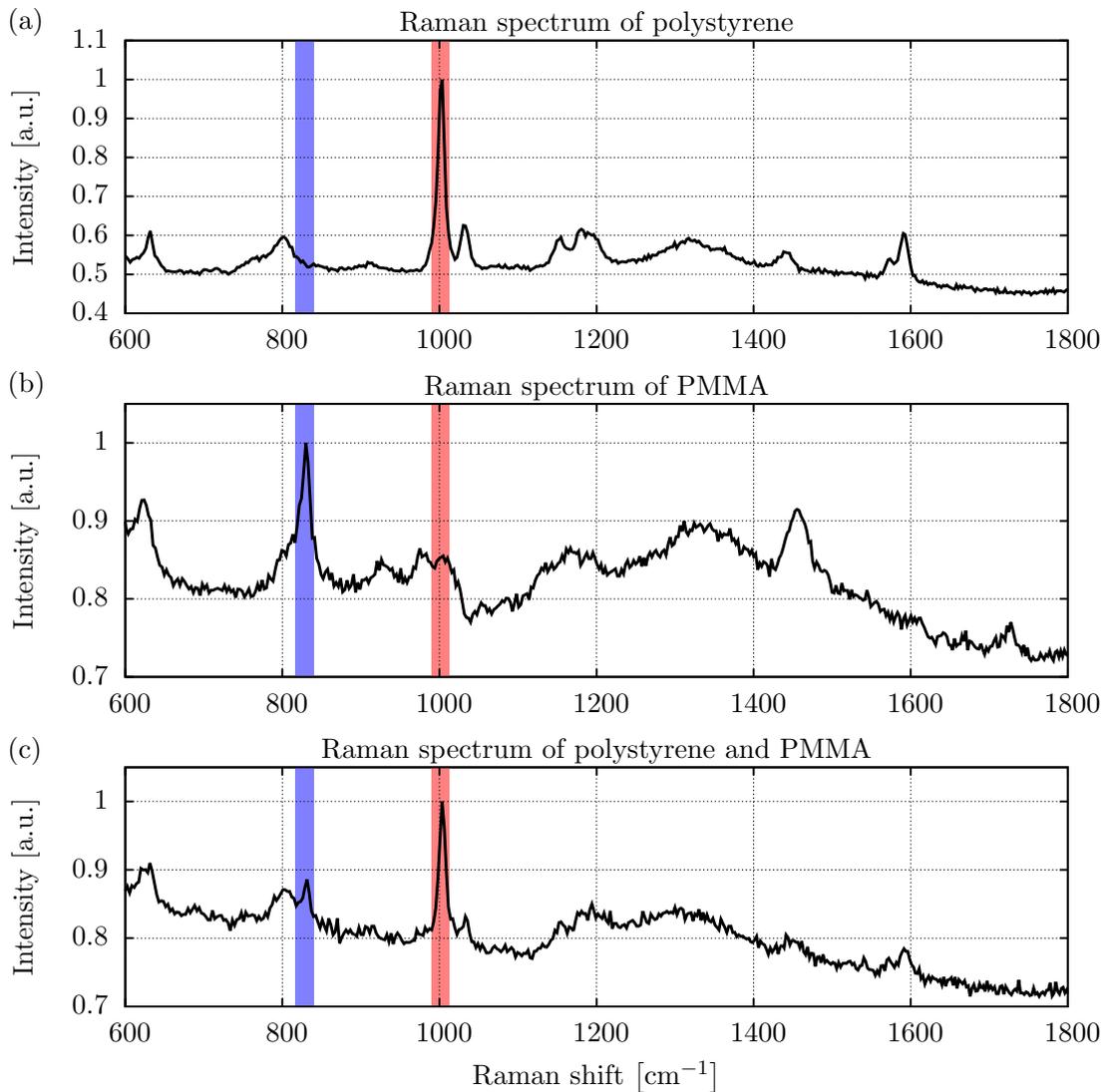
**Figure 4.14:** (a) Raman spectrum resulting from focusing a Gaussian beam of about 300 nm FWHM onto a 3 μm polystyrene bead (0.1 s exposure time). (b) The same as (a) but for a 3 μm PMMA bead. (c) Spectrum for one polystyrene bead and one PMMA bead illuminated with the 4th eigenmode and 3 s acquisition time. The area of the significant peak for PMMA is indicated in blue and the one of polystyrene in red.
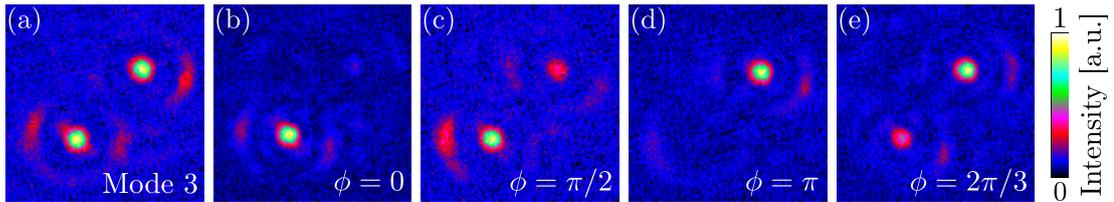
Figure 4.15: Illustration of the probing process. (a) Two beads illuminated with Mode 3, both beads are illuminated. (b)-(e) Interference of Mode 3 with the reference wave and varying phase shift ϕ causes the illumination to shift from one bead to the other. The light of the modes is concentrated in the center of the transparent beads due to microlensing induced by them.

pattern of mode $\mathbb{F}_3$ features two vertical lobes (see e.g. Figure 4.8), such that both beads are illuminated. The amplitude of c_3 is then obtained as the sum over the red part of the spectrum in Figure 4.14a. To determine the phase of c_3, the mode $\mathbb{F}_3$ is interfered with the reference wave F_{ref}. Upon interference with four phase shifts $\phi = 0, \ldots, \frac{2\pi}{3}$ between $\mathbb{F}_3$ and F_{ref}, corresponding to $P = 4$ in Equation 4.11, intensity shifts from one bead to the other due to the phase difference of π between both lobes of the intensity pattern of $\mathbb{F}_3$. This selective illumination of the beads is illustrated in Figures 4.15b to 4.15e. For each of the illuminations depicted in Figure 4.15, a spectrum similar to the one in Figure 4.14a is acquired with the spectrograph and the spectral intensity is summed within the red area of interest. This sum corresponds to the integral in Equation 4.11 and the phase of c_3 is determined as complex angle of Equation 4.11. This procedure is repeated for each OEi to get their corresponding coefficients c_k. Then a Raman image of the sample is composed by superposition of the modes $\mathbb{F}_k$ weighted with the c_k according to Equation 4.2.

With $3\,\mathrm{\mu m}$ beads in a $6\,\mathrm{\mu m} \times 6\,\mathrm{\mu m}$ sample area, the samples only exhibit very few details, such that the first four eigenmodes are sufficient for imaging. Actually, as shown later, using higher order modes is degrading the quality of sample reconstruction. Figure 4.16 depicts some OEi Raman images resulting from different sample configurations. The top row of pictures in Figure 4.16 shows brightfield images of beads captured with whitelight illumination of the sample from above. From left to right the sample consists of one polystyrene bead in the lower left corner of the ROI, one bead in the top right corner, two beads diagonally arranged, and one polystyrene bead in the top left corner together with one silica bead in the lower right corner. The latter can be distinguished from the polystyrene beads in the whitelight pictures due to its different refractive index. This last sample arrangement is chosen to demonstrate that the images discussed below are really based on the Raman peaks and not on some broad fluorescent background, as it was the case for the hole covered with Blu-Tack in Section 4.5.2. To get an idea of what to expect from a Raman image of these samples, the second row of pictures
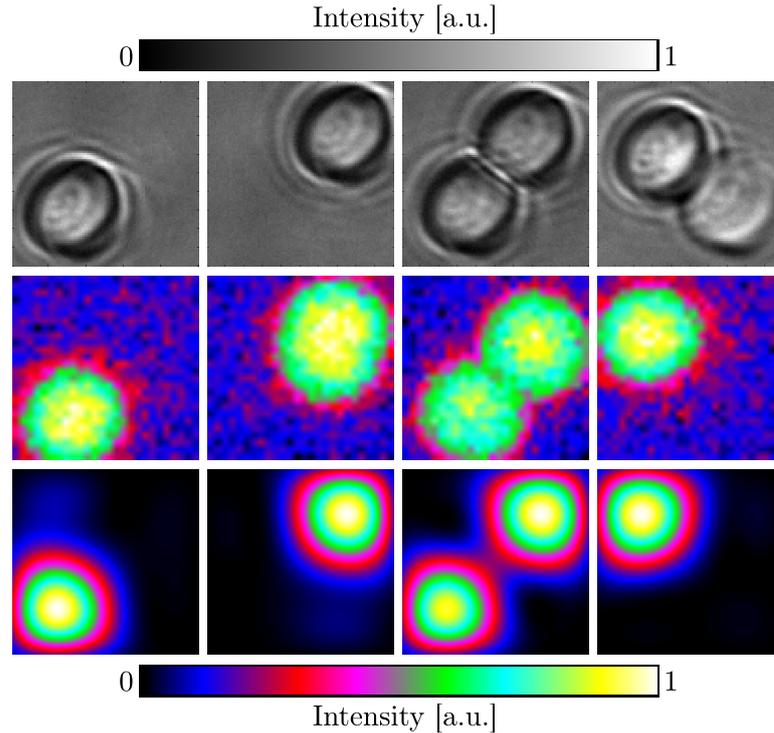
Figure 4.16: OEi Raman microscopy of polystyrene beads. From top to bottom the rows show whitelight images, Raman raster scans at 26×26 points, and OEi images acquired with 4 modes. From left to right the columns correspond to one polystyrene bead in the lower left corner of the FOV, one bead in the top right corner, two polystyrene beads in the FOV, and one polystyrene and one glass bead in the FOV. The latter is not visible in the Raman images. In the whitelight image it can be distinguished from the polystyrene bead due to its higher refractive index.

depicts Raman raster scans of the same FOV using a 26×26 scanning grid. The polystyrene beads are well reconstructed while the silica bead remains invisible. The last row of images in Figure 4.16 depicts OEi images captured with only four modes. The single beads are reconstructed well and also in the picture of two polystyrene beads two clearly distinct particles are reconstructed. The noise level in the OEi images is visually lower compared to the raster scans. But this will be discussed in detail later on.

Figure 4.17 shows OEi Raman images that result from $M = 4, \ldots, 20$ modes. The top row of pictures corresponds to a bead in the lower left corner of the FOV, the middle row to a particle in the top right corner, and the bottom row shows images of two beads. Usually a more accurate object reconstruction with finer features and particle localisation should be enabled using higher order eigenmodes. However, in the results presented in Figure 4.17 image quality clearly degrades with increasing number M of modes. This contradicts the prior statement, but can be attributed to aberrations induced by the sample itself. OEi imaging can
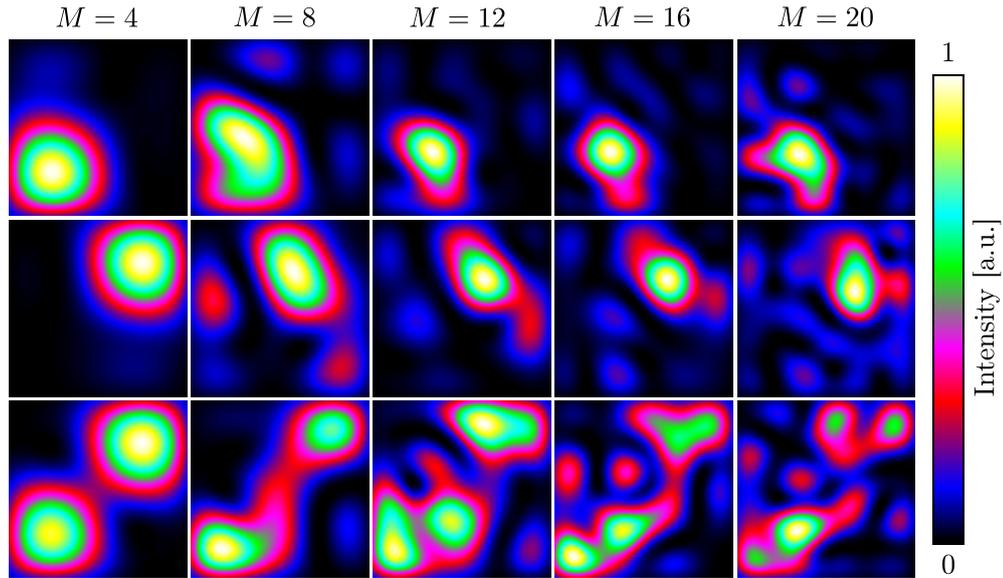
Figure 4.17: OEi Raman images resulting from probing the first three sample configurations in Figure 4.16 with different numbers M of modes. The first row corresponds to one polystyrene bead in the lower left corner of the FOV, the second row to a bead in the top right corner, and the third row shows two beads in the FOV. With increasing M the images get more noisy. This is due aberrations induced by the beads, which mainly affect the higher order modes (see text for more detailed discussion).

work well, if the modes are accurately generated in the focal plane. This will be the case for thin samples with low aberrations. But the sample for the above experiments does not fulfill this condition. With a bead diameter of $3\,\mu m$, the chosen FOV of $6\,\mu m$ size is only twice this value, hence rendering the sample more a 3D than a 2D object. The resulting aberrations are illustrated very well by the microlensing effect of the beads, visible in Figure 4.15. For the focused beam used in the raster scans this does not have such a large impact, as the phase is constant over the focal plane. In contrast to that the generation of OEi relies on phase changes of π between the intensity lobes of the modes (see Figure 2.9). For low order modes with a size of the lobes comparable to the bead size, the OEi are still reproduced in good approximation. But higher order modes seem to be significantly distorted due to the spatial phase changes induced by the transparent beads. On the other hand, the low order modes provide enough detail to reconstruct the above samples.

In the last column of pictures in Figure 4.16 it has already been shown that a silica bead, which at most exhibits broad fluorescence, is not reconstructed in the Raman images. However, a more interesting question is, if two objects with a different Raman signature can be reconstructed independently using OEi microscopy. Therefore a sample is prepared, which features both, polystyrene
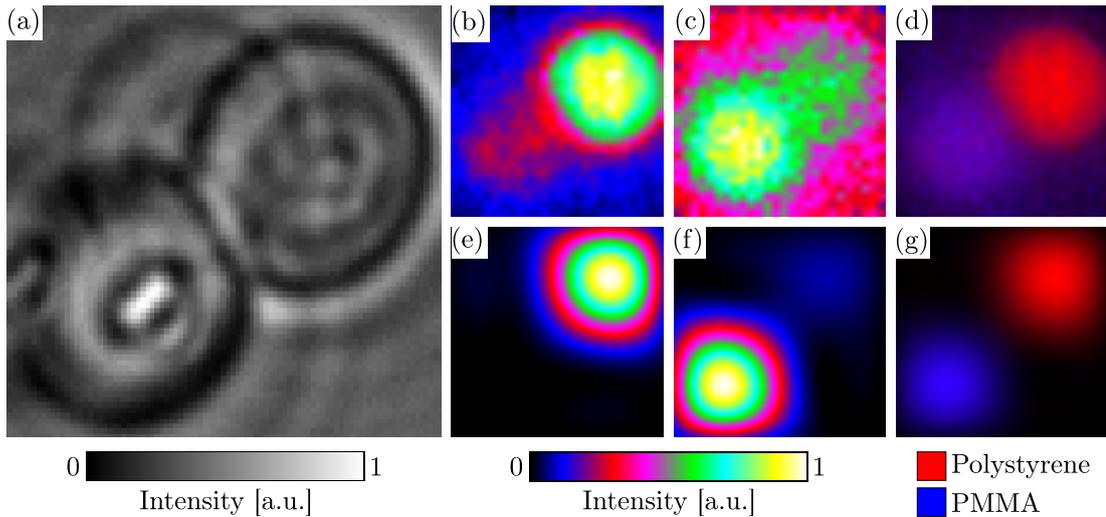
Figure 4.18: OEi Raman imaging of a polystyrene and a PMMA bead. (a) White-light image of the sample, the polystyrene bead is in the top right corner and the PMMA bead in the lower left corner. (b), (c) Raman images resulting from 26×26 points raster scans. (e), (f) OEi Raman images corresponding to (b) and (c). (d) Graphical superposition of the intensity distributions in (b) and (c), indicating the occurence of polystyrene in red and the one of PMMA in blue. (g) The same as (d), but for the OEi images.

and polymethacrylate (PMMA) beads (86935-5ML-F, Sigma-Aldrich) of the same $3\,\mu m$ diameter. The sample preperation was carried out almost identical as described for the polystyrene beads prior in this section. The difference is that first the polystyrene beads were distributed on the quartz slide. The solution of PMMA beads was added, after the liquid of the polystyrene solution evaporated. This was necessary as the beads were building big agglomerates when adding both bead solutions together. After evaporation of the liquid in the PMMA bead solution, water was added and the sample was sealed as outlined above. The main peak in the Raman spectrum of PMMA at about $830\,cm^{-1}$, highlighted by blue colour in Figure 4.14b, is well seperated from the main peak of polystyrene, highlighted red in Figure 4.14a. However, there is a small overlap of the PMMA peak with a less intense broad feature of polystyrene and the PMMA signal is significantly weaker than the one of polystyrene, which is aparent by the higher noise level in Figure 4.14b compared to 4.14a. This is why in the spectrum in Figure 4.14c, which results from illumination of both beads with the fourth eigen-mode, the PMMA peak appears as a side peak of the broad polystyrene peak at $800\,cm^{-1}$. The imaging process of this mixed material sample is then performed as described above using the first four OEi in an area which accomodates a polystyrene bead and a PMMA bead next to each other. This configuration is shown in Figure 4.18a. Using the red highlighted region of the spectra around

$1001\,\mathrm{cm}^{-1}$ results in reconstruction of the polystyrene bead, shown in Figure 4.18b for a raster scan and in Figure 4.18e as OEi image. Reconstructing with respect to the blue region around $830\,\mathrm{cm}^{-1}$ reveals the PMMA bead as raster scan in Figure 4.18c and as OEi image in Figure 4.18f. Due to the small spectral overlap of polystyrene and PMMA, the PMMA bead is partly reconstructed in the images of the polystyrene bead and vice versa. This effect is stronger visible in the raster scans than in the OEi images, which in general feature a very low background. In addition to the reconstructions of the single beads, these information are merged in Figures 4.18d and 4.18g for the raster scan and the OEi imaging, delivering multispectral images that provide material information.

Above it was visually observed that the OEi Raman images feature a lower background than the raster scans. However, comparing the noise level of both methods in terms of the presented results is not trivial. The question is, OEi images with which number of modes should be compared to the raster scans? On the one hand, the images resulting from only 4 modes definitely have the lowest background level, but on the other hand the raster scans with their 676 points will definitely provide a more accurate localisation of the beads. On the other hand, using more modes for the OEi imaging, which should in principle enhance the localisation capabilities, turned out to degrade the image quality instead of improving it due to the sample's thickness. Based on these considerations, a quantitative comparison of the noise levels of both methods is postponed to the next Section 4.6.2. There a SERS sample with $200\,\mathrm{nm}$ gold spheres is utilised, which is closer to being a 2D sample than the $3\,\mu\mathrm{m}$ beads and hence allows OEi imaging with a larger number of modes.

In conclusion, the results in this section showed, that OEi imaging also works on the basis of a sample's Raman signal. First, polystyrene beads were imaged using only the first four eigenmodes. Then a mixed sample consisting of a polystyrene and a PMMA bead, featuring different Raman signatures, was imaged. Here, both beads could be reconstructed independently based on their main peak, hence demonstrating hyperspectral OEi microscopy. A disadvantage of OEi imaging found in the course of the experiments was its sensitivity to aberrations induced by the sample. Higher order OEi were disturbed by the phase change induced by the transparent beads, such that using them was decreasing the image quality instead of increasing it. Raster scans with a focused beam were less sensitive to this sort of distortion. Visually, OEi images provide a lower noise level compared to raster scans. However, this has to be confirmed in the next Section 4.6.2 due to the aberration problems with OEi imaging of thick samples.

4.6.2 Localising SERS hotspots with OEi imaging

The results in the previous Section 4.6.1 have shown that OEi imaging with higher order modes suffers from strongly aberrating samples, such as the $3\,\mu\mathrm{m}$
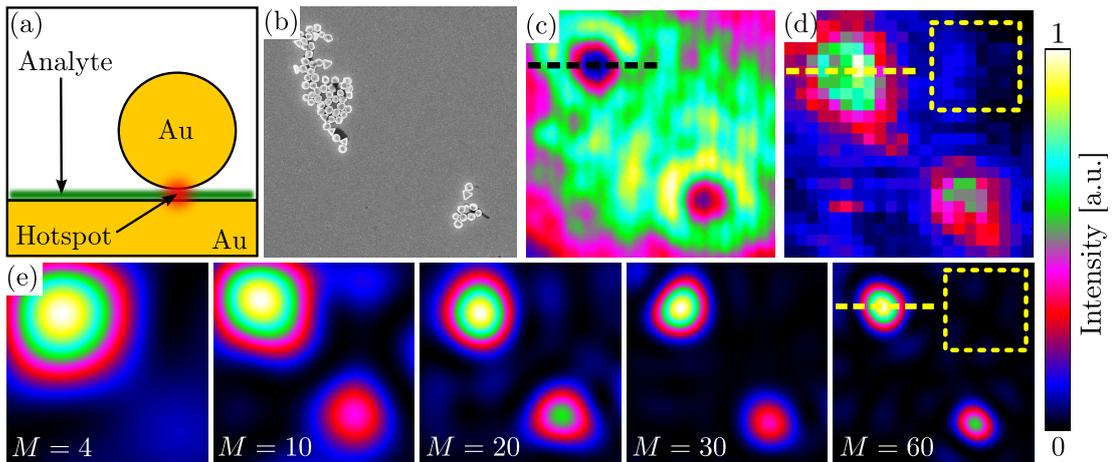
Figure 4.19: (a) Schematic of the SERS sample: 200 nm gold particle on gold surface, which was coated with the analyte, in this case dithiol. The hotspot between gold layer and sphere gives rise to SERS. (b) SEM image of a sample area similar to the imaged one (thanks to Kapil for taking that image). (c) Backreflectec laser light from the 9 µm × 9 µm ROI chosen for imaging. Two agglomerates of gold particles are visible as dark spots. (d) Raman raster scan of the scenery. (e) OEi imaging reconstruction of the scene for increasing number M of modes.
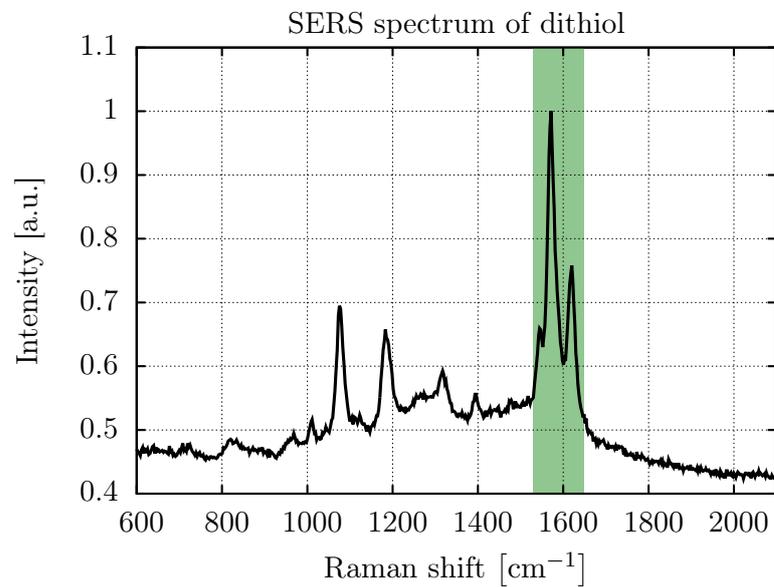
Figure 4.20: SERS spectrum of dithiol: Normalised counts in dependence on the Raman shift. The peaks used for the imaging process are highlighted in green.
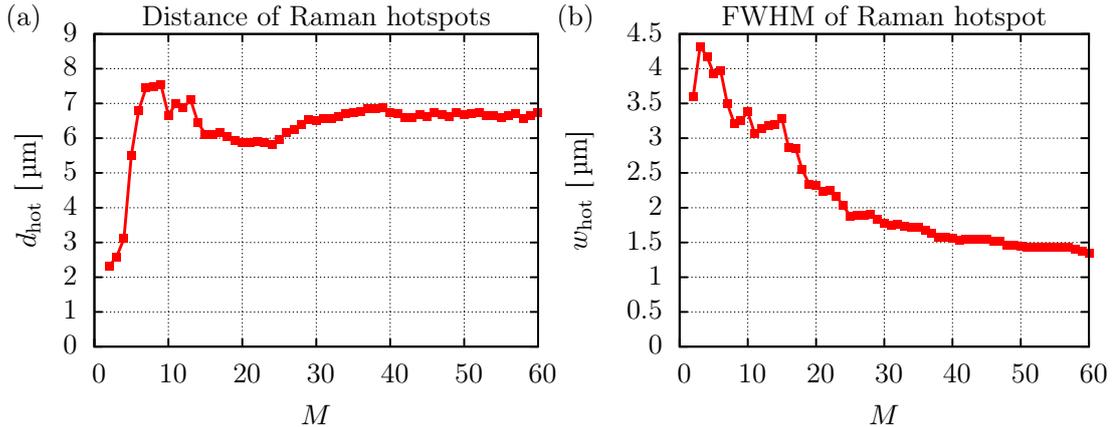
Figure 4.21: (a) Distance between SERS hotspots and (b) FWHM of the top left hotspot in dependence on the number M of probes.

beads that were used. The logical step would be to employ thinner samples, such as smaller beads of e.g. $1\,\mu m$ diameter. However, a thinner sample also means less sample volume and in essence a weaker Raman signal. Hence, spreading the OEi illumination over the same FOV as in the previous experiments, the Raman signal with $1\,\mu m$ polystyrene beads was found to be not sufficient to perform OEi imaging experiments. An efficient method to obtain a strong signal from a small sample volume is SERS, described in Section 4.3. Hence, in this section a SERS sample provided by Dr Sumeet Mahajan (Department of Physics, Cavendish Laboratory, University of Cambridge) is employed. Its structure is arranged in the following way [201]: A monolayer of the analyte, in the present case dithiol [202], is deposited on a flat layer of gold. Then gold spheres of about $200\,nm$ diameter are deposited on the dithiol. A schematic of this arrangement is depicted in Figure 4.19a and an SEM image of the sample is provided in Figure 4.19b. The dithiol binds to both, the flat gold layer and the gold spheres, generating a $1.3\,nm$ gap between them. Upon illumination with laser light, this small gap gives rise to a strong field enhancement and hence to a strong SERS signal, which is shown in Figure 4.20.

To image this sort of sample, the oil emersion objective used before is unsuitable, as the object itself would be covered with oil. Hence the objective was change for an air objective (Nikon $60 \times /0.8\ \infty/0.17$ WD 0.3). For the imaging a sample region of about $9\,\mu m \times 9\,\mu m$ was selected that features two agglomerates of particles. Figure 4.19c shows a picture of this sample area captured with the CCD camera upon illumination with the reference wave. In the following this is referred to as reference image. The two bunches of particles are visible as dark spots, as they reflect less light than the flat gold surface. For imaging, the spectral region with the two largest peaks at a Raman shift of around $1600\,cm^{-1}$, highlighted green in Figure 4.20, was selected. The resulting Raman raster scan
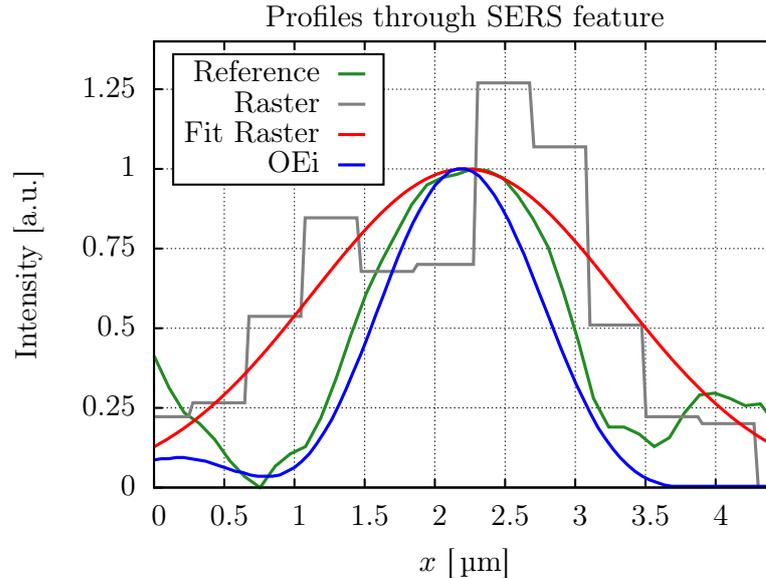
Figure 4.22: Profiles along the dashed lines in Figures 4.19c, 4.19d, and 4.19e. The FWHM of the curves are: 2.57 µm for the fit onto the raster scan, 1.58 µm for reference wave illumination, and 1.30 µm for OEi imaging.

at $22 \times 22 = 484$ points is depicted in Figure 4.19d, revealing the areas of high SERS activity around the two particle agglomerates. Figure 4.19e depicts OEi Raman images reconstructed from illumination with $M = 4, \ldots, 60$ modes. With increasing mode number the intensity distribution in the images is visually converging against the SERS hotspots in the sample. In Figures 4.21a and 4.21b, which depict the distance d_{hot} between the two hotspots and the width w_{hot} of the top left spot, this can also be observed quantitatively. With increasing M both graphs converge towards a steady state. Hence, for $M = 60$ it can be assumed that an image is reconstructed, whose quality would not be significantly improved further using higher order OEi.

Comparing the raster scan in Figure 4.19d and the OEi image for $M = 60$ in Figure 4.19e with the reference image in Figure 4.19c, the size of the features seems to be more accurately reconstructed in the OEi image. This impression is confirmed quantitatively in Figure 4.22, which shows horizontal profiles through the bigger of both particle agglomerates. The blue plot for the OEi image agrees quite well with the reference plot in green. Due to the low pixel resolution of the raster scan (gray plot), a Gaussian fit is done for this data, coloured red. With 2.57 µm, the FWHM of this fit is twice the width of 1.30 µm resulting from the OEi imaging process. This discrepance is probably attributed to two effects: First, with 22 scanning points to cover a distance of 9 µm, the step width between two pixels corresponds to about 400 nm on the sample. This is relatively large compared to the widths of 1.3 µm and 1.58 µm, measured in the OEi scan and the

reference image respectively and thus will influence the measured feature width significantly. Actually, this step width is also clearly above the Nyquist limit of half the diffraction limit, which in this case would require a scan with 250 nm steps. Furthermore, the features of the sample will additionally be broadened by the visually higher background in the image produced by the raster scan, which is investigated in more detail below.

As already observed in Section 4.6.1, the OEi images visually exhibit a lower background and hence a higher signal-to-noise (S/N) level compared to the raster scans. Here this observation is confirmed quantitatively using the raster scan image in Figure 4.19d and the OEi image with $M = 60$ modes in Figure 4.19e. For an objective comparison, the exposure times for the acquisitions of these images were chosen such, that about the same amount of light, i.e. intensity, was used to generate both images. The noise level in each of the pictures is quantified as average in the dotted square relative to the signal, which is the largest value of the main SERS feature. For the raster scan, a S/N of 17.7 is measured, which is almost an order of magnitude less compared to the S/N of 145.6 measured in the OEi image. Consequently, also the fluctuations of the background are less in the OEi image. They are quantified as standard deviation from the mean in the dotted square. For the raster scan these background fluctuations are measured to be 3.4 %, which is 7× higher then the value of 0.5 % obtained for the OEi image. The reason for this is the phase information of the OEi, as already discussed in Section 4.2.2: Superposition of the modes with the correct phase relationship enables a very efficient cancellation of the background.

Overall, the results in this section show, that OEi imaging is well suitable for SERS microscopy. Sufficient signal is provided due to the SERS effect, such that also thin samples can be employed. In contrast to Section 4.6.1, this allows the usage of higher order OEi, as they do no longer suffer from aberrations induced by the sample. Using 60 modes only, the width of a SERS feature was demonstrated to be confined to only half the width that was enabled by a raster scan with 484 points, which corresponds to almost an order of magnitude compression.

4.7 Summary & conclusion

This section is briefly summarising the main results and conclusions that can be drawn from this chapter. After a review of the field of indirect or "ghost" imaging, the basic principle of OEi imaging was outlined. Then OEi imaging was compared in simulations to computational ghost imaging (CGI) as the most similar indirect imaging method. It was found that optical eigenmode imaging requires 2-3 orders of magnitude less samplings than conventional CGI. Compared to the application of compressive sensing methods in CGI, OEi imaging would still save 1-2 orders of

magnitude acquisitions. However, the standard imaging modality with respect to the target applications of OEi imaging, namely fluorescence and Raman imaging, is laser scanning. Hence OEi imaging has also been compared to raster scanning imaging in simulations, investigating the resolution and the localisation of object features. The major advantage of OEi imaging was found for a low number of probes, i.e. eigenmodes or scanning points respectively. To achieve subdiffractive localisation of sample points, OEi imaging was requiering an order of magnitude less probes than a raster scan. In terms of resolution, four times less OEi than scanning points were needed to approach a diffraction limited resolution. But for a practical implementation one has to keep in mind that, due to the phase measurement involved in the OEi acquisition process, at least three exposures must be performed to gain the necessary information for one eigenmode. This diminishes the advantage of OEi imaging especially with reference to resolution. But with respect to localisation capabilities still a factor three improvement remains.

After the simulations, attention was paid to the experimental implementation of OEi imaging. First the effects of fluorescence and (surface enhanced) Raman scattering as target regimes for OEi imaging were reviewed. Before any imaging experiments were carried out, the experimental generation of optical eigenmodes was checked. Positioning a mirror in the focal plane, the intensity distributions of the experimental OEi were found to visually agree well with the simulated ones. Furthermore, experimentally obtaining the inner products of the OEi, their orthonormality was also found to be satisfied in good approximation. Having the correct implementation confirmed, a first macroscopic transmission OEi imaging experiment was carried out using a test target consisting of three holes in an aluminium plate. The reconstructed images of that sample were in good agreement with prior simulations. As a first step towards spectroscopic imaging, one of the holes was covered with a thin layer of Blu-Tack which was exhibiting some fluorescence. Based on that signal, the corresponding hole could be reconstructed, hence proving the applicability of OEi imaging in the fluorescent regime.

As a first microscopic Raman imaging experiment, $3\,\mu m$ sized beads of polystyrene and PMMA were employed, as they feature relatively strong Raman activity. Based on their Raman signature, OEi images of the beads could be reconstructed using only the first four modes. The chemical selectivity was demonstrated with both a polystyrene and a PMMA bead in the field of view. Selecting the corresponding spectral region in the acquired signals enabled seperate reconstruction of the beads according to their material, hence showing the ability of OEi for hyperspectral imaging. For all experiments, the correctness of the OEi images was confirmed by raster scans. One limitation of OEi imaging found in the course of imaging the beads is the sensitivity of OEi to sample aberrations. Instead of increasing the image quality, using higher order modes was decreasing the quality. This was attributed to the fact, that the experimental generation of OEi requires to obey a precise phase relationship over the field of

view. Strongly aberrating samples such as the arrangement of beads, which was already more a 3D than a 2D sample, affect this relationship. In contrast to that, a Gaussian beam has the same phase over its whole cross section, rendering it quite insensitive to spatial aberrations over the sample.

A further drawback of OEi imaging with respect to weakly scattering samples is, that the intensity of the OEi is spread over the whole field of view. Hence, only a small spatial fraction of the pupil, i.e. the SLM, is utilised for each mode, leaving a lot of light unused upon illumination of the SLM with a Gaussian beam. These two effects add up in a negative way, leaving relatively low focal intensities for sample illumination. This is why the strongly aberrating $3\,\mu m$ beads were used in the first experiments, $1\,\mu m$ sized beads for example simply did not deliver a sufficient signal. To explore OEi imaging for non-aberrating samples, advantage was taken of the SERS effect in terms of imaging a sample featuring SERS hotspots. In this context, OEi imaging with up to 60 modes was performing very well. Compared to a raster scan at about 500 points, OEi imaging delivered a twofold improved lateral resolution and a S/N ratio which was increased by an order of magnitude.

In conclusion, OEi imaging was investigated in simulations and experiments for imaging in transmission as well as in the regimes of fluorescence and (surface enhanced) Raman scattering, also demonstrating the option of hyperspectral imaging. Major advantages in comparison to CGI and raster scanning imaging is the compressive aspect and the improved S/N ratio shown in the Raman regime. Drawbacks are the sensitivity to sample aberrations and low focal intensities, especially affecting the usage in Raman imaging. Relatively little can be done about sample aberrations, but e.g. biological samples such as cells and tissues certainly aberrate much less than the investigated beads, which probably represent something close to the worst case scenario. An obvious way to deal with the intensity issue is to use stronger light sources and shorter wavelengths. The latter increases the Raman cross section, but also leads to more fluorescence. An alternative way to increase the OEi intensity in the focal plane is a change of the experimental setup such, that the SLM modulates the light in a confocal plane instead of a reciprocal plane of the focal plane. As can be seen in Figure 2.8, in the reciprocal plane the OEi only occupy a small fraction of the available area, as they correspond to different spatial frequencies. Hence a lot of light is lost when illuminating the SLM with a plane Gaussian beam. If the SLM would be positioned in a confocal plane, the OEi in Figure 2.9 would be encoded, which always fill the whole available area. This would enable usage of the full SLM area for each mode, which should dramatically increase the OEi's intensity in the focal plane.

Chapter 5

Coherent control of gold nanostructures

The concentration of light in the vicinity of metallic nanostructures has applications in optical trapping [73] and sensing schemes based on fluorescence [76] or surface enhanced Raman spectroscopy [77]. In combination with spatial information, molecular sensing enables for example analysis of subcellular signaling [76]. One way to achieve spatially selective field enhancement is to pattern the nanostructure itself [73]. However, this method is inflexible as, once fabricated, the pattern is fixed. A more convenient way is to fabricate periodic arrays of nanostructures and then spatially selective excite array elements by shaping the incident light field. In Reference 66 pulse shaping has been combined with an iterative optimisation procedure to tailor the near field response of a silver nanostructure. An approach based on continous light flow relies on the illumination with higher order transverse modes, for example Hermite-Gaussian (HG) modes [68], generated by static phase optical elements. Upon illumination with a plane Gaussian beam, a nanoantenna consisting of two arms gives rise to an intensity hotspot located in the gap between both arms. Illuminating the same configuration with the HG_{10} mode, which features two intensity lobes which are phase shifted by π with respect to each other, enables to drive both antenna arms out of phase. This results in two intensity hotspots, one at the center of each arm. Two confirm that this is a phase effect, a Laguarre-Gauss (LG) mode, in particular LG_{20}, was used, which also features zero intensity in the center, but the same phase on both arms of the antenna. In that case the resulting near field excitation is similar to illumination with a Gaussian beam, hence confirming that the phase on the nanostructure plays a key role for its control. Recently, an SLM divided into superpixel that are imaged onto a nanostructure has been used to implement flexible phase and amplitude shaping for the coherent control of surface plasmons [69]. In Reference 203 the approach of using higher order modes is generalised in simulations by decomposing the light field on an array of nanoantennas into optical eigenmodes. In contrast to the concept in Reference 69, the optical eigenmodes are not a static set of modes, which spans over the continous space.

Instead they are defined with respect to isolated points corresponding to features of the nanostructure. They can be flexibly defined on freely chosen points on nanostructure, addressing each of them with an individual phase and intensity. Once the OEi are determined on a structure, their superposition can be tailored in order to match an intensity and phase distribution of choice with respect to the selected nanoelements. In this chapter the idea proposed in Reference 203 is verified experimentally with the following organisation: Section 5.1 outlines the basic principle of OEi based coherent control. The experimental setup for the experiments is presented in Section 5.2. Section 5.3 deals with coherent control experiments using nanoantennas and nanopads. As a further feature, focusing onto nanoelements through turbid media using OEi is investigated in Section 5.4. In Section 5.5 the work is summarised.

5.1 Principle of OEi based coherent control

In the following two sections the principle of OEi based coherent control is decribed. The whole process can be divided into two steps. First the light field on a nanostructure is decomposed into OEi. This is described in Section 5.1.1. In the second step, outlined in Section 5.1.2, the superposition of these OEi is determined in order to match user defined target functions such as addressing one or multiple elements of the nanostructure.

5.1.1 Decomposing the light on a nanostructure into OEi

The first step of OEi based Coherent Control is to decompose the light field on the nanostructure into orthogonal modes. In contrast to the methods treated prior in this work, the modes that are determined here are not orthogonal over a region of continous space, but with respect to descrete points, which are chosen to be at the positions of features of the structure. After selecting a desired number M of points P_m defined by a pair (x_2, y_2), the sample is illuminated with N test fields F_i, that are generated by encoding fields E_i on an SLM. Amplitude and phase of each field F_i at the point P_m with respect to a reference wave F_{ref} are determined by an interference technique, slightly different to what was described in Sections 4.4.2 and 4.4.3:

$$F_i(P_m)\, F_{\text{ref}}^*(P_m) = \frac{1}{4} \sum_{p=0}^{3} e^{i\frac{\pi}{2}p} \left| F_i(P_m) + e^{-i\frac{\pi}{2}p}\, F_{\text{ref}}(P_m) \right|^2. \qquad (5.1)$$

The absolute square in Equation 5.1 is acquired on a CCD with the corresponding field $E_i + e^{-i\frac{\pi}{2}p}\, E_{\text{ref}}$ encoded on the SLM. In analogy to Section 4.4.3, the phase

of $F_i(\mathrm{P}_m)$ is obtained as complex angle of Equation 5.1, while the amplitude is defined as the square root of an acquisition with only the reciprocal field E_i encoded on the SLM. Knowing the fields F_i at all points P_m, optical eigenmodes with respect to these points are calculated according to Section 2.5.1 from the eigenvectors and eigenvalues of the intensity operator $\mathbf{M}^{(0)}$. In the case presented here the integration in Equation 2.28 for the calculation of the elements of $\mathbf{M}^{(0)}$ corresponds to a sum

$$M_{ij}^{(0)} = \sum_{m=1}^{M} F_i(\mathrm{P}_m)\, F_j^*(\mathrm{P}_m) \tag{5.2}$$

over the points P_m. The modes $\mathbb{F}_k$, which are determined according to Equation 2.32, are orthogonal with respect to the nanoelements represented by the points P_m. They are generated by encoding the fields $\mathbb{E}_k$, composed as in Equation 2.31, on the SLM. The orthogonality of the $\mathbb{F}_k$ is experimentally demonstrated in Section 5.3.2. If the test fields F_i were sufficiently probing the degrees of freedom of the system, there are exactly M eigenmodes that have nonzero eigenvalues $\lambda_k^{(0)}$, meaning nonzero intensity on the M points P_m. In the next Section 5.1.2 it is shown how the superposition of these M OEi $\mathbb{F}_k$ can be tailored in order to generate flexible optical landscapes on a static nanopattern.

5.1.2 Shaping illumination by approximating target functions

After obtaining the OEi $\mathbb{F}_k$, their superposition can be tailored in order to match user defined target functions. A target function defines a target field $T_m \equiv T(\mathrm{P}_m)$ at each of the points P_m. The complex weighting coefficient c_k for each mode $\mathbb{F}_k$ and $\mathbb{E}_k$ respectively is defined in discrete analogy to Equation 4.1 by the projection of each OEi onto the target:

$$c_k = \sum_{m=1}^{M} T_m\, \mathbb{F}_k(\mathrm{P}_m). \tag{5.3}$$

Encoding the superposition

$$S = \sum_{k=1}^{M} c_k\, \mathbb{E}_k \tag{5.4}$$

on the SLM delivers the desired target field

$$T = \sum_{k=1}^{M} c_k\, \mathbb{F}_k. \tag{5.5}$$
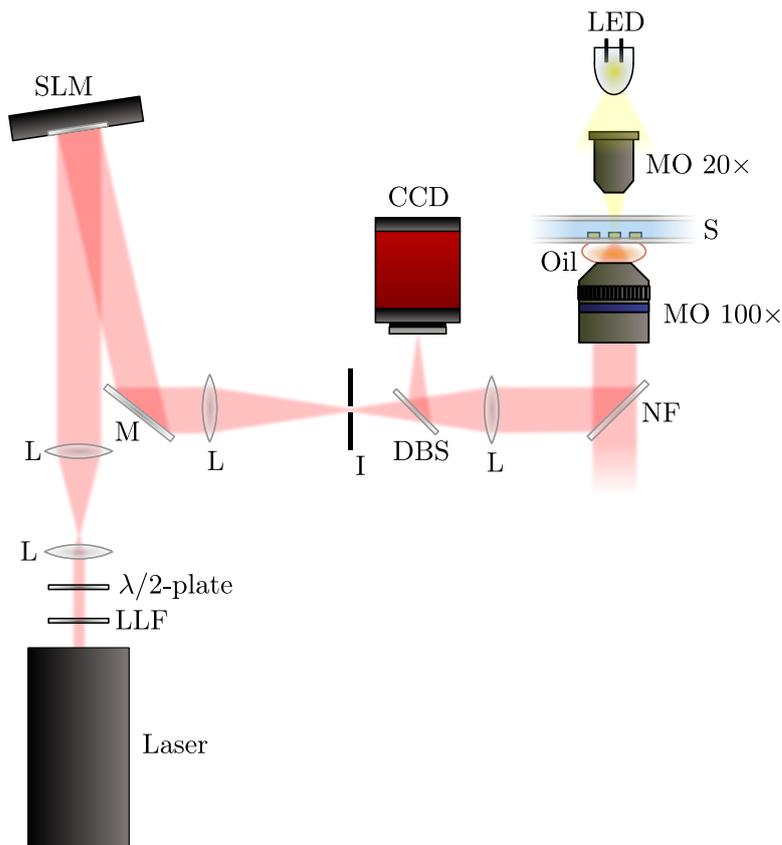
Figure 5.1: Experimental setup for optical eigenmode based coherent control. LLF: Laser line filter at 785 nm; L: Lens; SLM: Spatial light modulator; M: Mirror; I: Iris to filter out first diffraction order of the SLM; DBS: Dichroic beam splitter reflecting visible light and transmitting infrared light; CCD: CCD camera; NF: Notch filter reflecting the laser wavelength of 785 nm; MO: Microscope objective; S: Sample.

Like that, the light field on a nanostructure can be "coherently" controlled. An experimental realisation of OEi based coherent control is shown in Section 5.3 with gold nanoantennas and nanopads. But the next Section 5.2 first briefly describes the utilised setup.

5.2 Setup

The experiments on Coherent Control employ a subset of the setup already described in Section 4.4.1.2. For the reader's convenience this subset is again depicted in Figure 5.1. The light source is a 1 W Ti:Sapphire laser (3900S, Spectra-Physics) pumped with a 6 W Nd:YAG laser (Verdi V-6, Coherent Inc.). Its beam is collimated and reflects upon the display of a phase only SLM (LCOS-SLM X10468-02, Hamamatsu Photonics), which is wavefront corrected based on the
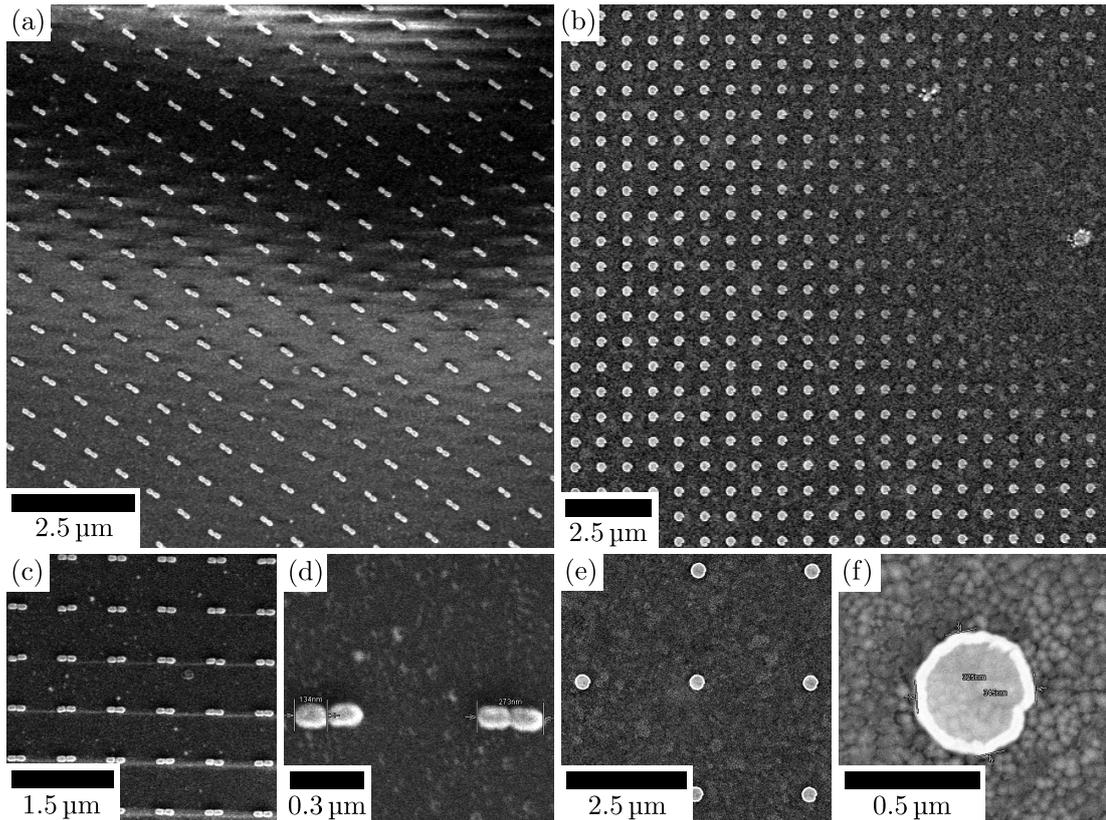
Figure 5.2: Overview over arrays of 800 nm spaced (a) nanoantennas and (b) nanopads. (c), (d) Subsets of (a). (e) Subset of an array of 2500 nm spaced gold-pads. (f) Single goldpad. Thanks to Andrea for taking these pictures.

method in Reference 147. The modulated 1st order light is coupled into a microscope objective ($100 \times / 1.30$ Oil UPlanFL N, Olympus) and illuminates a sample consisting of gold nanostructures. The backscattered light is imaged onto a CCD camera (Basler pilot piA640-210gm, 648 pixel $\times$ 488 pixel resolution, 7.4 µm pixel pitch). To obtain brightfield images of the sample, it can be illuminated from above by a light emitting diode.

5.3 Coherent control of nanoantennas and nanopads

After outlining the principle of OEi based coherent control in Section 5.1, this part deals with its experimental implementation. As test objects for this purpose, periodic patterns of gold nano elements, fabricated by electron beam lithography, are used (many thanks to Andrea Di Falco for fabricating these nanostructures).

Gold is a material which is often used in sensing applications, as it enables strong plasmonic field enhancement and does not exhibit strong corrosion. In particular, the utilised structures were arrays of nanoantennas and nanopads. Individual elements were about 300 nm in size and the spacing between them varied from 2500 nm to 400 nm. The latter equals about half the wavelength $\lambda = 785$ nm of the laser light used for the experiments, hence allowing to challenge the limits of far field coherent control of the structures. Figure 5.2 exemplarily depicts some scanning electron microscope (SEM) images of the patterns. In Section 5.3.1 it is illustrated how the light field on these nanostructures is decomposed into OEi. The orthonormality of the OEi is checked in Section 5.3.2. Section 5.3.3 deals with the generation of tailored optical landscapes on the samples. The accuracy of generating these target fields is investigated in Section 5.3.4. Finally, in Section 5.3.5 it is demonstrated that, using the OEi method, it is possible to reduce the illumination crosstalk of neighbouring nanoelements.

5.3.1 Decomposition into OEi

Here it is experimentally illustrated how the light field on a nanostructure is decomposed into orthogonal modes. Figure 5.3a depicts a whitelight image of an array of 2500 nm spaced goldantennas. From these a subset of 3×3 elements is selected, as shown in Figure 5.3b. In Figure 5.3c this subset is almost homogenously illuminated with an expanded laser beam, which serves as reference wave F_{ref} for the probing with the test fields F_i. In a first step, $M = 9$ points P_m are selected, one on top of each antenna. To reduce the sensitivity to noise in the following measurements, the intensity for a point is averaged in a square of 11 pixel $\times$ 11 pixel centered at that point. This square is exemplarily indicated in yellow on top of one of the antennas in Figure 5.3c.

The next step is to experimentally measure amplitude and phase of the test fields F_i. In principle every set of fields that is sufficiently covering the degrees of freedom on the nanostructure would be suitable for probing. However, to keep the probing time as short as possible, the theoretically derived OEi used in Section 4 are chosen to serve as test fields here. These are orthogonal in the area that accomodates the 9 antennas, hence they should also very efficiently probe the 9 degrees of freedom given by the points P_m. Exemplarily, Figure 5.3d depicts the backreflection of Mode 20 from the glass surface next to an array of 800 nm spaced gold pads and a triangular marker. The probing is then carried out as described in Section 5.1.1, using the eigenmodes shown in Figure 2.9 as test fields F_i. The process is illustrated in detail by means of Figures 5.4a to 5.4g. Figure 5.4a shows the complex map of one of the test fields. In Figure 5.4b the antennas are illuminated with that field, highlighting all of them. Interfering the probe with the reference wave at various phase shifts switches individual antennas
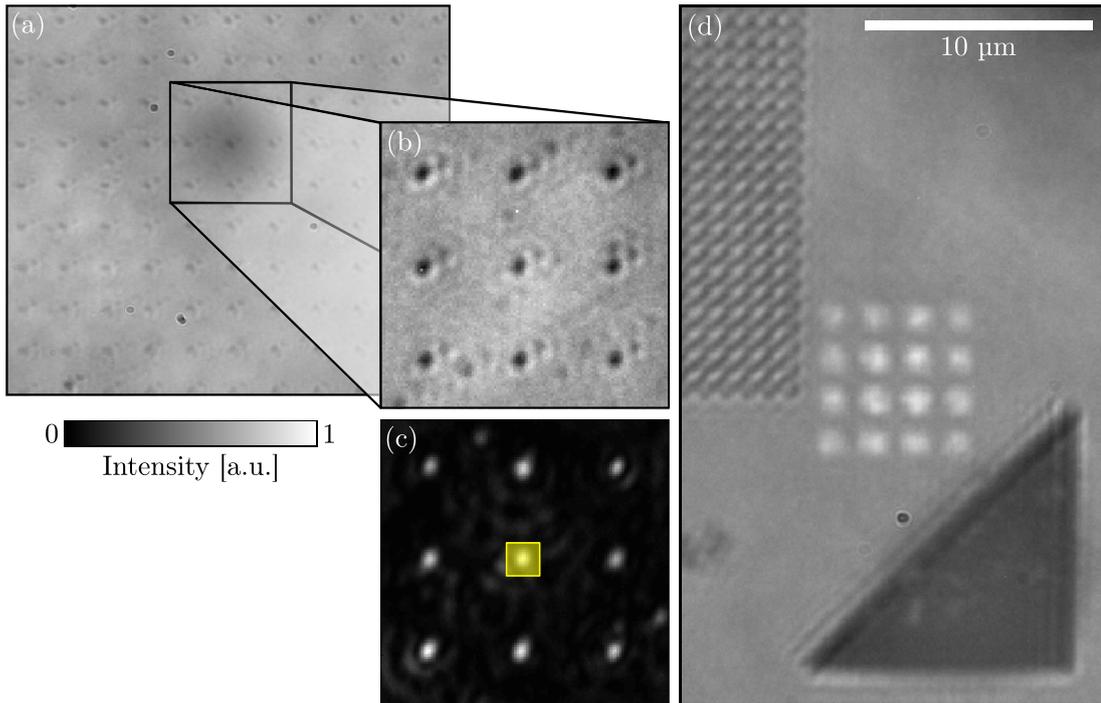
Figure 5.3: (a) Whitelight image of nanoantennas. (b) Zoom of 3×3 antennas in (a). (c) Antennas in (b) illuminated with the reference wave. The spacing of the antennas is 2.5 µm. The yellow square indicates the area over which the intensity is integrated for the reconstruction of the field on that antenna. (d) Backreflection of Mode 20 from the glass slide in vicinity of an array of 800 nm spaced nanopads and a triangular marker. The structures are slightly out of focus due to the wavelength difference between the whitelight illumination and the 785 nm laser light.

"on" and "off", as depicted in Figures 5.4c to 5.4f. This allows for the complex field on the antennas, shown in Figure 5.4g, to be reconstructed.

After reconstruction of all (in this case $N = 164$) test fields F_i, OEi $\mathbb{F}_k$ in the focal plane and $\mathbb{E}_k$ on the SLM are determined as described in Section 5.1.1. As there are 9 points/antennas, only 9 out of the 164 modes $\mathbb{F}_k$ feature nonzero intensity on these points. These 9 modes are illustrated in Figure 5.4h. The intensity distributions captured with the CCD, when the corresponding fields $\mathbb{E}_k$ are encoded on the SLM, are depicted in Figure 5.4i and show good agreement with the semi-theoretical OEi in Figure 5.4h. Furthermore, the eigenvalues $\lambda_k^{(0)}$ are depicted as red bars in Figure 5.5, clearly highlighting the cutoff for $k = 9$. The blue bars indicate the eigenvalues when probing a set of 49 nanopads that are spaced 800 nm from each other. With a point P_m defined on each of the pads, the cutoff is at $k = 49$ in this case.

An advantageous feature of the OEi over e.g. two displaced foci is, that they are orthogonal with respect to the selected nanoelements. This is at least true
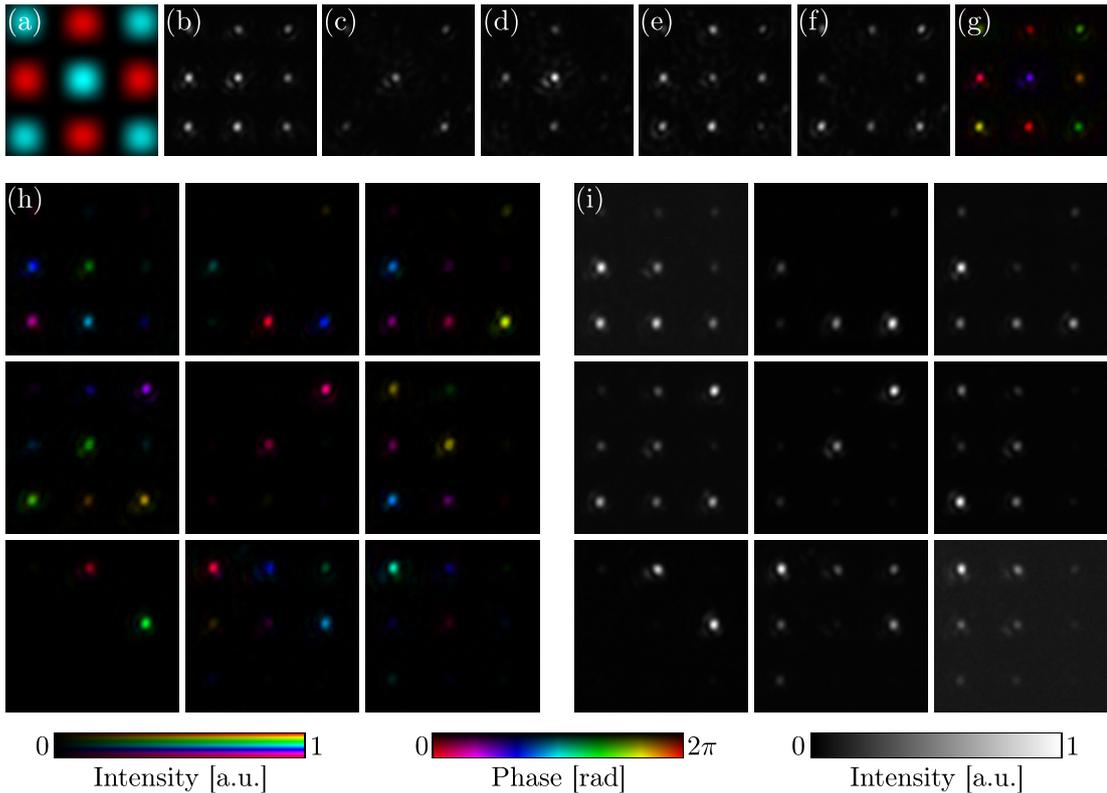
Figure 5.4: Probing with mode 11 (a). (b) Just mode. (c)-(f) Interference with reference wave and phase shifts of (c) 0, (d) $\pi/2$, (e) π, and (f) $3\pi/2$. (g) Reconstructed field. (h) Theoretical and (i) experimental OEi.

in theory. In the next Section 5.3.2 this orthogonality is also investigated experimentally.

5.3.2 Orthogonality of the OEi

As the OEi $\mathbb{F}_k$ are composed from the orthogonal eigenvectors of the intensity operator, the fields themselves are orthogonal with respect to the points P_m, hence fulfilling

$$\sum_{m=1}^{M} \mathbb{F}_k(P_m)\,\mathbb{F}_l^*(P_m) = \delta_{kl}. \tag{5.6}$$

The image denoted as "Theory" in Figure 5.6 depicts this relationship for OEi that were calculated on a 3×3 subset of 800 nm spaced nanopads with the row and column numbers indicating the indices k and l respectively. The displayed matrix is purely diagonal, so the OEi are orthogonal in theory.

Eigenvalue spectra
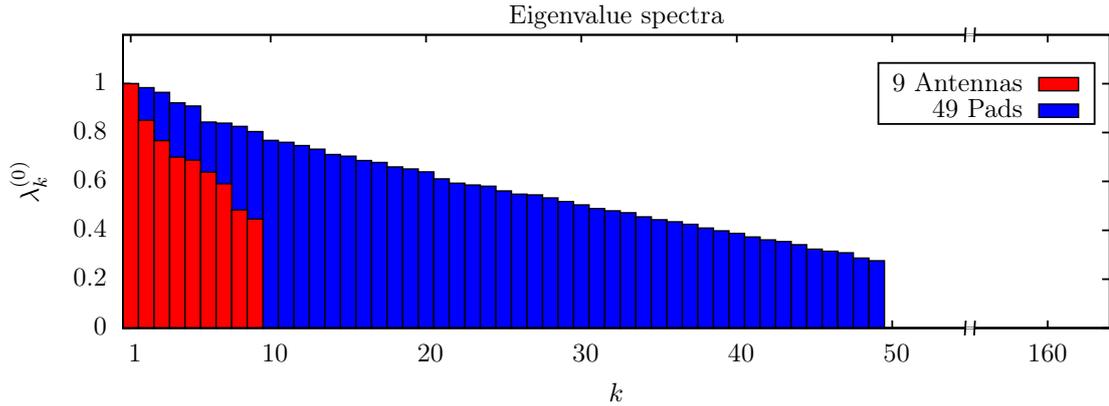
Figure 5.5: Eigenvalues of the intensity operator when probing 9 nanoantennas (red boxes) and 49 nanopads (blue boxes) with 164 test fields.
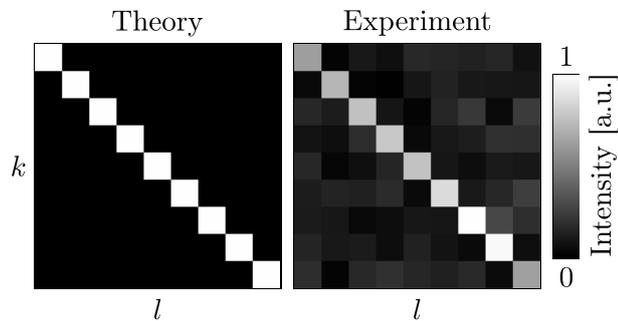
Theory   Experiment

Figure 5.6: Theoretical and experimental orthogonality matrix for the optical eigenmodes on a 3×3 array of 800 nm spaced nanopads.

Experimentally, orthogonality is determined as already described in Section 4.4.2 using the polarisation identity. The image denoted "Experiment" in Figure 5.6 depicts the experimentally resulting orthogonality relationship (5.6) for the 9 nanopads. The observed agreement between theory and experiment is visually similar to the one already observed in Figure 4.9, Section 4.4.2, and allows the conclusion of orthogonality with respect to the selected nanoelements in good approximation. The, according to Section 4.4.2, measured errors of $\sigma_{\mathrm{orth}} = 0.14$ and $\sigma_{\mathrm{diag}} = 0.14$ to quantify orthonormality are slightly larger compared to the $10\,\%$ error in Section 4.4.2. This might be due to the additional challenge of measurement on the small nanoelements, due to which small vibrations and drifts can have a significant effect. Deviations between experiment and theory will again be due to measurement uncertainty and nonperfect encoding on the SLM.
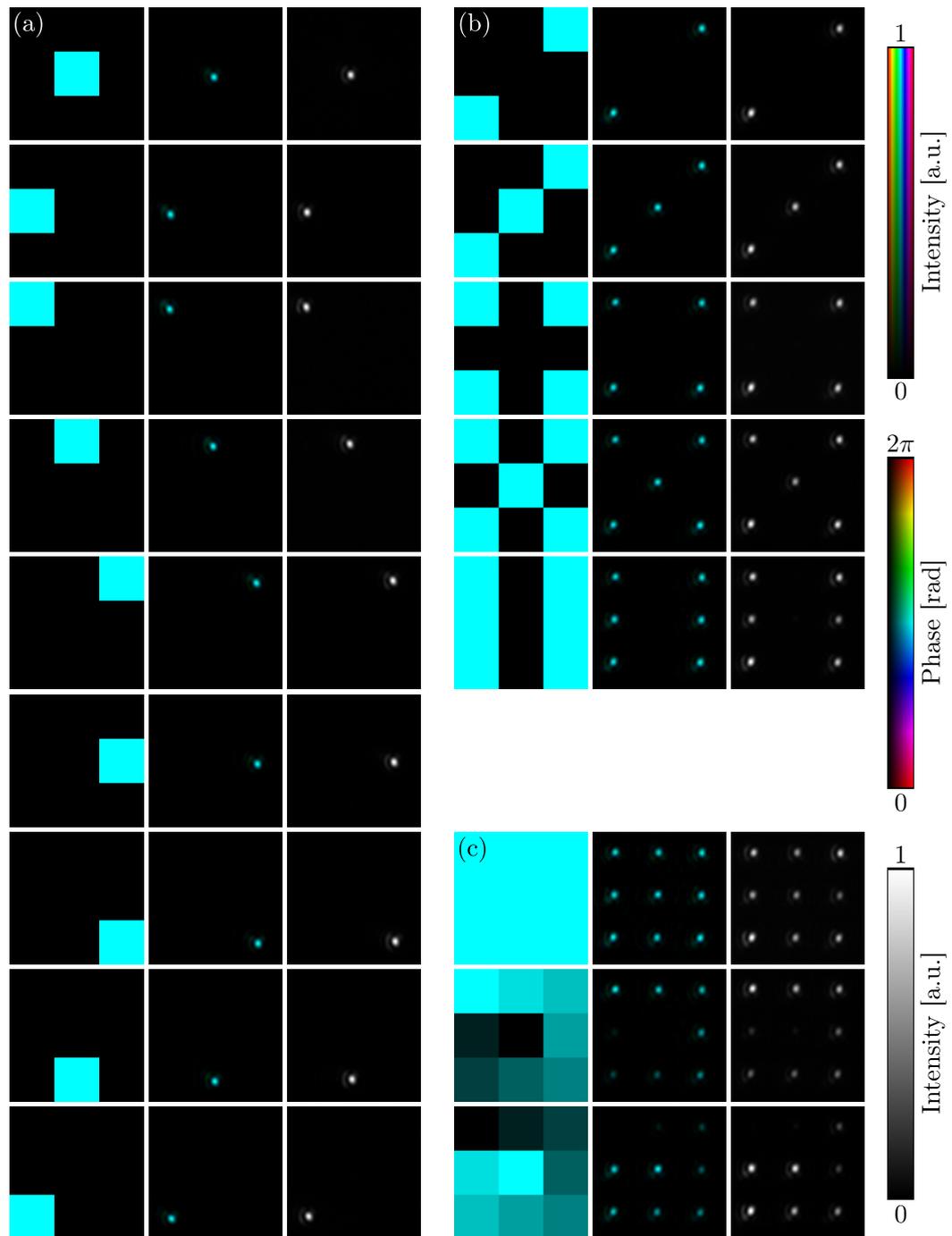
Figure 5.7: (a) Addressing single antennas. (b) Sides of dyes. (c) Addressing all antennas uniformly and with spiraling intensity gradient.

5.3.3 Approximation of target functions

Once the OEi $\mathbb{F}_k$ are determined for a set of selected points P_m on the sample, their superposition can be tailored to match user defined target functions. The principle of this procedure has been outlined in Section 5.1.2. This part provides some experimental examples of it, starting with the subset of 3×3 nanoantennas which was already used in Section 5.3.1 and is illustrated in Figures 5.3 and 5.4. The term "target function" means that a value of intensity and phase is assigned to each point P_m. This is shown in the left column of Figure 5.7a: Each element of the 3×3 matrix contains the intensity and phase information for one point P_m. From top to bottom of the figure the target intensity is moved around from one point to another. Projecting the OEi $\mathbb{F}_k$ onto the target values, as defined in Equation 5.3, delivers the superposition coefficient c_k for each mode. The semi-theoretical superposition T of the OEi according to Equation 5.5 is depicted in the middle column of Figure 5.7a. As demanded by the target values in the left column, the intensity in the middle column moves over the "theoretical" positions of the antennas. To show that the light is really directed to the correct locations on the structure, the superposition S following Equation 5.4 is encoded on the SLM. The resulting intensity distributions on the antennas are captured with the CCD and displayed in the right column of Figure 5.7a. The agreement between the images in the middle and right column shows that the light is indeed directed exactly onto the antennas, hence demonstrating the basic functionality of OEi based coherent control.

Further then this basic functionality it is possible to generate more complex light fields on the nanostructure. In Figure 5.7b not only one, but two to six antennas are excited simultaniously in patterns arranged like the points on a die. It is also no requirement to assign the same intensity to the addressed antennas. Figure 5.7c depicts target functions in which all 9 antennas are addressed uniformly and with a spiraling intensity gradient. The uniform highlighting of all 9 antennas is additionally illustrated with simultanious white light illumination in Figure 5.8. This again visually demonstrates the accurate directivity of the light field on the anntenna array.

One would expect that generating the appropriate light field gets increasingly more difficult with a rising number of degrees of freedom, i.e. addressed nanoelements/points, on the sample. This is investigated with an array of 7×7 nanopads that are arranged with a period of $800 \, \text{nm}$. This distance corresponds about to the wavelength $\lambda = 785 \, \text{nm}$ of the laser light. Figure 5.9 shows encoding the letters and numbers for a "St Andrews 600 Years" banner as well as some other target functions on this nanopattern. There is still good agreement between the semi-theoretical superposition of the OEi, depicted in the upper rows, and the experimentally resulting intensity distributions in the lower rows. However, it is clearly visible that in the experimental pictures not all points are addressed with
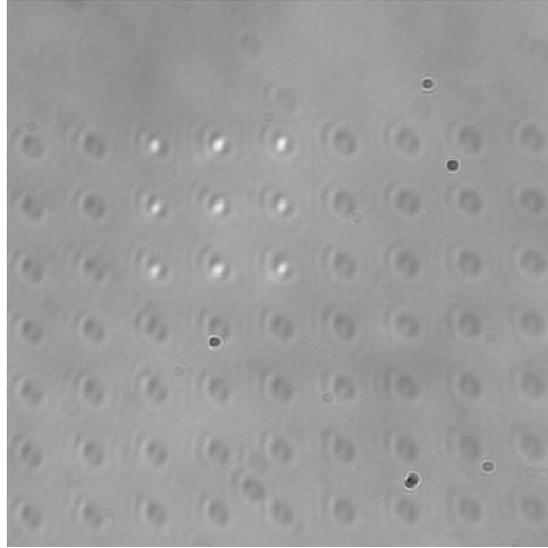
Figure 5.8: Highlighting a subset of 3×3 elements in an array of nanoantennas. The antennas are addressed from below with the OEi shaped laser beam and illuminated from above with whitelight. With respect to the reflected near infrared laser light the antennas are in focus. In the visible whitelight they are slightly out of focus due to the difference in wavelength.

identical intensity, though they are supposed to be. Investigating this behaviour in more detail is subject of the next Section 5.3.4.

5.3.4 Accuracy of target function approximation

In the previous Section 5.3.3 it was observed that with an increasing number of addressed nanoelements the experimentally generated intensity distributions visibly differ from the defined target functions. Here this effect is quantitatively analysed on the 800 nm spaced 7×7 nanopads. Therefore different numbers N_P of nanopads are addressed and the resulting intensity pattern is captured with the CCD camera. Then the deviation σ_t of this pattern from the target intensity distribution is calculated according to

$$\sigma_t = \bar{I}_t \sqrt{\frac{1}{M} \sum_{m=1}^{M} \left(\frac{I_{t,m}}{\bar{I}_t} - \frac{I_{c,m}}{\bar{I}_c} \right)^2}. \tag{5.7}$$

In Equation 5.7 the sum is over the total number $M = 49$ of nanopads/points on the sample and $I_{t,m}$ and $I_{c,m}$ are the target and captured intensities on the nanopad indexed with m. The latter are normalised to the mean intensities $\bar{I}_t$ and $\bar{I}_c$ on all points of the target function and the captured intensity image. To get
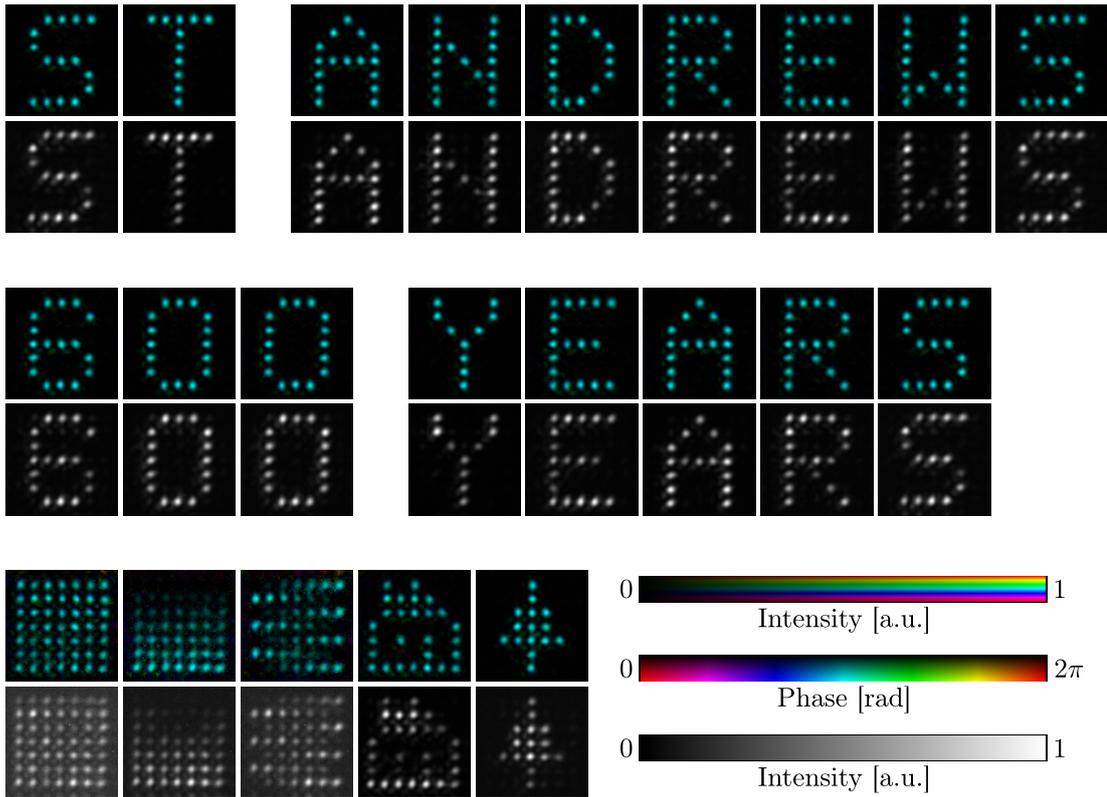
Figure 5.9: Generation of target functions on a subset of 7×7 nanopads spaced by 800 nm. The top row of each block in turquoise colour depicts the theoretical target functions, while the experimentally captured intensity distributions are illustrated as grayscale images.

some statistics, for each number N_P of addressed elements the deviation σ_t from the target function was measured 10 times for random selection of the elements. Figure 5.10a exemplarily shows some random target functions for various numbers N_P of addressed nanopads. The corresponding experimentally captured images are depicted in Figure 5.10b, clearly showing that with increasing number N_P of addressed points they are not uniformly illuminated anymore.

Figure 5.11 illustrates this inhomogeneity quantitatively in the form of σ_t, determined according to Equation 5.7, depending on N_P. The errorbars correspond to the standard deviation from the mean of the 10 randomised measurements. With increasing number N_P of addressed pads the deviation σ_t is increasing. This deviation between theory and experiment is due to a combination of measurement errors adding up and, probably mostly, due to nonperfect beam shaping by the SLM. That is why usually iterative algorithms with feedback are used to implement specified target functions, in particular multispot patterns [148, 204–209]. Thus, to generate challenging multispot patterns, a possible approach could be to use the OEi generated function as a good initial condition and then perform

0 ▭ 1
Intensity [a.u.]

0 ▭ 2π
Phase [rad]

0 ▭ 1
Intensity [a.u.]
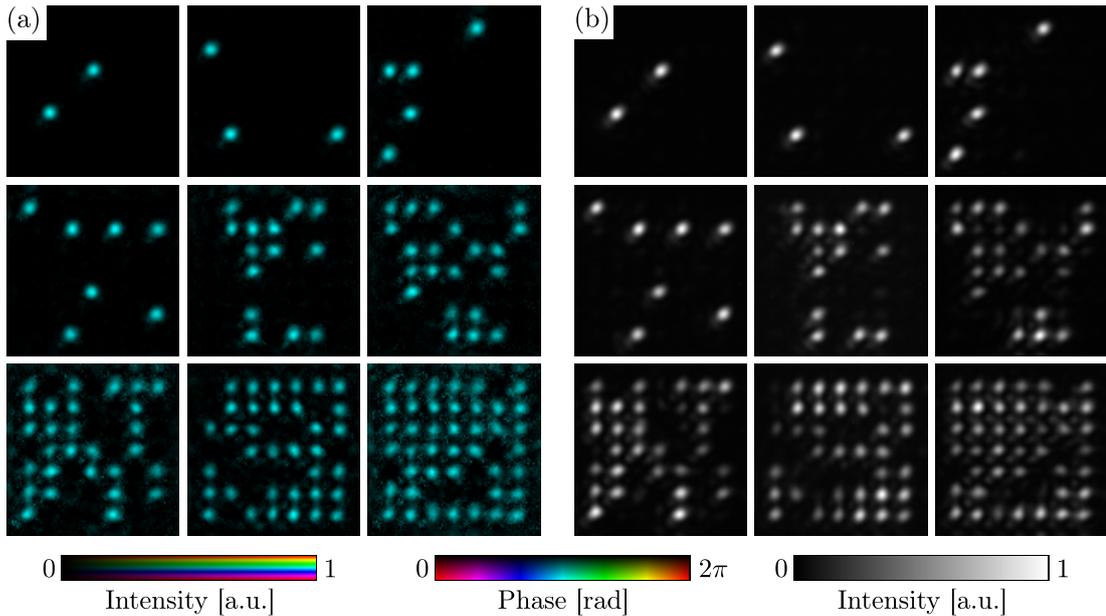
Figure 5.10: Addressing of different numbers N_P of nanopads at randomly chosen positions. (a) Theoretical target functions and (b) experimentally acquired intensity distributions.

finetuning with an iterative algorithm. However, for small numbers of spots the resulting intensity patterns agree quite well with the targets. Hence, in the next Section 5.3.5 the light field on a subset of 9 nanopads is decomposed into OEi with the aim of minimising illumination crosstalk.

5.3.5 Cross talk

One challenge for the control of the light field on a nanostructure is crosstalk between neighbouring elements. The term "crosstalk" in this context means the following: One attempts to optically address one element of the structure, but as a byproduct another element next to the target element is excited as well. This crosstalk can be due to two scenarios (or of course a mix of them). The first one is that one element of the structure is excited, e.g. by a tighly focussed laser beam, which is only illuminating that target element. However, the evanescent field of the illuminated element can couple to another element very close to the first one and excite that one as well. This process is called "evanescent coupling" and for it to happen two elements usually have to feature a gap of only few tens of nanometers, like two arms of a nanoantenna. The second scenario is that one attempts to focus a laser beam onto one element, but the focussing is not tight enough so that part of the beam illuminates neighbouring elements. This effect is here referred to as "illumination crosstalk".
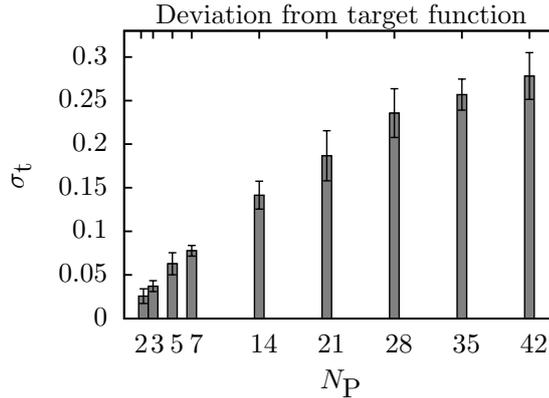
**Figure 5.11:** Deviation σ_t from target function depending on number N_P of addressed nanopads, calculated according to Equation 5.7.

As a near field effect, evanescent coupling is not necessarily visible in the far field. However, the experimental configuration used here detects in the far field. Thus this work deals with illumination crosstalk as a first and, with the available equipment, more sensible choice. To avoid evanescent coupling to happen, the structures that are used here are seperated by few hundred nanometers. The gap between the arms of the nanoantennas utlised earlier on would in principle allow evanescent coupling effects. But one antenna pair, with a size of about 300 nm, can only be addressed as a single point-like element with conventional far field optics, as the diffraction limit of the employed setup is about that value. So every observed crosstalk in the experiments should be due to inaccurate illumination and not due to plasmonic coupling.

The goal in this section is to investigate, whether or not the decomposition of the light field into orthogonal modes enables the tailoring of a more precise illumination that reduces crosstalk compared to illumination with a simple focused beam. Therefore the elements of an arrangement of nanoscatterers are illuminated individually using three different approaches:

1. Illumination with a focussed Gaussian beam;

2. Illumination using the first OEi with respect to the illuminated pad;

3. Illumination utilising a superposition of OEi that are orthogonal with respect to all 9 pads.

These three methods are outlined more detailed in the following.

Method 1: Focussed Gaussian beam This can be considered to be the most basic concept for the coherent control of individual nanoelements. In a first step the displacement of the beam on the sample is, in analogy to Section 3.5.1.1,
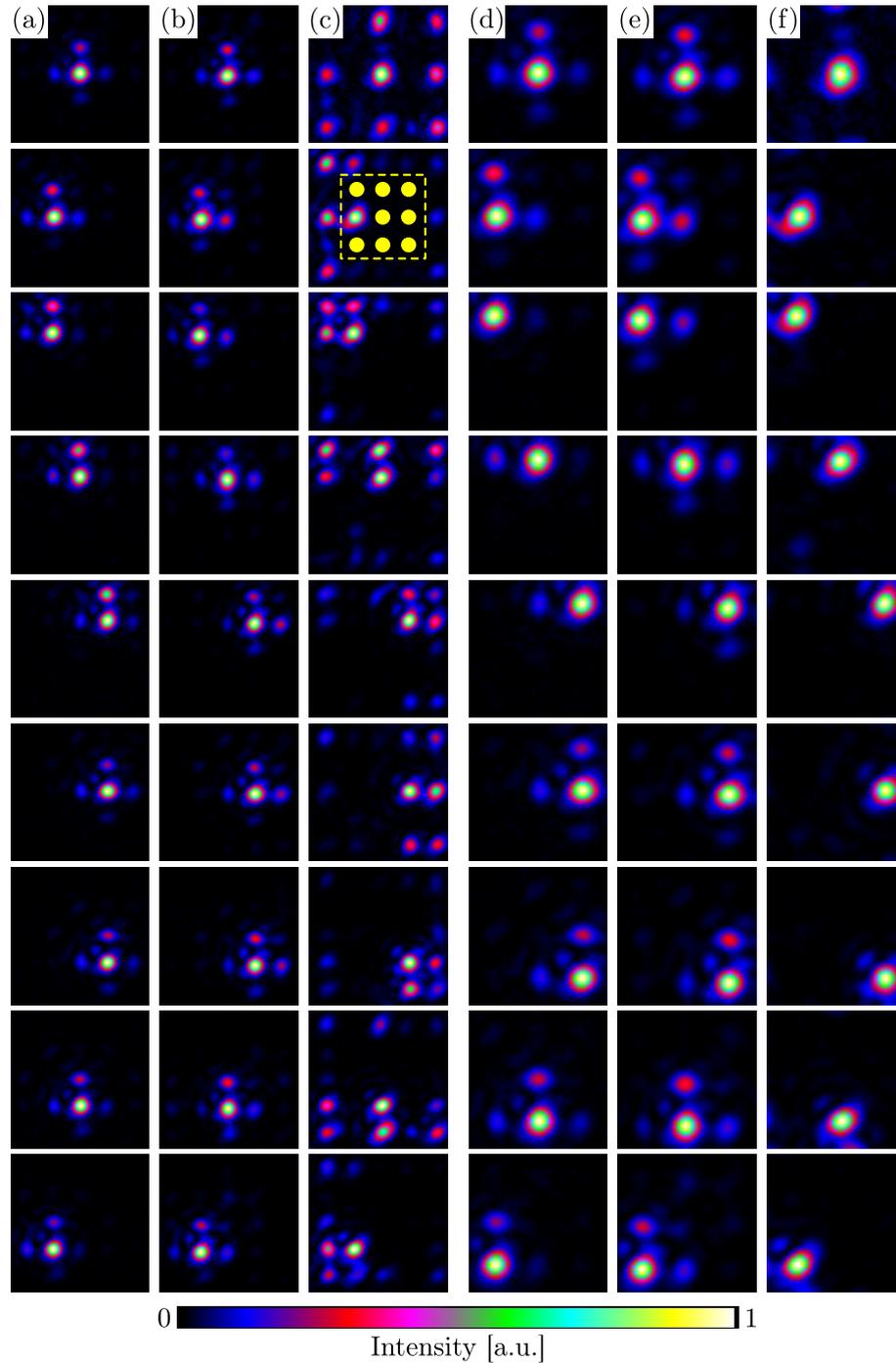
Figure 5.12: Addressing of single elements in a 3×3 array of $800\,\text{nm}$ spaced nanopads using (a) Method 1, (b) Method 2, and (c) Method 3. Columns (a), (b), and (c) depict intensity distributions on a 5×5 subset. Columns (d), (e), and (f) show only the central 9 pads, which were subject to the eigenmode decomposition. Their location with respect to (a), (b), and (c) is indicated in the second picture of column (c).

Semi-theory
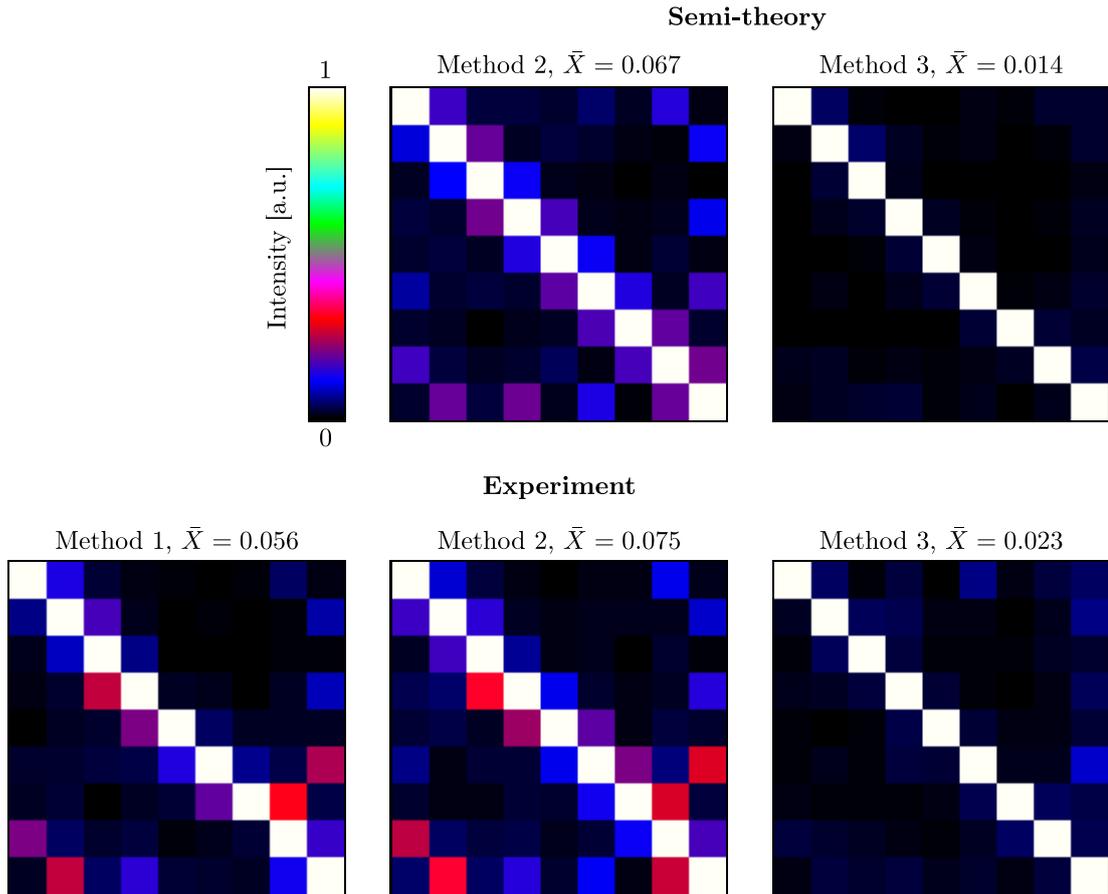
Figure 5.13: Crosstalk matrices for coherent control of $300\,\mathrm{nm}$ sized and $800\,\mathrm{nm}$ spaced goldpads using Methods 1, 2, and 3 for illumination.

calibrated depending on the deflections k_x, k_y on the SLM. Then the beam can be deflected to the position x_2, y_2 of the nanopad one wants to address by applying the proper k_x, k_y. As the SLM is wavefront corrected, the focus on the sample should be of about diffraction limited size.

Method 2: First OEi with respect to illuminated pad   For this method the sample is probed with the test fields F_i and they are superimposed in order to form the first OEi $\mathbb{F}_1$ with respect to the nanopad that shall be addressed. Generated from the eigenvector with the largest eigenvalue of the intensity operator, the mode $\mathbb{F}_1$ maximises the intensity on the addressed pad. Hence this illumination method is almost identical to the focussed beam. It should in principle just additionally compensate for small residual aberrations in the system, e.g. induced by the glass slide the nanostructure is fabricated on.

Method 3: Superposition of OEi The third method shares with the second one that the sample is probed with the test fields F_i. Different is then that OEi are calculated with respect to all nine nanopads and not only for one of them. To address an individual pad, the nine modes are superimposed in order to match a target function that directs the light to the selected pad. This process of approximating target functions was described in Section 5.1.2. As the OEi are orthogonal with respect to the nine nanoelements, they should constructively interfere only on the one element that one wants to excite and cancel out on all other elements.

In the following the above approaches are applied to a 3×3 subset of 800 nm spaced nanopads. In order to observe illumination crosstalk at this distance with a focussed beam, the effective NA for the illumination is decreased to about 0.4 by a suitable circular mask on the SLM. With this, the FWHM of the diffraction limited beam at the wavelength of 785 nm is about 1 μm, rendering Gaussian beam illumination of one pad without partly illuminating its neighbours impossible. To investigate this and a possible advantage of OEi illumination, the nanopads are addressed with the three Methods 1, 2, and 3. For Methods 2 and 3, the probing was performed using the first 60 "test modes". The results of the three methods are shown in Figure 5.12. Figures 5.12a, 5.12b, and 5.12c depict an area containing 5×5 nanopads. Out of these the central 3×3 pads are selected for optical addressing. Their positions are schematically indicated by yellow disks in the second picture of Figure 5.12c. From top to bottom, each picture of a subfigure corresponds to addressing another of the 9 nanopads. In Figure 5.12a the pads are illuminated with Method 1. The pad of choice is always clearly highlighted, but significant intensity is also deposited on the neighbouring pads. For Method 2, illustrated in Figure 5.12b, the result is almost identical, which is to be expected. The illumination with Method 3 is depicted in Figure 5.12c. Here the addressed pad is excited with no visible crosstalk on the other 8 pads, which are part of the arrangement the OEi are composed on. However, one will have noticed that instead intensity is dumped on pads that are not part of this square 3×3 pad arrangement, which will be discussed later on. For a closer view on the difference between the three methods, Figures 5.12d to 5.12f show the area of the inner 3×3 pads only, indicated by the dotted box in the second image of Figure 5.12c. In Figures 5.12d and 5.12e, corresponding to Methods 1 and 2, the pads next to the addressed one are obviously partly illuminated as well. In contrast to that, using Method 3 in Figure 5.12f, the intensity is clearly confined to the target pad only. Actually, in some of the pictures the shape of the confinement reflects the shape of the box, over which the intensity is average (see Figure 5.3c).

Quantitavely, the crosstalk for the three methods is illustrated in Figure 5.13 in the form of crosstalk matrices. The row and column indices of the matrices correspond to the indices m of the goldpads. In each column of a matrix another nanopad is addressed and the elements of a column depict the intensity on the

individual pads, normalised to the intensity on the target pad. The off-diagonal entries correspond to the crosstalk, i.e. the intensity on all other then the addressed pad. So in an ideal situation one would get the identity matrix with zero crosstalk. The average crosstalk $\bar{X}$ for a method is calculated as mean value of all off-diagonal matrix elements. For Methods 2 and 3, semi-theoretical crosstalk data is available via numerical superposition of the OEi. It is displayed in the top row of Figure 5.13 and suggests from $\bar{X} = 6.7\,\%$ to $\bar{X} = 1.4\,\%$ by $80\,\%$ reduced crosstalk using Method 3 compared to Method 2. This difference is also clearly visible in the matrices, where all off-diagonal elements are close to zero for Method 3, while significant off-diagonal contributions are present for Method 2. On the directly neighbouring elements the maximum crosstalk of about $25\,\%$ for Method 2 is reduced by more than $60\,\%$ to less than $10\,\%$ using Method 3. The experimental data in the bottom row of Figure 5.13 is in good agreement with the semi-theoretical prediction. Compared to Method 2, Method 3 offers from $7.5\,\%$ to $2.3\,\%$ by $70\,\%$ reduced crosstalk and in comparison to Method 1 the crosstalk is reduced from $5.6\,\%$ by $60\,\%$ using Method 3. On neighbouring antennas the maximum crosstalk is up to $35\,\%$ for Methods 1 and 2, while only $10\,\%$ are measured with Method 3. The latter corresponds to a decrease of about $70\,\%$.

On a smaller scale of about half the wavelength, the above study was carried out with a sample of $200\,\mathrm{nm}$ pads spaced with a period of $400\,\mathrm{nm}$. In this case the NA for illumination was restricted to about 0.8 on the SLM in order to observe crosstalk with a Gaussian focus. Figures 5.14a to 5.14c depict the addressing of the 9 nanopads with the Methods 1 to 3. Compared to Figures 5.14a and 5.14b, the illumination in Figure 5.14c visually looks tighter confined to the target pad, thus indicating a reduced crosstalk with Method 3 over Methods 1 and 2. This visual impression is confirmed quantitatively by the crosstalk matrices in Figure 5.14d. Experimentally, Method 3 delivers an average crosstalk $\bar{X}$ reduced by about $40\,\%$ compared to Method 1. In comparison to Method 2, the crosstalk is decreased by $55\,\%$. As for the $800\,\mathrm{nm}$ spaced pads, the experimental results are in reasonable agreement with the semi-theoretical predictions.

Interestingly, the price which has to be paid for the reduced crosstalk with Method 3 is that intensity is deposited on nanopads which are not included in the OEi decomposition. This is apparent in Figure 5.12c, in which nanopads outside the dashed yellow box are illuminated, while inside the box all light is confined to the target pad. The explanation for this effect is related to the squeezing of light in Chapter 3. As investigated there and elsewhere before [116–119], light cannot be focussed below the diffraction limit, at least not without intensity being pushed into the sidelobes of the spot. However, this is exactly what is required in order to minimise crosstalk on the nanopad array: The NA used to illuminate the nanopads is to low to focus the light tight enough for addressing an isolated element. That is why there is crosstalk using Methods 1 and 2 for illumination. With these approaches the light is simply directed to one pad of

(a)

(b)

(c)

(d)

Semi-theory

Method 2, $\bar{X} = 0.088$

Method 3, $\bar{X} = 0.028$

Intensity [a.u.]

1

0

Experiment

Method 1, $\bar{X} = 0.079$

Method 2, $\bar{X} = 0.11$

Method 3, $\bar{X} = 0.049$
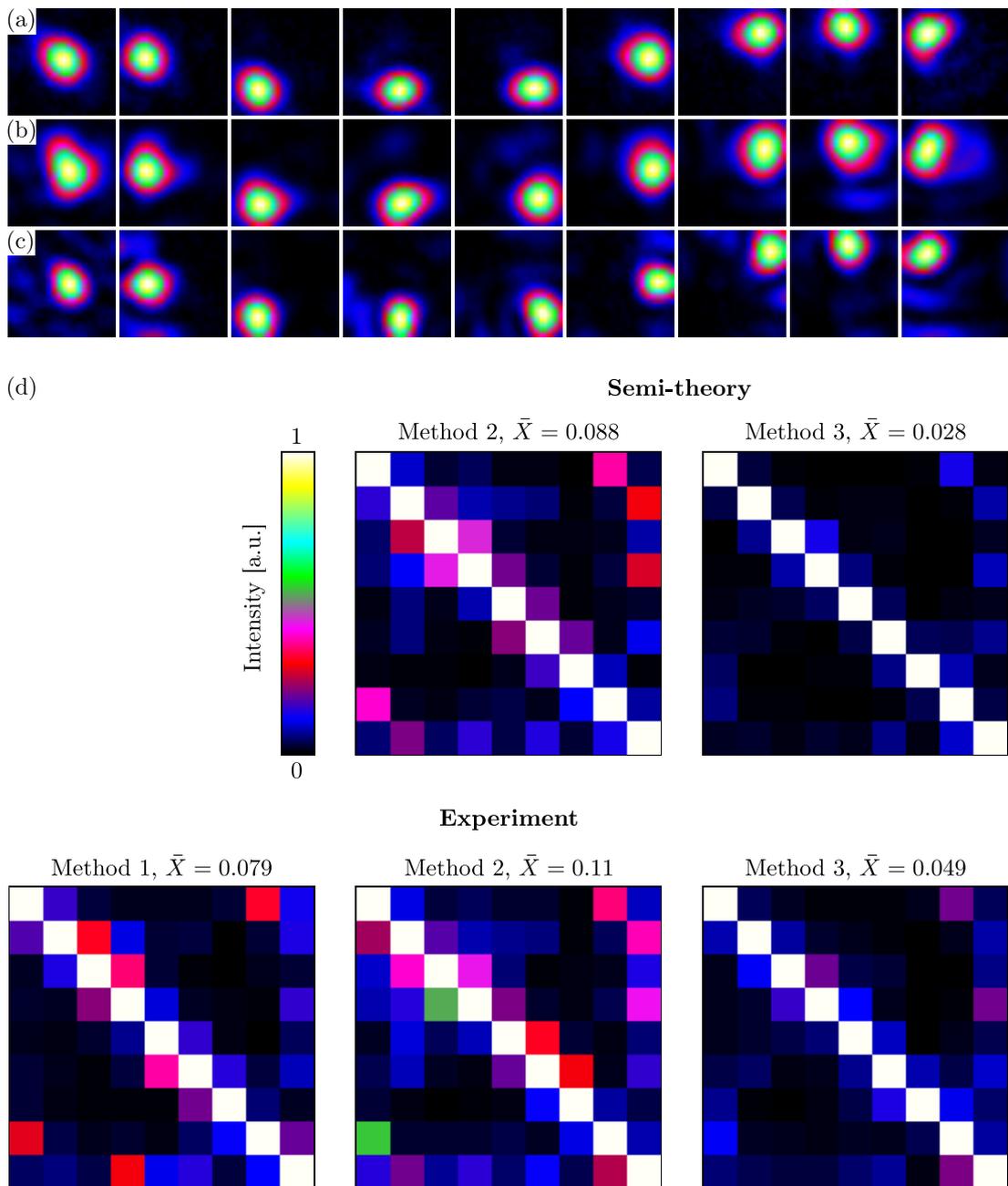
Figure 5.14: Illumination of $400\,\text{nm}$ spaced and $200\,\text{nm}$ sized goldpads with (a) Method 1, (b) Method 2, and (c) Method 3. (d) Crosstalk for the three methods.
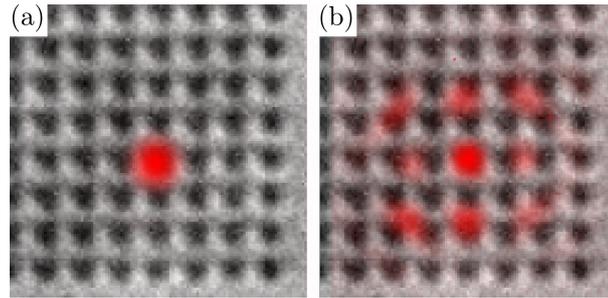
Figure 5.15: Graphical superposition of a whitelight image of the nanopad array and the intensity distributions of (a) the Gaussian focus and (b) the optical eigenmode beam to address the central of the 3×3 nanopads. The normal focus is visibly larger compared to the central bit of the OEi beam. To enable the reduced spot size of the latter, intensity has to be redistributed onto surrounding pads, which are not part of the optical eigenmode decomposition.

choice, without taking into account the other 8 pads. Using Method 3, the light field is first decomposed into orthogonal modes on all 9 pads of interest. Then the superposition of the modes is tailored to match a target function with high intensity on the addressed pad and zero intensity on the other ones. The difference to Methods 1 and 2 is that Method 3 directs the light onto the pad of choice, but with the additional constraint of minimising the intensity on the other 8 elements. This latter constraint requires to locally squeeze the illumination below the diffraction limit. And for this to happen intensity has to be dumped outside the region within which orthogonality is enforced by the eigenmode decomposition. For illustration of this effect, Figures 5.15a and 5.15b show the focussed Gaussian beam and the OEi beam used for illumination of the central of the 9 nanopads. The intensity distributions of both beams were captured on a big marker of the sample, effectively acting as a mirror. In both images the laser light, indicated by red colour, is superimposed onto a whitelight image of the nanopad array by graphical postprocessing. This enables a rough comparison of the spot sizes with respect to the nanostructure. The Gaussian beam has a measured FWHM of about 1000 nm and is partly extending onto neighbouring pads. On the other hand, the OEi beam visually seems to be tighter confined to the central goldpad. This impression is confirmed by a FWHM measure of about 800 nm. Hence, in the OEi beam generated by Method 3 the light is squeezed about 20 % below the diffraction limit, which is represented by the width of the Gaussian beam. As an unavoidable byproduct light is dumped outside the 3×3 antenna region as illustrated in Figure 5.15b. The question is: What are the limitations of this approach, i.e. how far could the NA be reduced while still maintaining the ability to individually address the nanoelements? Or, equivalently, how closely packed can the nanoelements be arranged while still controlling them individually? The answer is identical to the question of how far a focal spot can be squeezed: It
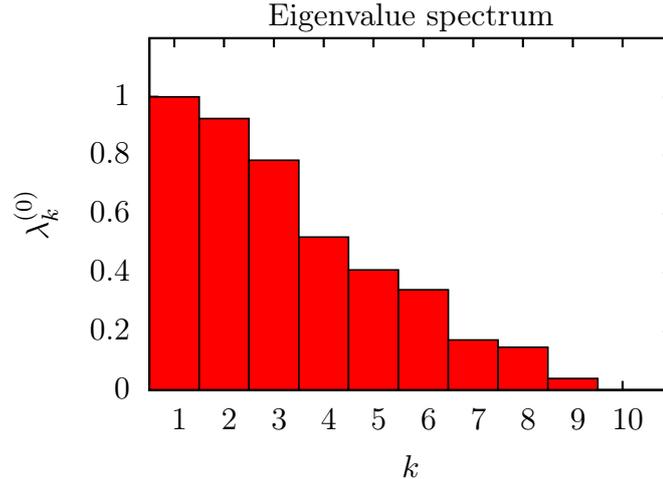
Figure 5.16: Eigenvalue spectrum for the 800 nm spaced nanopads and the NA reduced to 0.4.

depends on the noise level and the number of degrees of freedom/OEi above the noise as well as the size of the area within which the nanopads shall be addressed. As long as, for the example of the 9 nanopads, there are 9 OEi with significant eigenvalues, the OEi can be superimposed in order to address the nanopads seperately. For the NA of 0.4, the lowest eigenvalues are already close to zero, as can be seen in the plot of the eigenvalue spectrum in Figure 5.16. For comparison: In Figure 5.5 all eigenvalues are clearly above zero, until a sharp drop when k gets larger than the number of nanoelements. In Figure 5.16 there is no such sharp gap, instead the $\lambda_k^{(0)}$ converge towards zero. If the NA is further reduced below 0.4 or, at constant NA, the pads are moved closer together, it will at some point no longer be possible to find 9 orthogonal modes above the noise level. And this is the point where the individual addressing will fail.

5.4 Correction through diffusive media

Another advantage of experimentally decomposing the focal field into optical eigenmodes besides their orthogonality is, that they also incorporate optical aberrations for the chosen field of view or, in the case presented here, with respect to the chosen nanoelements. From that point of view OEi are similar to transmission eigenchannels of a diffuse medium [210, 211]. With the ability of flexible light shaping by SLMs for aberration correction, scattering media have shown to not necessarily be a disturbing factor. Their presence can also be taken as an advantage, e.g. to focus light into a smaller spot [212, 213]. Common wavefront correction methods correct for aberrations with respect to one point. This point
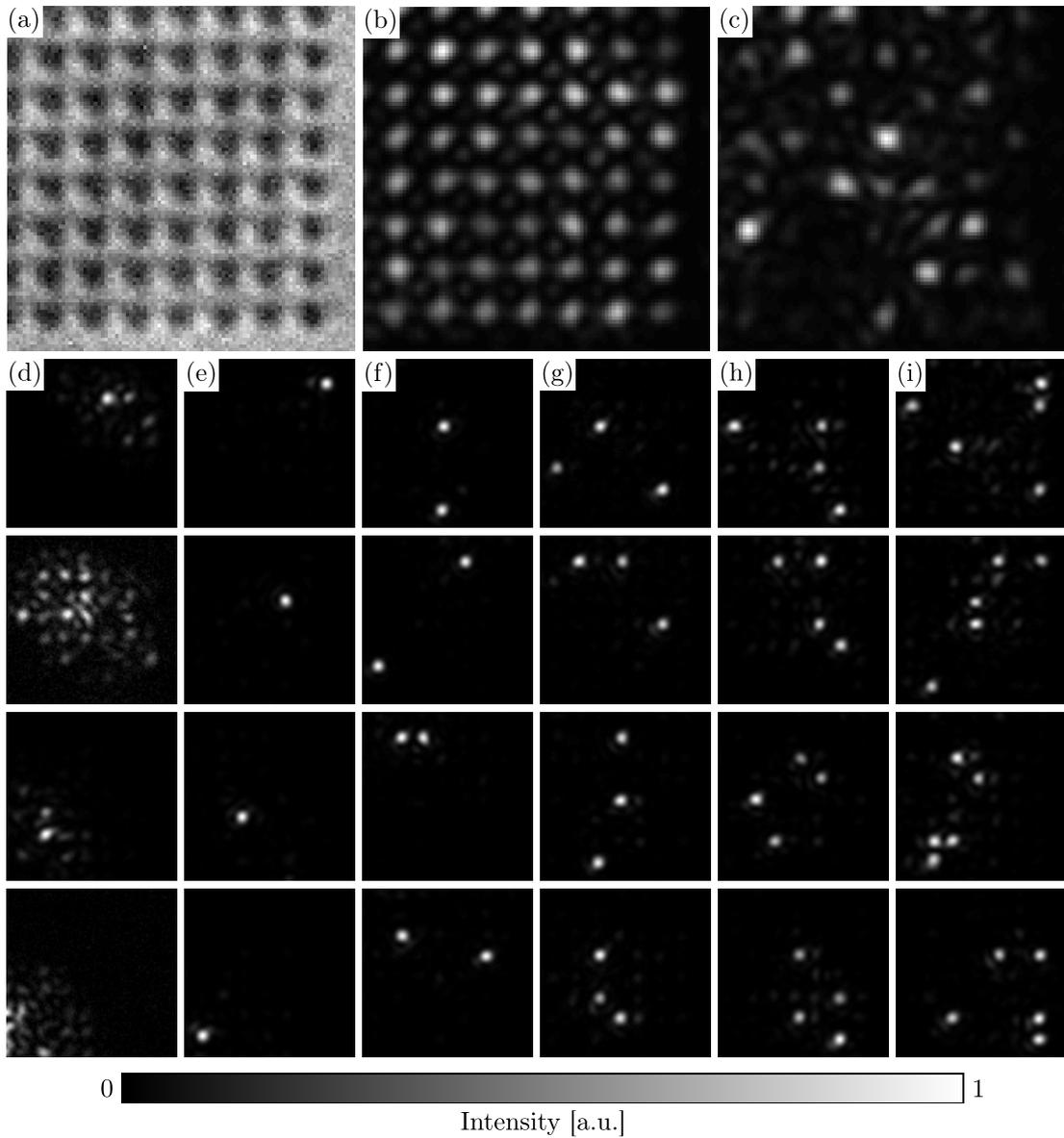
Figure 5.17: (a) Whiltelight image of the 7×7 subset of $300\,\text{nm}$ nanopads with $800\,\text{nm}$ spacing. (b) Illumination of this subset with the reference beam. (c) The same as (b), but with the diffuser distorting the wavefront. (d) Attempt to address nanopads on the diagonal of the array. (e) Same as (d) but with the wavefront corrected due to the superposition of optical eigenmodes. (f)-(i) Focusing onto two to five randomly chosen nanopads.

can be just an area of choice on a CCD camera [214, 215] or a so called "guide star", such as an isolated fluorescing or scattering particle [147, 213]. Then the SLM is divided into segments and the phase of each of the segments is cycled iteratively, such that it is in phase with all other segments at the reference point. In order to correct with respect to several points, they have to be chosen in advance and their intensity sum is used as a feedback to distribute intensity equally amongst them [215].

Using the OEi method, it is possible to determine modes with respect to the chosen field of view or to chosen points, automatically taking aberrations by a diffusive medium into account. Once the OEi are known, their superposition can be tailored to match a target function. Encoding the corresponding complex field on the SLM then generates this target function through the scattering medium. This is demonstrated here. Therefore a holographic diffuser (1° diffusing angle, Edmund Optics) is positioned about 1 cm after the iris in the setup shown in Figure 5.1. The diffused laser light is used to illuminate the subset of 7×7 nanopads, already used for the experiments in Section 5.3. For orientation, Figure 5.17a depicts a whitelight image of this arrangement. Upon illumination with the reference beam and without the diffuser in place, the nanopads are relatively homogenously illuminated, as shown in Figure 5.17b. With the diffuser in place, the illmination is heavily distorted, illustrated in Figure 5.17c. Consequently, a controlled addressing of individual antennas is impossible. Exemplarily, Figure 5.17d shows the attempt of illuminating every second element on the diagonal from the top right to the lower left corner of the nanopad array. To compensate for the aberrations, OEi are determined with respect to the array elements in the same way as in Section 5.3. Literally, the only difference to the prior experiments in Section 5.3 is the diffuser in the optical path. Now that the optical eigenmodes are known, the diagonal nanopads can be addressed properly, as depicted in Figure 5.17e. This already demonstrates the flexibility given by the OEi method: No new probing is necessary to deflect the beam onto nanoelements at different locations, as aberration correction for the whole field of view is inherent to the OEi. But further than this, also more than one element can be addressed simultaniously by defining appropriate target functions, onto which the OEi are then projected. Figures 5.17f to 5.17i illustrate the simultanious focusing onto two to five nanopads at randomly chosen positions, further underlining the full field wavefront correction.

In conclusion the results in this section demonstrate, that a full field aberration correction is inherent to experimentally determined OEi. This is a very useful feature when working in turbid media such as biological tissues and cells.

5.5 Summary

This section provides a summary of the main results and conclusions obtained throughout this chapter and finishs with an outlook onto possible future work. After describing the basic principle of optical eigenmode based coherent control, the experimental implementation was described. As a first experiment it was shown, how the field on a 3×3 nanoantenna array is decomposed into OEi. Here the method delivered exactly 9 eigenmodes with nonzero eigenvalues, i.e. nonzeros intensity on the antennas. Good agreement was observed between the numerically calculated intensity distribution of these modes and the experimentally captured distributions. As a next step the orthonormality of the experimental modes was checked on 3×3 nanopads. The OEi were found to be orthonormal in good approximation.

Knowing the OEi, they could be superimposed to match user defined target functions. The basic functionality of this concept was demonstrated on the 3×3 nanoantenna array, addressing one or more antennas with identical intensity or with an intensity gradient. Here the experimental realisation of the target functions was agreeing well with the defined target. A 7×7 nanopad array could be addressed with more challenging light patterns, such as letters and numbers. In that case a deviation between the defined target and the experimentally generated intensity distribution was observed, which was increasing with increasing number of addressed nanoelements. It was concluded that this discrepance is mainly due to the encoding on the SLM, which is why usually iterative algorithms are used to generate e.g. multispot patterns. As a possible improvement it was proposed to use an eigenmode generated function as a good initial condition and finetune the light pattern using iterative algorithms.

However, for small numbers of elements, such as 9 nanopads, the error in target function reproduction was below 10%. Hence, using a subset of 3×3 pads, it was investigated if individual elements could be addressed with reduced illmination crosstalk compared to addressing with a focused Gaussian beam. With an illumination NA of 0.4, the diffraction limited beam was featuring a FWHM of about $1\,\mu m$. On the $300\,nm$ sized pads with $800\,nm$ spacing this was leading to a maximum illmination crosstalk of up to 35% and an average crosstalk of 6% on the whole subarray. Using optical eigenmodes, both the maximum and the average crosstalk could be reduced by 60-70\% to about 10% and 2% respectively. On a smaller scale of half the wavelength, optical eigenmodes helped to reduce the crosstalk by about 50% on $400\,nm$ spaced nanopads of $200\,nm$ diameter.

Finally, it was shown that full field aberration correction is inherent to experimentally determined OEi. Therefore eigenmodes were determined on the 7×7 subset of nanopads with a diffuser in the illumination part of the optical path. With these it was possible to address one or multiple nanopads through the diffuser, hence demonstrating the applicability of optical eigenmode based coherent

control in turbid environments. This can be of great advantage for biomedical sensing or imaging applications involving scattering cells and tissue for example.

In conclusion the results presented in this chapter demonstrated the advantage using optical eigenmodes for the coherent control of nanoelements. Compared to conventional addressing them with a Gaussian beam, optical eigenmodes can reduce the illumination crosstalk with neighbouring elements, hence having the potential of a higher spatial resolution for sensing or also imaging applications. Furthermore they incorporate a full-field wavefront correction, which might be useful for applications in biological samples. It has also been illustrated and discussed that the effect that minimises the crosstalk is a local squeezing of the beam, as in Chapter 3. To achieve that, light has to be redistributed elsewhere. In the case presented here it is on other nanopads, which were not part of the OEi decomposition. This redistribution is unavoidable in far field optics. Hence, for the future it would be interesting to investigate, if also the near field can be controlled with the OEi concept. The studies in this chapter were dealing with illumination crosstalk, but maybe also plasmonic crosstalk can be reduced by tailored illumination. Thereby the idea would be to minimse the effect of plasmonic coupling of a metallic nanolelement with its neighbours by shaping amplitude and phase of the illumination of both the element that one wants to address and the one that exhibits plasmonic crosstalk. The principle would be similar to active noise control [216, 217], as used e.g. in noise cancelling headphones. A practical implementation would require to record feedback in the near field of the nanostructures. This could be done for example by SNOM, two photon luminescence, or simply fluorescence.

Chapter 6

Summary, Conclusions & Outlook

This thesis dealt with the application of optical eigenmodes do minimise focal spots, perform compressive imaging, and coherently control the illumination of gold nanostructures. The introduction in Chapter 1 started with oscillations and made the transition to light as a wave. The general concept of modes was illustrated at the example of vibrations. In this context modal analysis is important for manufacturing music instruments or analysing resonances of for example car bodies and buildings such as bridges and skyscrapers. The benefit of decomposing oscillations into modes is, that an analysis can be carried out only taking into account the most important modes. As other applications of this compressive feature eigenfaces for face recognition and modal analysis to model motion in animations were highlighted. With respect to optics and photonics, the modal concept is well established in laser physics to characterise cavities and beams. In this thesis modal analysis has been applied to the focal plane of optical systems, decomposing it into optical eigenmodes.

The theory Chapter 2 dealt with light as a wave and numerical methods for its propagation and focussing. The diffraction limit resulting from the wave nature of light was briefly reviewed and degrees of freedom in an optical system were discussed. Then it was detailed, how the light field in the focal plane of an optical system is decomposed into its degrees of freedoms, i.e. into optical eigenmodes. Examples for modes with respect to a circular region in the focal plane of a lens and in a square in the focal plane of a microscope objective have been simulated.

The former were used in Chapter 3 to demonstrate, how the optical eigenmode concept can be employed to extremise certain measures of the light field. In the presented case the width of a focussed laser beam was minimised in simulations. The relationship between the spot size, its Strehl ratio, and the intensity and distance of the sidelobes compared to the central spot were in qualitative agreement with prior studies on that topic. While the theoretical possibility of locally squeezing a focal spot below the diffraction limit is known for several decades, only little is known about practical limits regarding their implementation. Using an SLM system to generate the focal spots enabled a comprehensive experimental

study to be carried out answering that question. It was found that with state-of-the-art beam shaping technology focal spots with up to 60 % reduced core size and Strehl ratios down to 0.004 could be generated. As a possible application example, pairs of holes were confocally scanned with a selected minimised beam and a resolution gain of 1.28 was observed according to the Rayleigh criterion. Applying the same spot in fluorescence imaging, a gain of about 1.45 was proposed based on simulations. However, as there are already imaging techniques such as STED, PALM/STORM, SIM, that deliver resolution gains of 2 or even up to an order of magnitude, it was concluded that the application of minimised focal spots is more beneficial for applications that physically require a small spot, such as lithography, data storage, or photoporation.

In Chapter 4 optical eigenmodes were used to perform indirect imaging. Therefore the modes are projected onto the sample and for each of them a complex coupling coefficient to the sample is determined. The superposition of the OEi with the corresponding coefficients then delivers an indirect image of the sample. After a review of other indirect imaging methods, in particular (computational) ghost imaging using speckle pattern projections, the principle of optical eigenmode imaging was detailed. Then OEi imaging was compared in simulations to computational ghost imaging. It was found that, using OEi, 2-3 orders of magnitude fewer probes are necessary to obtain an image of similar quality compared to conventional ghost imaging. In compressive computational ghost imaging schemes the acquired speckle patterns are represented in their most sparse basis set, which saves about an order of magnitude acquisitions. In that case OEi imaging is 1-2 orders of magnitude more efficient, as the optical eigenmodes represent the most sparse possible set of illumination patterns.

However, the imaging modality which is mostly used for spectral imaging is raster scanning. In that context relevant features are the resolution and the capability of localising sample features, both in dependence on the number of probes, i.e. scanning points. The simulations carried out showed that in theory, compared to raster scanning imaging, OEi imaging requires an order of magnitude less probes to obtain subdiffractive localisation of points on the object. Furthermore, four times less samplings are required to approach a diffraction limited resolution. But one has to keep in mind, that at least three intensity acquisitions are required to determine one complex OEi coupling coefficient, hence reducing the advantage of OEi imaging.

Before doing optical eigenmode imaging in praxis, the correct experimental implementation of the OEi was checked. The intensity distributions of the OEi, captured with a mirror in the focal plane, were in good agreement with the simulated ones. Furthermore, orthogonality of the eigenmodes was verfied to be fulfilled in good proximity. Both of these indicated a good practical implementation of the optical eigemodes. In a first transmission imaging experiment a test target featuring three holes was imaged. The resulting picture was agreeing with

simulations, hence confirming the practical functionality of OEi imaging. As first step to spectral imaging, one of the holes was covered with a thin layer of Blu-Tack, which was exhibiting some fluorescence. Based on that signal, the covered hole could be reconstructed, while an image of the other two holes was obtained based on the transmission signal.

To investigate the suitablity of OEi imaging with respect to Raman scattering, 3 µm diameter polystyrene and PMMA beads were chosen, as they provide a relatively strong Raman signal. Using only four modes, it was possible to reconstruct images of one and two polystyrene beads in a field of view of about 6 µm × 6 µm. With a polystyrene and a PMMA bead in the image area, each of them could be reconstructed seperately chosing the corresponding spectral range, hence demonstrating the suitablity of OEi for compressive hyperspectral imaging. As a drawback it was observed, that the projection of higher order modes did decrease the image quality. This was attributed to the beads as strongly aberrating sample. Their thickness of 3 µm equalled half of the field of view, hence they were acting like a 3D object. This induced severe changes in the phase of the OEi, affecting their correct reproduction in the focal plane. A focal spot used for raster scanning was not disturbed in such a strong way, as its intensity distribution does not rely with that sensitivity on a correct phase. A further challenge observed for OEi imaging are low focal intensities. As the OEi are filling the whole field of view, their energy density on the sample is low compared to a focussed beam. And as a further result of their fullfield illumination and their organisation by spatial frequencies is, that they only utilise a small fraction of the SLM in the reciprocal plane, which additionally lowers the intensity. As a result the Raman signal by smaller 1 µm sized beads was not sufficient for optical eigenmode imaging in the used configuration.

To get a strong Raman signal from a sample with few aberrations, advantage was taken of the SERS effect. In particular a sample consisting of dithiol sandwiched between a gold surface and 200 nm gold particles was used, which exhibited strong SERS hotspots at the positions of the latter. With this additional signal strength, OEi Raman imaging was performing very well and the use of higher order modes enabled to reveal fine sample features. The usage of 60 optical eigenmodes delivered a picture with a twofold increased lateral resolution and an order of magnitude higher S/N ratio compared to a rasterscan with 484 points.

Overall it was demonstrated that the principle of OEi imaging works in transmission, with fluorescence, and in the regime of Raman scattering. The fact that the sample illumination is decomposed into its degrees of freedom, ordered by their relevance, enables the most efficient probing of the sample possible. Due to that, images with a higher resolution can be obtained for the same number of probes compared to raster scanning. This advantage is greatest for a few number of probes; when the number of probes/scanning points is approaching the Nyquist limit, the advantage of OEi imaging tails off. Another strong feature of optical

eigenmode imaging is that, due to the phase information, the background signal is cancelled very efficiently. The challenges that were observed regarding OEi imaging are its sensitivity to aberrations induced by the sample and its low power density in the focal plane. The latter is especially problematic in low efficiency applications such as Raman imaging. As the most promising way to increase the OEi intensity on the sample it has been discussed to change the experimental setup such, that the SLM modulates the light in a confocal plane instead of a reciprocal plane. Like that the full SLM area would be used for each OEi. In future this might enable optical eigenmode imaging of samples with lower Raman cross sections, maybe even biological cells and tissues.

In the last Chapter 5 the coherent control of gold nanostructures with optical eigenmodes was investigated. First it was shown how the field on nanoelements could be decomposed into OEi. Good agreement was observed for the theoretical and experimental intensity distribution of modes on 9 nanoantennas and orthonormality was confirmed on 9 nanopads with the same method as in Chapter 4. Then it was demonstrated how OEi can be superimposed to generate target illumination patterns, e.g. to simultaniously illuminate several antennas with identical intensity or an intensity gradient. This worked well for about 10 nanoelements, but in general the discrepance between the target and the generated illumination was increasing with increasing complexity, i.e. number of elements. As a possible way to improve this it was discussed to use the OEi generated pattern as a good initial guess for finetuning by iterative algorithms, which are usually used to taylor feature-rich light fields.

On a 3×3 subset of nanopads spaced by a distance smaller than the diffraction limit, it was furthermore demonstrated, that the orthogonality of the OEi helps to prevent illumination crosstalk when adressing a single element. Compared to illumination with a focussed Gaussian beam, the crosstalk was reduced by up to $70\,\%$ using OEi shaped illumination.

Finally, by adressing nanopads through a diffuser, it has been shown that experimentally determined OEi incorporate a full-field aberration correction. This is a very useful feature when working in turbulent media such as biological tissues and cells.

With respect to the reduced crosstalk it was illustrated and discussed, that this reduction was also a local effect, similar to the squeezing of a focal spot in Chapter 3. To achieve the crosstalk reduction, it was also necessary to redistribute intensity elsewhere. In other words, this effect is ultimately also restricted by the far field diffraction limit. Hence, in future it would be interesting to investigate, if the concept of optical eigenmodes could be used to generate a far field illumination that optimises the near field. With respect to that it has been discussed to employ OEi in order to minimise not illumination, but plasmonic crosstalk.

Overall, this thesis has shown the application of optical eigenmodes to extremise properties of the light field, in this particular case minimising the width of a focal

spot. Furthermore, they were used to perform highly compressive hyperspectral imaging and for the coherent control of gold nanostructures. Advantages and challenges were highlighted and discussed and possible directions for the future have been pointed out. The most interesting of these seems to be the tailoring of plasmonic near field effects, which might be of great advantage for high resolution and sensitivity biomedical sensing applications.

Appendix A

Radial symmetric representation of Huygen's integral in ABCD system

Here it shown how the radial symmetric representation of Huygen's integral in Equation 2.16 with the $ABCD$ matrix optics formalism is derived. In one dimension the field $F(x_2)$ resulting from propagation of the field $E(x_1)$ through an optical system represented by an $ABCD$ matrix is calculated by [22]

$$F(x_2) = \sqrt{\frac{\mathrm{i}}{B\lambda}}\, \mathrm{e}^{-\mathrm{i}kL} \int_{-\infty}^{\infty} E(x_1) \exp\left[-\mathrm{i}\frac{k}{2B}\left(Ax_1^2 - 2x_1 x_2 + Dx_2^2\right)\right] dx_1. \quad (\text{A.1})$$

In Equation A.1 the wavelength is denoted by λ, $k = 2\pi/\lambda$, L is the overall distance of propagation, and A, B, and D are the elements of an $ABCD$ matrix. Extending Equation A.1 to two dimension results in

$$F(x_2, y_2) = \frac{\mathrm{i}}{B\lambda}\, \mathrm{e}^{-\mathrm{i}kL} \iint_{-\infty}^{\infty} E(x_1, y_2) \exp\left[-\mathrm{i}\frac{k}{2B}\left(Ax_1^2 - 2x_1 x_2 + Dx_2^2\right)\right] \times$$

$$\times \exp\left[-\mathrm{i}\frac{k}{2B}\left(Ay_1^2 - 2y_1 y_2 + Dy_2^2\right)\right] dx_1 dy_1. \quad (\text{A.2})$$

In polar coordinates $x = r\cos\varphi$ and $y = r\sin\varphi$, Equation A.2 becomes

$$F(r_2, \varphi_2) = \frac{\mathrm{i}}{B\lambda}\, \mathrm{e}^{-\mathrm{i}kL} \int_0^{\infty}\int_0^{2\pi} E(r_1, \varphi_1) \exp\left[-\mathrm{i}\frac{k}{2B}\left(Ar_1^2 + Dr_2^2\right)\right] \times$$

$$\times \underbrace{\exp\left[\mathrm{i}\frac{k}{B} r_1 r_2 \cos\left(\varphi_1 - \varphi_2\right)\right]}_{\zeta} r_1\, dr_1 d\varphi_1. \quad (\text{A.3})$$

With the relationship [218]

$$\int_0^{2\pi} \exp\left\{i\left[\frac{k}{B} r_1 r_2 \cos\left(\varphi_1 - \varphi_2\right) - \nu\varphi_1\right]\right\} d\varphi_1 = 2\pi\, i^\nu e^{-i\nu\varphi_2} J_\nu\left(\frac{kr_1 r_2}{B}\right) \quad \text{(A.4)}$$

and the field E being purely radial dependent, the factor indicated by ζ in Equation A.3 becomes 2π times the Bessel function J_0 of first kind and order 0. This finally delivers the radial symmetric representation of Huygen's integral using the $ABCD$ matrix formalism as

$$F(r_2) = i\frac{k}{B}\, e^{-ikL} \int_0^\infty E(r_1)\, \exp\left[-i\frac{k}{2B}\left(Ar_1^2 + Dr_2^2\right)\right] J_0\left(\frac{k}{B} r_1 r_2\right) r_1\, dr_1. \quad \text{(A.5)}$$

Bibliography

[1] K. A. RAMSEY: *Effective Measurements for Structural Dynamics Testing PART I.* Sound and Vibration Magazine, 11:24–35, 1975.

[2] X. HE and J. TROMP: *Normal-mode constraints on the structure of the Earth.* Journal of Geophysical Research, 101:20053–20082, 1996.

[3] M. SCHLESKE: *Eigenmodes of Vibration in the working process of a violin.* Catgut Acoustical Society Journal, 3:2–8, 1996.

[4] M. SCHLESKE: *Empirical Tools in Contemporary Violin Making: Part I. Analysis of Design, Materials, Varnish, and Normal Modes.* Catgut Acoustical Society Journal, 4:50–64, 2002.

[5] C. M. HUTCHINS: *The Acoustics of Violin Plates.* Scientific American, 245:170–179, 1981.

[6] M. J. WHELAN, M. V. GANGONE, K. D. JANOYAN, and R. JHA: *Operational modal analysis of a multi-span skew bridge using real-time wireless sensor networks.* Journal of Vibration and Control, 17:1952–1963, 2011.

[7] X. SHI and C. S. CAI: *Suppression of Vehicle-induced Bridge Vibration Using Tuned Mass Damper.* Journal of Vibration and Control, 14:1037–1054, 2008.

[8] S. I. KIM: *Experimental evaluations of track structure effects on dynamic properties of railway bridges.* Journal of Vibration and Control, 17:1817–1826, 2011.

[9] S. R. CHEN, C. C. CHANG, and C. S. CAI: *Study on Stability Improvement of Suspension Bridge with High-Sided Vehicles under Wind using Tuned-Liquid-Damper.* Journal of Vibration and Control, 14:711–730, 2008.

[10] R. A. KHAN and T. K. DATTA: *Probabilistic Risk Assessment of Fan Type Cable Stayed Bridges Against Earthquake Forces.* Journal of Vibration and Control, 16:779–799, 2010.

[11] F. AMINI and R. VAHDANI: *Fuzzy Optimal Control of Uncertain Dynamic Characteristics in Tall Buildings Subjected to Seismic Excitation.* Journal of Vibration and Control, 14:1843–1867, 2008.

[12] K. A. KORKMAZ, Z. AY, S. N. KESKIN, and D. CEDITOGLU: *Investigation of Traffic-induced Vibrations on Masonry Buildings in Turkey and Counter-measures.* Journal of Vibration and Control, 17:3–10, 2011.

[13] D. GREENA and W. G. UNRUH: *The failure of the Tacoma Bridge: A physical model.* American Journal of Physics, 74:706–716, 2006.

[14] L. SIROVICH and M. KIRBY: *Low-dimensional procedure for the characterization of human faces.* Journal of the Optical Society of America A, 4:519–524, 1987.

[15] M. TURK and A. PENTLAND: *Eigenfaces for Recognition.* Journal of Cognitive Neuroscience, 3:71–86, 1991.

[16] A. PENTLAND and J. WILLIAMS: *Good vibrations: modal dynamics for graphics and animation.* In *Proceedings of the 16th annual conference on Computer graphics and interactive techniques*, pages 215–222, 1989.

[17] R. FLOREA and K. C. HALL: *Eigenmode Analysis of Unsteady Flows about Airfoils.* Journal of Computational Physics, 147:568–593, 1998.

[18] K. K. HAUSER, C. SHEN, and J. F. O'BRIEN: *Interactive Deformation Using Modal Analysis with Constraints.* In *Proceedings of the Graphics Interface 2003 Conference*, pages 247–256, 2003.

[19] D. L. JAMES and D. K. PAI: *DyRT: dynamic response textures for real time deformation simulation with graphics hardware.* In *Proceedings of the 29th annual conference on Computer graphics and interactive techniques*, pages 582–585, 2002.

[20] M. G. CHOI and H. S. KO: *Modal warping: real-time simulation of large rotational deformation and manipulation.* IEEE Transactions on Visualization and Computer Graphics, 11:91–101, 2005.

[21] R. BRIDSON, S. MARINO, and R. FEDKIW: *Simulation of clothing with folds and wrinkles.* In *Proceedings of the 2003 ACM SIGGRAPH/Eurographics symposium on Computer animation*, pages 28–36, 2003.

[22] A. E. SIEGMAN: *Lasers.* University Science Books, 1st edition edition, 1986.

[23] M. A. GOLUB, A. M. PROKHOROV, I. N. SISAKYAN, and V. A. SOĬFER: *Synthesis of spatial filters for investigation of the transverse mode composition of coherent radiation.* Soviet Journal of Quantum Electronics, 12:1208–1209, 1982.

[24] M. A. GOLUB, L. SHIMSHI, N. DAVIDSON, and A. A. FRIESEM: *Mode-matched phase diffractive optical element for detecting laser modes with spiral phases.* Applied Optics, 46:7823–7828, 2007.

[25] T. KAISER, D. FLAMM, S. SCHRÖTER, and M. DUPARRÉ: *Complete modal decomposition foroptical fibers using CGH-basedcorrelation filters.* Optics Express, 17:9347–9356, 2009.

[26] O. A. SCHMIDT, C. SCHULZE, D. FLAMM, R. BRÜNING, T. KAISER, S. SCHRÖTER, and M. DUPARRÉ: *Real-time determination of laser beam quality by modal decomposition.* Optics Express, 19:6741–6748, 2011.

[27] D. FLAMM, C. SCHULZE, O. A. SCHMIDT, S. SCHRÖTER, and M. DUPARRÉ: *Mode analysis of LMA fibers using the correlation filter method.* Proceedings of SPIE, 8237:82370Z, 2012.

[28] O. SHAPIRA, A. F. ABOURADDY, J. D. JOANNOPOULOS, and Y. FINK: *Complete Modal Decomposition for Optical Waveguides.* Physical Review Letters, 94:143902, 2005.

[29] A. P. NAPARTOVICH and D. V. VYSOTSKY: *Theory of spatial mode competition in a fiber amplifier.* Physical Review A, 76:063801, 2007.

[30] H. YODA, P. POLYNKIN, and M. MANSURIPUR: *Beam quality factor of higher order modes in a step-index fiber.* Journal of Lightwave Technology, 24:1350–1355, 2006.

[31] H. M. LAMBERTON and V. G. ROPER: *Beam divergence of a highly multi-mode CO_2 laser.* Journal of Physics E: Scientific Instruments, 11:1102–1103, 1978.

[32] D. FLAMM, C. SCHULZE, R. BRÜNING, O. A. SCHMIDT, T. KAISER, S. SCHRÖTER, and M. DUPARRÉ: *Fast M^2 measurement for fiber beams based on modal analysis.* Applied Optics, 51:987–993, 2012.

[33] J. P. KOPLOW, D. A. V. KLINER, and L. GOLDBERG: *Single-mode operation of a coiled multimode fiber amplifier.* Optics Letters, 25:442–444, 2000.

[34] S. WIELANDY: *Implications of higher-order mode content in large mode area fibers with good beam quality.* Optics Express, 15:15402–15409, 2007.

[35] R. T. SCHERMER and J. H. COLE: *Improved Bend Loss Formula Verified for Optical Fiber by Simulation and Experiment.* IEEE Journal of Quantum Electronics, 43:899–909, 2007.

[36] R. Oron, Y. Danziger, N. Davidson, A. A. Friesem, and E. Hasman: *Laser mode discrimination with intra-cavity spiral phase elements.* Optics Communications, 169:115–121, 1999.

[37] R. Oron, Y. Danziger, N. Davidson, A. A. Friesem, and E. Hasman: *Discontinuous phase elements for transverse mode selection in laser resonators.* Applied Physics Letters, 74:1373–1375, 1999.

[38] C. Blanca and S. Hell: *Axial superresolution with ultrahigh aperture lenses.* Optics Express, 10:893–898, 2002.

[39] J. Kim, D. C. Kim, and S. H. Back: *Demonstration of high lateral resolution in laser confocal microscopy using annular and radially polarized light.* Microscopy Research and Technique, 72:441–446, 2009.

[40] I. Izeddin, M. El Beheiry, J. Andilla, D. Ciepielewski, X. Darzacq, and M. Dahan: *PSF shaping using adaptive optics for three-dimensional single-molecule super-resolution imaging and tracking.* Optics Express, 20:4957–4967, 2012.

[41] S. W. Hell and J. Wichmann: *Breaking the diffraction resolution limit by stimulated emission: stimulated-emission-depletion fluorescence microscopy.* Optics Letters, 19:780–782, 1994.

[42] S. W. Hell and M. Kroug: *Ground-state-depletion fluorscence microscopy: A concept for breaking the diffraction resolution limit.* Applied Physics B, 60:495–497, 1995.

[43] J. Keller, A. Schönle, and S. W. Hell: *Efficient fluorescence inhibition patterns for RESOLFT microscopy.* Optics Express, 15:3361–3371, 2007.

[44] M. G. L. Gustafsson: *Surpassing the lateral resolution limit by a factor of two using structured illumination microscopy.* Journal of Microscopy, 198:82–87, 2000.

[45] V. Studer, J. Bobin, M. Chahid, H. Moussavi, E. Candes, and M. Dahan: *Compressive Fluorescence Microscopy for Biological and Hyperspectral Imaging*, 2012.

[46] G. Ghielmetti and C. M. Aegerter: *Scattered light fluorescence microscopy in three dimensions.* Optics Express, 20:3744–3752, 2012.

[47] D. McGloin, G. C. Spalding, H. Melville, W. Sibbett, and K. Dholakia: *Three-dimensional arrays of optical bottle beams.* Optics Communications, 225:215–222, 2003.

[48] K. T. GAHAGAN and G. A. SWARTZLANDER: *Optical vortex trapping of particles.* Optics Letters, 21:827–829, 1996.

[49] D. P. RHODES, D. M. GHERARDI, J. LIVESEY, D. MCGLOIN, H. MELVILLE, T. FREEGARDE, and K. DHOLAKIA: *Atom guiding along high order Laguerre Gaussian light beams formed by spatial light modulation.* Journal of Modern Optics, 53:547–556, 2006.

[50] S. A. TATARKOVA, W. SIBBETT, and K. DHOLAKIA: *Brownian Particle in an Optical Potential of the Washboard Type.* Physical Review Letters, 91:038101, 2003.

[51] J. BAUMGARTL, M. MAZILU, and K. DHOLAKIA: *Optically mediated particle clearing using Airy wavepackets.* Nature Photonics, 2:675–678, 2008.

[52] M. M. BURNS, J. M. FOURNIER, and J. A. GOLOVCHENKO: *Optical binding.* Physical Review Letters, 63:1233–1236, 1989.

[53] V. GARCES-CHAVEZ, D. MCGLOIN, H. MELVILLE, W. SIBBETT, and K. DHOLAKIA: *Simultaneous micromanipulation in multiple planes using a self-reconstructing light beam.* Nature, 419:145–147, 2002.

[54] J. ARLT, V. GARCES-CHAVEZ, W. SIBBETT, and K. DHOLAKIA: *Optical micromanipulation using a Bessel light beam.* Optics Communications, 197:239–245, 2001.

[55] W. M. LEE and X. C. YUAN: *Observation of three-dimensional optical stacking of microparticles using a single Laguerre–Gaussian beam.* Applied Physics Letters, 83:5124–5126, 2003.

[56] E. R. DUFRESNE, G. C. SPALDING, M. T. DEARING, S. A. SHEETS, and D. G. GRIER: *Computer-generated holographic optical tweezer arrays.* Review of Scientific Instruments, 72:1810–1816, 2001.

[57] V. GARCÉS CHÁVEZ, K. DHOLAKIA, and G. C. SPALDING: *Extended-area optically induced organization of microparticles on a surface.* Applied Physics Letters, 86:031106, 2005.

[58] C. D. MELLOR and C. D. BAIN: *Array Formation in Evanescent Waves.* ChemPhysChem, 7:329–332, 2006.

[59] M. P. MACDONALD, G. C. SPALDING, and K. DHOLAKIA: *Microfluidic sorting in an optical lattice.* Nature, 426:421–424, 2003.

[60] T. ČIŽMÁR, M. ŠILER, M. ŠERÝ, P. ZEMÁNEK, V. G. CHÁVEZ, and K. DHOLAKIA: *Optical sorting and detection of submicrometer objects in a motional standing wave.* Physical Review B, 74:035105, 2006.

[61] L. Paterson, M. P. MacDonald, J. Arlt, W. Sibbett, P. E. Bryant, and K. Dholakia: *Controlled rotation of optically trapped microscopic particles.* Science, 292:912–914, 2001.

[62] H. He, M. E. J. Friese, N. R. Heckenberg, and H. Rubinsztein Dunlop: *Direct Observation of Transfer of Angular Momentum to Absorptive Particles from a Laser Beam with a Phase Singularity.* Physical Review Letters, 75:826–829, 1995.

[63] M. E. J. Friese, J. Enger, H. Rubinsztein Dunlop, and N. R. Heckenberg: *Optical angular-momentum transfer to trapped absorbing particles.* Physical Review A, 54:1593–1596, 1996.

[64] V. Garcés Chávez, D. McGloin, M. J. Padgett, W. Dultz, H. Schmitzer, and K. Dholakia: *Observation of the Transfer of the Local Angular Momentum Density of a Multiringed Light Beam to an Optically Trapped Particle.* Physical Review Letters, 91:093602, 2003.

[65] K. Ladavac and D. Grier: *Microoptomechanical pumps assembled and driven by holographic optical vortex arrays.* Optics Express, 12:1144–1149, 2004.

[66] M. Aeschlimann, M. Bauer, D. Bayer, T. Brixner, F. J. Garcia de Abajo, W. Pfeiffer, M. Rohmer, C. Spindler, and F. Steeb: *Adaptive subwavelength control of nano-optical fields.* Nature, 446:301–304, 2007.

[67] X. Li and M. I. Stockman: *Highly efficient spatiotemporal coherent control in nanoplasmonics on a nanometer-femtosecond scale by time reversal.* Physical Review B, 77:195109, 2008.

[68] G. Volpe, S. Cherukulappurath, R. Juanola Parramon, G. Molina-Terriza, and R. Quidant: *Controlling the Optical Near Field of Nanoantennas with Spatial Phase-Shaped Beams.* Nano Letters, 9:3608–3611, 2009.

[69] B. Gjonaj, J. Aulbach, P. M. Johnson, A. P. Mosk, L. Kuipers, and A. Lagendijk: *Active spatial control of plasmonic fields.* Nature Photonics, 5:360–363, 2011.

[70] R. Quidant, G. Badenes, S. Cheylan, R. Alcubilla, J. C. Weeber, and C. Girard: *Sub-wavelength patterning of the optical near-field.* Optics Express, 12:282–287, 2004.

[71] P. Mühlschlegel, H. J. Eisler, O. J. F. Martin, B. Hecht, and D. W. Pohl: *Resonant Optical Antennas.* Science, 308:1607–1609, 2005.

[72] R. QUIDANT, D. PETROV, and G. BADENES: *Radiation forces on a Rayleigh dielectric sphere in a patterned optical near field.* Optics Letters, 30:1009–1011, 2005.

[73] M. RIGHINI, A. S. ZELENINA, C. GIRARD, and R. QUIDANT: *Parallel and selective trapping in a patterned plasmonic landscape.* Nature Physics, 3:477–480, 2007.

[74] M. L. JUAN, M. RIGHINI, and R. QUIDANT: *Plasmon nano-optical tweezers.* Nature Photonics, 5:349–356, 2011.

[75] J. N. ANKER, W. P. HALL, O. LYANDRES, N. C. SHAH, J. ZHAO, and R. P. VAN DUYNE: *Biosensing with plasmonic nanosensors.* Nature Materials, 7:442–453, 2008.

[76] Sheng WANG, Sadao OTA, Bin GUO, Jongeun RYU, Christopher RHODES, Yi XIONG, Sheraz KALIM, Li ZENG, Yong CHEN, Michael A. TEITELL, and Xiang ZHANG: *Subcellular Resolution Mapping of Endogenous Cytokine Secretion by Nano-Plasmonic-Resonator Sensor Array.* Nano Letters, 11:3431–3434, 2011.

[77] A. AHMED and R. GORDON: *Single Molecule Directivity Enhanced Raman Scattering using Nanoantennas.* Nano Letters, 12:2625–2630, 2012.

[78] J. S. DONNER, G. BAFFOU, D. MCCLOSKEY, and R. QUIDANT: *Plasmon-Assisted Optofluidics.* ACS Nano, 5:5457–5462, 2011.

[79] B. J. ROXWORTHY and K. C. TOUSSAINT: *Plasmonic nanotweezers: strong influence of adhesion layer and nanostructure orientation on trapping performance.* Optics Express, 20:9591–9603, 2012.

[80] P. A. M. DIRAC: *The Principles of Quantum Mechanics.* Oxford University Press, 4th edition, 1982.

[81] Eugene HECHT: *Optics.* Addison Wesley, 2001.

[82] A. EINSTEIN: *Über einen die Erzeugung und Verwandlung des Lichtes betreffenden heuristischen Gesichtspunkt.* Annalen der Physik, 322:132–148, 1905.

[83] J. J. STAMNES: *Waves in Focal Regions.* Taylor & Francis, 1st edition, 1986.

[84] Max BORN and Emil WOLF: *Principles of Optics.* Cambridge University Press, 1999.

[85] R. W. DITCHBURN: *Light.* Dover Publications, 2011.

[86] J. W. GOODMAN: *Introduction To Fourier Optics*. McGraw-Hill, 2nd edition, 1996.

[87] E. WOLF: *Electromagnetic Diffraction in Optical Systems. I. An Integral Representation of the Image Field*. Royal Society of London Proceedings Series A, 253:349–357, 1959.

[88] Marcel LEUTENEGGER, Ramachandra RAO, Rainer A. LEITGEB, and Theo LASSER: *Fast focus field calculations*. Opt. Express, 14:11277–11291, 2006.

[89] Stefan W. HELL: *Far-Field Optical Nanoscopy*. Science, 316:1153–1158, 2007.

[90] Eric BETZIG, George H. PATTERSON, Rachid SOUGRAT, O. Wolf LINDWASSER, Scott OLENYCH, Juan S. BONIFACINO, Michael W. DAVIDSON, Jennifer LIPPINCOTT-SCHWARTZ, and Harald F. HESS: *Imaging Intracellular Fluorescent Proteins at Nanometer Resolution*. Science, 313:1642–1645, 2006.

[91] George H. PATTERSON: *Fluorescence microscopy below the diffraction limit*. Semin. Cell Dev. Biol., 20:886–893, 2009.

[92] A. M. van OIJEN, J. KÖHLER, J. SCHMIDT, M. MÜLLER, and G. J. BRAKENHOFF: *Far-field fluorescence microscopy beyond the diffraction limit*. J. Opt. Soc. Am. A, 16:909–915, 1999.

[93] C. J. R. SHEPPARD and D. M. SHOTTON: *Confocal Laser Scanning Microscopy*. BIOS Scientific Publishers, 1997.

[94] Timothy R. CORLE and Gordon S. KINO: *Confocal Scanning Optical Microscopy and Related Imaging Systems*. Academic Press, 1996.

[95] G. TORALDO DI FRANCIA: *Resolving Power and Information*. Journal of the Optical Society of America, 45:497–499, 1955.

[96] D. GABOR: *IV Light and Information*, pages 109–153. Elsevier, 1961.

[97] G. TORALDO DI FRANCIA: *Degrees of Freedom of an Image*. Journal of the Optical Society of America, 59:799–803, 1969.

[98] D. A. B. MILLER: *Communicating with Waves Between Volumes: Evaluating Orthogonal Spatial Channels and Limits on Coupling Strengths*. Applied Optics, 39:1681–1699, 2000.

[99] D. A. B. MILLER: *Spatial channels for communicating with waves between volumes*. Optics Letters, 23:1645–1647, 1998.

[100] R. Piestun and D. A. Miller: *Electromagnetic degrees of freedom of an optical system.* Journal of the Optical Society of America A, 17:892–902, 2000.

[101] M. Mazilu, J. Baumgartl, S. Kosmeier, and K. Dholakia: *Optical Eigenmodes; exploiting the quadratic nature of the energy flux and of scattering interactions.* Opt. Express, 19:933–945, 2011.

[102] D. Slepian and H. O. Pollak: *Prolate spheroidal wave functions, Fourier analysis, and uncertainty—I.* Bell Syst. Tech. J., 40:43–64, 1961.

[103] G. Walter and T. Soleski: *A new friendly method of computing prolate spheroidal wave functions and wavelets.* Applied and Computational Harmonic Analysis, 19:432–443, 2005.

[104] K. Fukunaga: *Introduction to Statistical Pattern Recognition.* Academic Press, 2nd edition, 1990.

[105] M. Ploschner, M. Mazilu, T. Čižmár, and K. Dholakia: *Numerical investigation of passive optical sorting of plasmon nanoparticles.* Optics Express, 19:13922–13933, 2011.

[106] Eric Betzig and Jay K. Trautman: *Near-Field Optics: Microscopy, Spectroscopy, and Surface Modification Beyond the Diffraction Limit.* Science, 257:189–195, 1992.

[107] Zengbo Wang, Wei Guo, Lin Li, Boris Luk'yanchuk, Ashfaq Khan, Zhu Liu, Zaichun Chen, and Minghui Hong: *Optical virtual imaging at 50 nm lateral resolution with a white-light nanoscope.* Nat. Commun., 2:218, 2011.

[108] M. J. Rust, M. Bates, and X. Zhuang: *Sub-diffraction-limit imaging by stochastic optical reconstruction microscopy (STORM).* Nature Methods, 3:793–796, 2006.

[109] J. B. Pendry: *Negative Refraction Makes a Perfect Lens.* Phys. Rev. Lett., 85:3966–3969, 2000.

[110] Nicholas Fang, Hyesog Lee, Cheng Sun, and Xiang Zhang: *Subdiffraction-Limited Optical Imaging with a Silver Superlens.* Science, 308:534–537, 2005.

[111] Xiang Zhang and Zhaowei Liu: *Superlenses to overcome the diffraction limit.* Nat. Mater., 7:435–441, 2008.

[112] R. K. Luneburg: *Mathematical theory of optics.* Brown University Press, 1st edition, 1944.

[113] Harold OSTERBERG and Jr WILKINS: *The Resolving Power of a Coated Objective.* J. Opt. Soc. Am., 39:553–557, 1949.

[114] Harold OSTERBERG and Franklyn C. WISSLER: *The Resolution of Two Particles in a Bright Field by Coated Microscope Objectives.* J. Opt. Soc. Am., 39:558–563, 1949.

[115] Jr WILKINS: *The Resolving Power of a Coated Objective II.* J. Opt. Soc. Am., 40:222–224, 1950.

[116] G. Toraldo di FRANCIA: *Super-gain antennas and optical resolving power.* Il Nuovo Cimento, 9:426–438, 1952.

[117] B. R. FRIEDEN: *On Arbitrarily Perfect Imagery with a Finite Aperture.* J. Mod. Opt., 16:795–807, 1969.

[118] G. R. BOYER: *Pupil filters for moderate superresolution.* Appl. Opt., 15:3089–3093, 1976.

[119] Richard BOIVIN and Albéric BOIVIN: *Optimized Amplitude Filtering for Superresolution Over a Restricted Field.* J. Mod. Opt., 27:587–610, 1980.

[120] Matt S. CALDER and Achim KEMPF: *Analysis of superoscillatory wave functions.* J. Math. Phys., 46:012101, 2005.

[121] P. J. S. G. FERREIRA and A. KEMPF: *Superoscillations: Faster Than the Nyquist Rate.* IEEE Trans. Signal Process., 54:3732–3740, 2006.

[122] Fu M. HUANG, Nikolay I. ZHELUDEV, Yifang CHEN, and F. Javier Garcia de ABAJO: *Focusing of light by a nanohole array.* Appl. Phys. Lett., 90:091119, 2007.

[123] Fu M. HUANG, Yifang CHEN, F. Javier Garcia de ABAJO, and Nikolay I. ZHELUDEV: *Optical super-resolution through super-oscillations.* J. Opt. A: Pure Appl. Opt., 9:S285–S288, 2007.

[124] Nikolay I. ZHELUDEV: *What diffraction limit?* Nat. Mater., 7:420–422, 2008.

[125] Fu M. HUANG and Nikolay I. ZHELUDEV: *Super-Resolution without Evanescent Waves.* Nano Lett., 9:1249–1254, 2009.

[126] Tasso R. M. SALES: *Smallest Focal Spot.* Phys. Rev. Let., 81:3844–3847, 1998.

[127] C. J. R. SHEPPARD and Z. S. HEGEDUS: *Axial behavior of pupil-plane filters.* J. Opt. Soc. Am. A, 5:643–647, 1988.

[128] Ingemar J. COX: *Increasing the bit packing densities of optical disk systems.* Appl. Opt., 23:3260–3261, 1984.

[129] Y. YAMANAKA, Y. HIROSE, H. FUJII, and K. KUBOTA: *High density recording by superresolution in an optical disk memory system.* Applied Optics, 29:3046–3051, 1990.

[130] Z. S. HEGEDUS: *Annular Pupil Arrays: Application to Confocal Scanning.* Optica Acta, 32:815–826, 1985.

[131] Z. S. HEGEDUS and V. SARAFIS: *Superresolving filters in confocally scanned imaging systems.* J. Opt. Soc. Am. A, 3:1892–1896, 1986.

[132] X. S. GAN and C. J. R. SHEPPARD: *Imaging in a confocal microscope with one circular and one annular lens.* Optics Communications, 103:254–264, 1993.

[133] M. MARTÍNEZ-CORRAL: *Tunable axial superresolution by annular binary filters. Application to confocal microscopy.* Opt. Commun., 119:491–498, 1995.

[134] Zhihua DING, Guiying WANG, Min GU, Zhijiang WANG, and Zhifeng FAN: *Superresolution with an apodization film in a confocal setup.* Appl. Opt., 36:360–363, 1997.

[135] M. MARTÍNEZ-CORRAL: *Three-dimensional superresolution by annular binary filters.* Opt. Commun., 165:267–278, 1999.

[136] M. A. A. NEIL, R. JUŠKAITIS, T. WILSON, Z. J. LACZIK, and V. SARAFIS: *Optimized pupil-plane filters for confocal microscope point-spread function engineering.* Opt. Lett., 25:245–247, 2000.

[137] Manuel MARTINEZ-CORRAL, M. CABALLERO, Ernst H. K. STELZER, and Jim SWOGER: *Tailoring the axial shape of the point spread function using the Toraldo concept.* Opt. Express, 10:98–103, 2002.

[138] M. MARTINEZ-CORRAL, C. Ibáñez LÓPEZ, G. SAAVEDRA, and M. CABALLERO: *Axial gain resolution in optical sectioning fluorescence microscopy by shaded-ring filters.* Opt. Express, 11:1740–1745, 2003.

[139] Haitao LIU, Yingbai YAN, Deer YI, and Guofan JIN: *Design of Three-Dimensional Superresolution Filters and Limits of Axial Optical Superresolution.* Appl. Opt., 42:1463–1476, 2003.

[140] G. BOYER: *3D Behaviour of Frieden filters in confocal imaging.* Micron, 34:275–282, 2003.

[141] Phanindra GUNDU, Erwin HACK, and Pramod RASTOGI: *High efficient superresolution combination filter with twin LCD spatial light modulators.* Opt. Express, 13:2835–2842, 2005.

[142] Maojin YUN, Liren LIU, Jianfeng SUN, and De'an LIU: *Three-dimensional superresolution by three-zone complex pupil filters.* J. Opt. Soc. Am. A, 22:272–277, 2005.

[143] Haitao LIU, Yingbai YAN, and Guofan JIN: *Design theories and performance limits of diffractive superresolution elements with the highest sidelobe suppressed.* J. Opt. Soc. Am. A, 22:828–838, 2005.

[144] Rüdiger PASCHOTTA: *Encyclopedia of Laser Physics and Technology.* Wiley-VCH, 2008.

[145] J. LIANG, S. Y. WU, F. K. FATEMI, and M. F. BECKER: *Suppression of the zero-order diffracted beam from a pixelated spatial light modulator by phase compression.* Applied Optics, 51:3294–3304, 2012.

[146] Y. IGASAKI, F. LI, N. YOSHIDA, H. TOYODA, T. INOUE, N. MUKOHZAKA, Y. KOBAYASHI, and T. HARA: *High Efficiency Electrically-Addressable Phase-Only Spatial Light Modulator.* Optical Review, 6:339–344, 1999.

[147] Tomas CIZMAR, Michael MAZILU, and Kishan DHOLAKIA: *In situ wavefront correction and its application to micromanipulation.* Nat. Photonics, 4:388–394, 2010.

[148] Roberto DI LEONARDO, Francesca IANNI, and Giancarlo RUOCCO: *Computer generation of optimal holograms for optical trap arrays.* Opt. Express, 15:1913–1922, 2007.

[149] I. J. COX, C. J. R. SHEPPARD, and T. WILSON: *Reappraisal of arrays of concentric annuli as superresolving filters.* J. Opt. Soc. Am., 72:1287–1291, 1982.

[150] Virendra N. MAHAJAN: *Strehl ratio for primary aberrations: some analytical results for circular and annular pupils.* J. Opt. Soc. Am., 72:1258–1266, 1982.

[151] Stefan W. HELL: *Toward fluorescence nanoscopy.* Nat. Biotechnol., 21:1347–1355, 2003.

[152] B. LITTLETON, K. LAI, D. LONGSTAFF, V. SARAFIS, P. MUNROE, N. HECKENBERG, and H. RUBINSZTEIN-DUNLOP: *Coherent super-resolution microscopy via laterally structured illumination.* Micron, 38:150–157, 2007.

[153] E. T. F. ROGERS, J. LINDBERG, T. ROY, S. SAVO, J. E. CHAD, M. R. DENNIS, and N. I. ZHELUDEV: *A super-oscillatory lens optical microscope for subwavelength imaging.* Nature Materials, 11:432–435, 2012.

[154] H. J. HYVÄRINEN, S. REHMAN, J. TERVO, J. TURUNEN, and C. J. R. SHEPPARD: *Limitations of superoscillation filters in microscopy applications.* Optics Letters, 37:903–905, 2012.

[155] M. POSPIECH, M. EMONS, K. KUETEMEYER, A. HEISTERKAMP, and U. MORGNER: *Superresolved femtosecond laser nanosurgery of cells.* Biomedical Optics Express, 2:264–271, 2011.

[156] S. KOLJENOVIĆ, T. C. BAKKER SCHUT, J. P. van MEERBEECK, A. P. MAAT, S. A. BURGERS, P. E. ZONDERVAN, J. M. KROS, and G. J. PUPPELS: *Raman microspectroscopic mapping studies of human bronchial tissue.* Journal of Biomedical Optics, 9:1187–1197, 2004.

[157] K. M. TAN, C. S. HERRINGTON, and C. T. A. BROWN: *Discrimination of normal from pre-malignant cervical tissue by Raman mapping of deparaffinized histological tissue sections.* Journal of Biophotonics, 4:40–48, 2011.

[158] G. SCARCELLI and S. H. YUN: *Entangled-photon coincidence fluorescence imaging.* Optics Express, 16:16189–16194, 2008.

[159] G. A. WAGNIERES, W. M. STAR, and B. C. WILSON: *In Vivo Fluorescence Spectroscopy and Imaging for Oncological Applications.* Photochemistry and Photobiology, 68:603–632, 1998.

[160] E. B. HANLON, R. MANOHARAN, T. W. KOO, K. E. SHAFER, J. T. MOTZ, M. FITZMAURICE, J. R. KRAMER, I. ITZKAN, R. R. DASARI, and M. S. FELD: *Prospects for in vivo Raman spectroscopy.* Physics in Medicine and Biology, 45:R1, 2000.

[161] H. H. MANTSCH, L. P. CHOO-SMITH, and R. A. SHAW: *Vibrational spectroscopy and medicine: an alliance in the making.* Vibrational Spectroscopy, 30:31–41, 2002.

[162] Y. K. MIN, T. YAMAMOTO, E. KOHDA, T. ITO, and H. O. HAMAGUCHI: *1064 nm near-infrared multichannel Raman spectroscopy of fresh human lung tissues.* Journal of Raman Spectroscopy, 36:73–76, 2005.

[163] D. V. STREKALOV, A. V. SERGIENKO, D. N. KLYSHKO, and Y. H. SHIH: *Observation of Two-Photon "Ghost" Interference and Diffraction.* Physical Review Letters, 74:3600–3603, 1995.

[164] A. G. WHITE, J. R. MITCHELL, O. NAIRZ, and P. G. KWIAT: *"Interaction-free" imaging.* Physical Review A, 58:605–613, 1998.

[165] R. S. BENNINK, S. J. BENTLEY, and R. W. BOYD: *"Two-Photon" coincidence imaging with a classical source.* Physical Review Letters, 89, 2002.

[166] T. B. PITTMAN, Y. H. SHIH, D. V. STREKALOV, and A. V. SERGIENKO: *Optical imaging by means of two-photon quantum entanglement.* Physical Review A, 52:R3429–R3432, 1995.

[167] M. ZUKOWSKI, A. ZEILINGER, M. A. HORNE, and H. WEINFURTER: *Independent Photons and Entanglement. A Short Overview.* International Journal of Theoretical Physics, pages 501–517, 1999.

[168] G. SCARCELLI, V. BERARDI, and Y. SHIH: *Can Two-Photon Correlation of Chaotic Light Be Considered as Correlation of Intensity Fluctuations?* Physical Review Letters, 96:063602, 2006.

[169] A. GATTI, M. BONDANI, L. A. LUGIATO, M. G. A. PARIS, and C. FABRE: *Comment on "Can Two-Photon Correlation of Chaotic Light Be Considered as Correlation of Intensity Fluctuations?".* Physical Review Letters, 98:039301, 2007.

[170] G. SCARCELLI, V. BERARDI, and Y. H. SHIH: *Scarcelli, Berardi, and Shih Reply:.* Physical Review Letters, 98:039302, 2007.

[171] R. S. BENNINK, S. J. BENTLEY, R. W. BOYD, and J. C. HOWELL: *Quantum and classical coincidence imaging.* Physical Review Letters, 92, 2004.

[172] A. GATTI, E. BRAMBILLA, M. BACHE, and L. A. LUGIATO: *Ghost Imaging with Thermal Light: Comparing Entanglement and ClassicalCorrelation.* Physical Review Letters, 93:093602, 2004.

[173] F. FERRI, D. MAGATTI, A. GATTI, M. BACHE, E. BRAMBILLA, and L. A. LUGIATO: *High-Resolution Ghost Image and Ghost Diffraction Experiments with Thermal Light.* Physical Review Letters, 94:183602, 2005.

[174] A. VALENCIA, G. SCARCELLI, M. D'ANGELO, and Y. SHIH: *Two-Photon Imaging with Thermal Light.* Physical Review Letters, 94:063601, 2005.

[175] B. I. ERKMEN and J. H. SHAPIRO: *Unified theory of ghost imaging with Gaussian-state light.* Physical Review A, 77:043809, 2008.

[176] B. I. ERKMEN and J. H. SHAPIRO: *Signal-to-noise ratio of Gaussian-state ghost imaging.* Physical Review A, 79:023833, 2009.

[177] R. MEYERS, K. S. DEACON, and Y. SHIH: *Ghost-imaging experiment by measuring reflected photons.* Physical Review A, 77:041801, 2008.

[178] J. H. SHAPIRO: *Computational ghost imaging.* Physical Review A, 78:061802, 2008.

[179] Y. BROMBERG, O. KATZ, and Y. SILBERBERG: *Ghost imaging with a single detector.* Physical Review A, 79:053840, 2009.

[180] J. DU, W. GONG, and S. HAN: *The influence of sparsity property of images on ghost imaging with thermal light.* Optics Letters, 37:1067–1069, 2012.

[181] O. KATZ, Y. BROMBERG, and Y. SILBERBERG: *Compressive ghost imaging.* Applied Physics Letters, 95:131110, 2009.

[182] F. FERRI, D. MAGATTI, L. A. LUGIATO, and A. GATTI: *Differential Ghost Imaging.* Physical Review Letters, 104:253603, 2010.

[183] J. ROMBERG: *Imaging via Compressive Sampling.* IEEE Signal Processing Magazine, 25:14–20, 2008.

[184] J. CHENG and S. HAN: *Classical correlated imaging from the perspective of coherent-mode representation.* Physical Review A, 76:023824, 2007.

[185] Anna C. DE LUCA, Sebastian KOSMEIER, Kishan DHOLAKIA, and Michael MAZILU: *Optical eigenmode imaging.* Physical Review A, 84:021803, 2011.

[186] N. TIAN, Q. GUO, A. WANG, D. XU, and L. FU: *Fluorescence ghost imaging with pseudothermal light.* Optics Letters, 36:3302–3304, 2011.

[187] D. MALACARA: *Optical Shop Testing.* Wiley-Interscience, 2nd edition, 1992.

[188] J. R. LAKOWICZ: *Principles of Fluorescence Spectroscopy.* Springer, 3rd edition, 2006.

[189] G. G. STOKES: *On the Change of Refrangibility of Light.* Philosophical Transactions of the Royal Society of London, 142:463–562, 1852.

[190] B. N. G. GIEPMANS, S. R. ADAMS, M. H. ELLISMAN, and R. Y. TSIEN: *The Fluorescent Toolbox for Assessing Protein Location and Function.* Science, 312:217–224, 2006.

[191] M. KERKER: *The scattering of light and other electromagnetic radiation.* Academic Press, 1969.

[192] C. V. RAMAN and K. S. KRISHNAN: *A New Type of Secondary Radiation.* Nature, 121:501–502, 1928.

[193] E. LE RU and P. ETCHEGOIN: *Principles of Surface-Enhanced Raman Spectroscopy.* Elsevier Science, 1st edition, 2008.

[194] J. KNEIPP, H. KNEIPP, and K. KNEIPP: *SERS–a single-molecule and nanoscale tool for bioanalytics.* Chemical Society reviews, 37:1052–1060, 2008.

[195] A. M. KERN and O. J. F. MARTIN: *Excitation and Reemission of Molecules near Realistic Plasmonic Nanostructures.* Nano Letters, 11:482–487, 2011.

[196] J. ANDO, K. FUJITA, N. I. SMITH, and S. KAWATA: *Dynamic SERS imaging of cellular transport pathways with endocytosed gold nanoparticles.* Nano Letters, 11:5344–5348, 2011.

[197] A. CAMPION and P. KAMBHAMPATI: *Surface-enhanced Raman scattering.* Chemical Society Reviews, 27:241–250, 1998.

[198] E. C. LE RU, J. GRAND, I. SOW, W. R. C. SOMERVILLE, P. G. ETCHEGOIN, M. TREGUER-DELAPIERRE, G. CHARRON, N. FÉLIDJ, G. LÉVI, and J. AUBARD: *A Scheme for Detecting Every Single Target Molecule with Surface-Enhanced Raman Spectroscopy.* Nano Letters, 11:5013–5019, 2011.

[199] W. D. MONTGOMERY: *Phase retrieval and the polarization identity.* Optics Letters, 2:120–121, 1978.

[200] M. MAZILU, A. C. DE LUCA, A. RICHES, C. S. HERRINGTON, and K. DHOLAKIA: *Optimal algorithm for fluorescence suppression of modulated Raman spectroscopy.* Optics Express, 18:11382–11395, 2010.

[201] L. LI, T. HUTTER, A. S. FINNEMORE, F. M. HUANG, J. J. BAUMBERG, S. R. ELLIOTT, U. STEINER, and S. MAHAJAN: *Metal Oxide Nanoparticle Mediated Enhanced Raman Scattering and Its Use in Direct Monitoring of Interfacial Chemical Reactions.* Nano Letters, 2012.

[202] N. GUARROTXENA, Y. REN, and A. MIKHAILOVSKY: *Raman Response of Dithiolated Nanoparticle Linkers.* Langmuir, 27:347–351, 2010.

[203] M. MAZILU and K. DHOLAKIA: *Selective and optimal illumination of nanophotonic structures using optical eigenmodes.* arXiv:1111.7111v1, 2011.

[204] J. ROSEN, L. SHIV, J. STEIN, and J. SHAMIR: *Electro-optic hologram generation on spatial light modulators.* Journal of the Optical Society of America A, 9:1159–1166, 1992.

[205] N. YOSHIKAWA, M. ITOH, and T. YATAGAI: *Adaptive computer-generated hologram using interpolation method.* Optical Review, 4:A161–A163, 1997.

[206] O. Ripoll, V. Kettunen, and H. P. Herzig: *Review of iterative Fourier-transform algorithms for beam shaping applications.* Optical Engineering, 43:2549–2556, 2004.

[207] Y. Hayasaki, T. Sugimoto, A. Takita, and N. Nishida: *Variable holographic femtosecond laser processing by use of a spatial light modulator.* Applied Physics Letters, 87:031101, 2005.

[208] S. Hasegawa and Y. Hayasaki: *Second-harmonic optimization of computer-generated hologram.* Optics Letters, 36:2943–2945, 2011.

[209] N. Matsumoto, T. Inoue, T. Ando, Y. Takiguchi, Y. Ohtake, and H. Toyoda: *High-quality generation of a multispot pattern using a spatial light modulator with adaptive feedback.* Optics Letters, 37:3135–3137, 2012.

[210] I. M. Vellekoop and A. P. Mosk: *Universal Optimal Transmission of Light Through Disordered Materials.* Physical Review Letters, 101:120601, 2008.

[211] M. Kim, Y. Choi, C. Yoon, W. Choi, J. Kim, Q. H. Park, and W. Choi: *Maximal energy transport through disordered media with the implementation of transmission eigenchannels.* Nature Photonics, advance online publication, 2012.

[212] I. M. Vellekoop, A. Lagendijk, and A. P. Mosk: *Exploiting disorder for perfect focusing.* Nature Photonics, 4:320–322, 2010.

[213] E. G. van Putten, D. Akbulut, J. Bertolotti, W. L. Vos, A. Lagendijk, and A. P. Mosk: *Scattering Lens Resolves Sub-100˜nm Structures with Visible Light.* Physical Review Letters, 106:193905, 2011.

[214] I. M. Vellekoop and A. P. Mosk: *Focusing coherent light through opaque strongly scattering media.* Optics Letters, 32:2309–2311, 2007.

[215] I. M. Vellekoop and A. P. Mosk: *Phase control algorithms for focusing light through turbid media.* Optics Communications, 281:3071–3080, 2008.

[216] S. J. Elliott and P. A. Nelson: *Active noise control.* Signal Processing Magazine, IEEE, 10:12–35, 1993.

[217] C. R. Fuller and A. H. von Flotow: *Active control of sound and vibration.* Control Systems, IEEE, 15:9–19, 1995.

[218] J. P. Taché: *Derivation of ABCD law for Laguerre-Gaussian beams.* Applied Optics, 26:2698–2700, 1987.